Ultrafast optical studies of pressure-tuned spin-orbit materials

Thesis by
Chen Li

In Partial Fulfillment of the Requirements for the
Degree of
Doctor of Philosophy in Physics

CALIFORNIA INSTITUTE OF TECHNOLOGY
Pasadena, California

2024
Defended June 19, 2023

Chen Li
ORCID: 0000-0001-6750-5925

ACKNOWLEDGEMENTS

I am deeply grateful and want to express my heartfelt appreciation to my esteemed Ph.D. advisor, David Hsieh. He embodies the essence of an extraordinary scientist whose profound insights and refined sensibilities have profoundly shaped my academic journey. Beyond his scientific acumen, he possesses a contemplative nature that extends to encompass societal and educational considerations. His contemplative musings have ignited within me a renewed perspective on the broader world. The guidance he has provided not only sharpened my scientific skills but also expanded my intellectual horizons.

I'd also like to extend my profound appreciation to the other members of my thesis committee, including Thomas F. Rosenbaum, Jason Alicea, Joseph Falson, and Jennifer Jackson. Their probing questions during my candidacy exam and thesis defense have been instrumental in refining my scientific focus and charting the course for my subsequent endeavors.

My sincerest gratitude extends to my collaborator and genuine friend, Xiang Li. Together, we faced the challenges inherent in the intricate task of developing the high-pressure ultrafast laser technique. Xiang's expertise in high-pressure techniques proved invaluable, as she graciously shared her insights and adeptly navigated me through the complexities of this endeavor. Moreover, her unwavering support fortified me with the resilience needed to overcome the hurdles we encountered. Our joint journey has not only enriched my scientific understanding but also forged an enduring partnership that I hold in the highest regard. Xiang is more than a colleague; she is a true confidante and genuine friend. I fondly recall the countless days and nights during which we labored side by side, engaging in debates about physics, dissecting review comments, and even delving into conversations beyond science.

Furthermore, my deep appreciation extends to Stephen Armstrong, an esteemed co-member of the late-night high-pressure club. Alongside him, I would be remiss not to acknowledge Daniel M. Silevitch, whose consistent presence and unfailing willingness to lend assistance have offered me a continuous source of reassurance throughout my doctoral journey. Additionally, I extend my sincere gratitude to Analytis and Cao groups for their invaluable collaboration in providing samples. Their combined wealth of technical expertise and unwavering support have served

as steadfast pillars upon which I leaned, providing me with the confidence needed to overcome challenges and navigate the intricacies of my research journey. Their presence has undoubtedly left an indelible mark on my academic odyssey, for which I am profoundly grateful.

A special tribute is also reserved for Kyle Seyler, a true exemplar within the realm of experimental science. Kyle's meticulous approach and unwavering dedication to precision have continually reminded me to approach my work with earnestness and methodological rigor. His unwavering commitment to his craft has made an indelible impression, encouraging me to mirror his conscientious approach in my own endeavors. I am immensely grateful for the invaluable insights he has imparted, enriching not only my scientific comprehension but also deepening my appreciation for the art of experimentation.

My time within the Hsieh lab has been immensely rewarding due to the presence of my exceptional colleagues. My gratitude extends to Hao Chu and Alberto de la Torre, who imparted to me foundational optical skills through their guidance in "Optics Lab 101." Additionally, I am deeply indebted to Dan van Beveren for his partnership in the optoelectronic project. Dan's insightful perspectives have played an integral role in shaping our collective understanding and approach. A special acknowledgment is due to Aditi Venkatesh, who provided me with the opportunity to experience the role of a mentor, from which I gained profound insights.

I extend my heartfelt gratitude to my esteemed labmates, Junyi Shan, Honglie Ning, and Omar Mehio, whose paths intertwined with mine when I first joined the lab. The memories we forged, gathered around the dinner table day after day, remain etched in my heart, even though they came at the cost of my wallet. I shall forever cherish the encouragement Omar bestowed upon me, his words echoing in my mind, affirming my abilities as a capable and astute researcher, urging me to embrace self-assurance. Junyi's unwavering companionship during my moments of despondency stands as a testament to our unbreakable bond. The warmth emanating from Honglie, coupled with his unrelenting dedication to research, never ceases to leave an indelible impression. The latter part of my Ph.D. journey introduced me to Yuchen Han and Ryo Noguchi, whose camaraderie lent a joyous hue to my days in the lab. Our shared experiences, be it relishing hotpot, savoring Korean delicacies, or indulging in Japanese cuisine at Ryo and Jiyeon's abode, will forever evoke smiles. I am indebted to all the group members, including Xinwei Li, Alon Ron, Nicholas Laurita, Tejas Deshpande, Youngjoon Han, Carina Belvin, Hoon Kim, and Mingyao

Guo. The cherished moments, the conversations that traversed the realms of science and life, have enriched me beyond measure. Their unwavering support, both in the realm of knowledge and spirit, constitutes an indispensable cornerstone of my doctoral odyssey. I am profoundly thankful for the irreplaceable role each individual has played, collectively shaping the tapestry of my PhD experience. During my PhD journey, I was fortunate to form numerous lifelong friendships. I am particularly grateful to Sijia Dong, Chang Liu, Shumao Zhang, Xirui Wang, Shibo Shu, Yalu Chen, Hao Zhou, Xichen Shi, Kun Miao, Menghan Liu, Xin Su, Botao Hu, Yukai Liu, Ge Chen, Yujia Huang, Jiajing Mao, Jim Zhang, and Yifan Su. The shared moments we experienced hold a special place in my heart.

I also want to express my heartfelt appreciation to my boyfriend, Sen Wang, for his exceptional culinary skills and impeccable taste in choosing wonderful restaurants. His ability to create delicious meals and guide us to amazing dining experiences has truly enriched my life. Moreover, I am thankful for his unwavering encouragement to pursue a healthier lifestyle. His persistent motivation to hit the gym has not only made me physically stronger but has also contributed to my overall well-being. His support has been instrumental in shaping me into a healthier and stronger individual.

Lastly, my heartfelt gratitude extends to my parents, Zhiqing Zhang and Yilong Li, and my grandparents Jiaying Yang, Changgeng Li, Yufang Lu, and Hua Zhang. Despite the considerable geographical distance between us, their enduring patience, love, support, and wisdom have been a constant in my life. Throughout these six years, they have stood as unwavering witnesses to every hurdle and accomplishment in my research journey. Their unwavering solidarity has been a source of strength during joy and hardship. I know I owe much of who I am to their presence in my life. I can confidently say that this Ph.D. is as much theirs as it is mine.

ABSTRACT

The advent of quantum materials has provided researchers with a remarkable opportunity to delve into the intricate interplay among various degrees of freedom, encompassing charge, orbital, spin, and lattice dynamics. Transition metal compounds, possessing distinct characteristics, exemplify the captivating competition between interactions arising from different degrees of freedom, each with comparable strength. These interactions encompass the on-site Coulomb interaction, kinetic hopping, spin-orbit coupling (SOC), crystal electric field splitting, and Hund's exchange coupling. In correlated electron systems of this nature, the intricate interplay of these complex interactions gives rise to a plethora of exotic phenomena, rendering the understanding of each variable a daunting task. Hence, it becomes imperative to explore their responses to external stimuli, and in this regard, hydrostatic pressure emerges as a versatile tool capable of tuning the strength of competing interactions and shifting the delicate balance between coexisting and competing ground states. This engenders a rich diversity of quantum phases and holds the potential to decouple these intertwined variables in phase transitions, thus unveiling the distinctive roles played by each constituent.

In Chapter I, a comprehensive discussion on pressure-induced phase transitions will ensue, encompassing phenomena such as insulator-metal transitions, spin-crossover transitions, structural transformations, and the fervent search for elusive quantum spin liquid and topological superconductive states. Chapter II shall delve into the experimental techniques that have been extensively employed throughout my research endeavors. This will encompass a synergistic combination of a high-pressure environment and cutting-edge ultrafast optical probing techniques, including optical second harmonic generation (SHG), harnessed by the high peak power of femtosecond lasers, as well as time-resolved reflectivity, capitalizing on the exceedingly short time duration of laser pulses. Moreover, a wide-field microscopy approach based on the magneto-optical Kerr effect shall be expounded upon, enabling direct observations of intricate domain structures. In subsequent chapters, three projects shall be elucidated, encompassing Weyl semimetals, with a specific focus on TaAs in Chapter III, $Co_3Sn_2S_2$ in Chapter V, and an investigation into the spin-orbit-coupled Mott insulator Sr_2IrO_4 in Chapter IV.

The transition metal monopnictide family of Weyl semimetals recently has been shown to exhibit anomalously strong second-order optical nonlinearity, which is

theoretically attributed to a highly asymmetric polarization distribution induced by their polar structure. We experimentally test this hypothesis by measuring optical SHG from TaAs across a pressure-tuned polar to non-polar structural phase transition. Despite the high-pressure structure remaining non-centrosymmetric, the SHG yield is reduced by more than 60% by 20 GPa as compared to the ambient pressure value. By examining the pressure dependence of distinct groups of SHG susceptibility tensor elements, we find that the yield is primarily controlled by a single element that governs the response along the polar axis. Our results confirm a connection between the polar axis and the giant optical nonlinearity of Weyl semimetals and demonstrate pressure as a means to tune this effect *in situ*.

Sr_2IrO_4 stands as an archetypal SOC-mediated Mott insulator, where the electronic and magnetic structures are highly sensitive to the intricacies of the crystallographic structure, particularly the rotation and tilting of the IrO_6 cages. External pressure serves as a direct means to manipulate these characteristics. Under high pressure, fascinating phenomena have emerged, including the persistence of the insulating state up to an extreme pressure of 185 GPa, a sequence of magnetic transitions culminating in a quantum paramagnetic phase around 20 GPa. However, a dearth of information exists concerning the low-energy electronic band structure. To address this gap, we conducted time-resolved reflectivity measurements under pressures up to 14 GPa. Within the low-pressure range below 10 GPa, anomalies in the temperature-dependent reflectivity transients exhibit a trend akin to the Néel temperature. Yet, as pressure increases further, the temperature associated with these anomalies rises and deviates from the monotonically decreasing magnetic ordering temperature, thereby unveiling a mysterious underlying mechanism governing the relaxation dynamics.

In addition to the breaking of inversion symmetry, Weyl topology can also arise from the breaking of time reversal symmetry in magnetic systems, offering a fertile ground for investigating the intricate relationship between magnetism and topological order. Endeavors have been undertaken to manipulate magnetism as a means to tune the topological electronic band structure. Notably, the well-established ferromagnetic Weyl semimetal, $Co_3Sn_2S_2$, has garnered significant attention due to its intriguing magnetic anomalies persisting below the Curie temperature. Further investigations have revealed that the distribution of magnetic domains and domain walls plays a pivotal role in elucidating these anomalies. Herein, we report the observation of domain structures using a wide-field Kerr microscope and the manipulation of

said structures employing a mid-infrared laser and magnetic field. This study not only sheds light on domain-related properties but also holds promise for uncovering exotic topological phenomena exhibited at domain boundaries.

PUBLISHED CONTENT AND CONTRIBUTIONS

Li, Chen et al. (July 2022). “High-pressure control of optical nonlinearity in the polar Weyl semimetal TaAs”. en. In: *Physical Review B* 106.1, p. 014101. ISSN: 2469-9950, 2469-9969. DOI: 10.1103/PhysRevB.106.014101. URL: https://link.aps.org/doi/10.1103/PhysRevB.106.014101 (visited on 06/05/2023).

C.L. performed the experiment, performed the simulation, analyzed the data, and wrote the paper.

TABLE OF CONTENTS

LIST OF ILLUSTRATIONS

LIST OF TABLES

Number *Page*

Chapter 1

INTRODUCTION

1.1 Pressure Tuning of Transition Metal Compounds

The emergence of quantum materials has provided researchers with an opportunity to delve into the intricate interplay among different degrees of freedom (DoF), including charge, orbital, spin, and lattice. This exploration has led to the discovery of exotic phases exhibiting extraordinary electrical, magnetic, and optical properties that cannot be explained by classical or low-level quantum mechanics. Notably, 5d transition metal compounds (TMCs) stand out as a remarkable category of quantum materials, possessing distinctive characteristics such as the competition between interactions of different DoF with comparable strength. These interactions include on-site Coulomb interaction (U) , kinetic hopping (t), spin-orbit coupling (SOC, ζ), crystal electric field (CEF) splitting (Δ_{CF}), and Hund's exchange coupling (J_H). In electron-correlated systems like these, the intricate interplay of these complex interactions gives rise to a wide variety of exotic phenomena, including SOC-assisted Mott insulators, unconventional superconductivity, magnetism, multiferroicity, and topological states of matter (Witczak-Krempa et al., 2014; Georges, Medici, and Mravlje, 2013; Rau, E. K.-H. Lee, and Kee, 2016).

To understand the behavior of these materials, it is essential to explore their responses to external stimuli. Various techniques such as the application of high magnetic fields, pressure, uni- or bi-axial strain, chemical doping, electrostatic gating, and heterostructuring can tune the strength of competing interactions and shift the delicate balance between coexisting and competing ground states, leading to a rich diversity of quantum phases and transitions between them.

Among the various techniques available for manipulating the microscopic phase of matter, hydrostatic pressure stands out as an exceptionally versatile tool with several advantages over other methods. By exerting pressure on the sample, the interatomic distance and bonding angles can be directly altered. Most solids exhibit bulk moduli in the range of 20 to 200 GPa, and applying a pressure of 10 GPa can compress volumes by approximately 5% to 50%, resulting in noticeable changes in electronic energies (Dunstan and Spain, 1989). In addition to commonly used tuning methods such as temperature and magnetic field, the introduction of pressure as an

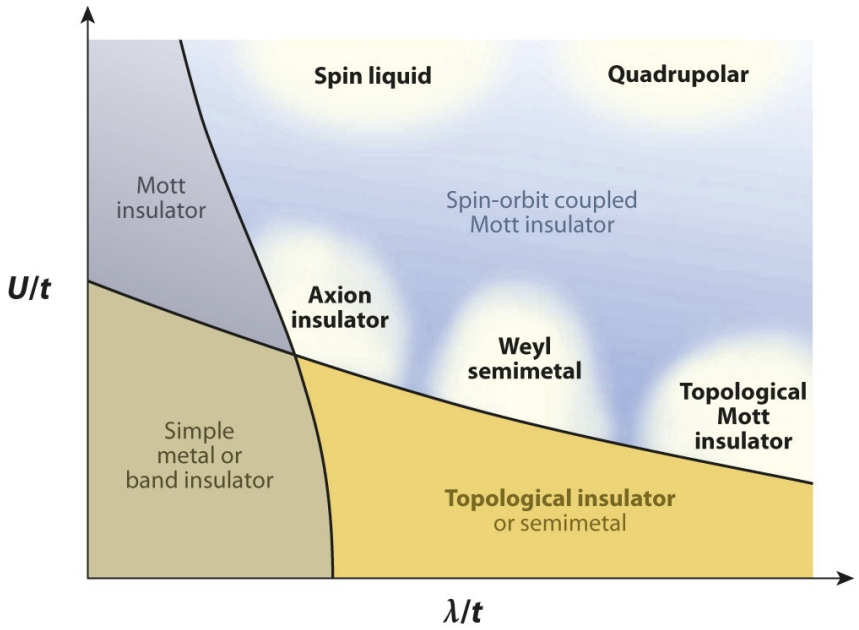

Figure 1.1: Sketch of a generic phase diagram for electronic materials in terms of the interaction strength U/t and spin-orbit coupling λ/t. The figure is adopted from Witczak-Krempa et al., 2014

additional dimension allows for the exploration of different phases and ordering in materials that cannot be achieved through alternative tuning techniques. This approach has led to the discovery of novel electronic states that are unique to the high-pressure regime. Moreover, the continuous tuning capability of pressure facilitates the investigation of quantum phase transitions and critical phenomena, enabling the probing of underlying physics. Furthermore, unlike chemical doping or strain engineering, the application of hydrostatic pressure does not introduce chemical impurities or alter the symmetry of the crystal structure. Consequently, hydrostatic pressure offers a clean, effective, powerful, and systematic approach to explore the fundamental physics of quantum materials, potentially leading to the discovery of new materials with exceptional properties.

Mott insulator-to-metal transition

The phenomenon of the Mott insulator, characterized by half filled bands, stands as a remarkable example that defies conventional band theory. It is a manifestation of strong electron correlations, where the Coulomb repulsion impedes the electrons from moving freely and forming a conducting state. In the Hubbard model,

$$H = -t \sum_{\langle ij \rangle, \sigma} (c^{\dagger}_{i\sigma} c_{j\sigma} + c^{\dagger}_{j\sigma} c_{i\sigma}) + U \sum_{i} n_{i\uparrow} n_{i\downarrow} \tag{1.1}$$

the on-site Coulomb interaction term U competes with the kinetic hopping term t. At large U/t ratios, the system undergoes a Mott transition to a correlated insulating phase with localized electrons. Due to the Pauli exclusion principle, the spins of neighboring electrons tend to align opposite to each other, which can be understood through virtual hopping or exchange processes. Consequently, the Mott insulating state is often accompanied by an antiferromagnetic (AFM) ground state, although this is not always the case Vasiliev et al., 2005; Erickson et al., 2007; Watanabe et al., 2012.

In the limit of large U/t and an average of one electron per site, charge fluctuations become negligible, reducing the Hamiltonian to an equivalent Heisenberg one:

$$H = -J \sum_{\langle ij \rangle} \mathbf{S}_i \cdot \mathbf{S}_j \tag{1.2}$$

where $J = -4t_{ij}^2/U$ represents the exchange constant, and $\mathbf{S}_i$ and $\mathbf{S}_j$ are quantum spin-S operators. Although most Mott insulating TMCs exhibit AFM ordering, ferromagnetic (FM) ordering may also arise in specific cases due to Hund's coupling, as observed in $NaCrGe_2O_6$ (Vasiliev et al., 2005) and Ba_2NaOsO_6 (Erickson et al., 2007). Additionally, Mott insulators can adopt paramagnetic states, such as disordered spin liquid phases in frustrated geometries, as observed in EtMe3Sb[Pd(dmit)2]2 (Watanabe et al., 2012).

In 5d TMC, the unique nature of Mott insulators is further complicated by the presence of SOC and CEF splitting, which compete with the effects of Coulomb interaction and kinetic hopping, as well as Hund's coupling. For instance, in iridates, the strong SOC drives the system into a $J_{eff} = \frac{1}{2}$ state, where the degeneracy of the t_{2g} orbitals is lifted, resulting in a SOC-assisted Mott insulating phase. This behavior is exemplified by the insulating properties observed in Sr_2IrO_4 (B. J. Kim, Jin, et al., 2008) and Ba_2IrO_4 (Okabe et al., 2011). These compounds exhibit exotic magnetic and electronic properties due to the intricate interplay between SOC and U.

For a sufficiently small U/t ratio, the Hubbard model typically describes a metal. As U/t is increased from zero, a quantum phase transition occurs from a metal to an insulator, known as the Mott transition (Imada, Fujimori, and Tokura, 1998). This transition can be achieved through either band-filling control or bandwidth control. In the former, the electron concentration and the position of the Fermi level are altered by doping, leading to insulator-to-metal transition (IMT). A classic

example is the IMT observed in V_2O_3 induced by Cr doping, where the additional electrons occupy the vanadium 3d band, causing the Fermi level to shift into the Mott gap (Hansmann et al., 2013; Lupi et al., 2010). In the latter method, the Mott insulator is transformed into a metal by reducing the strength of the Coulomb interaction or increasing the hopping amplitude, resulting in a narrowing of the Mott gap. The application of pressure, which enhances the overlap of wave functions and increases hopping strength, generally favors the metallic state. Alternatively, hydrostatic pressure can induce Mott transitions by tuning the U_{eff} through spin-crossover transitions (discussed in the next section). U_{eff} is defined as $U_{eff} = E(d^{n+1}) + E(d^{n-1}) - 2E(d^n)$. In compounds containing Fe^{3+} or Mn^{2+} ions, the high-spin to low-spin transition reduces U, facilitating the IMT. Additionally, under pressure, structural transitions or distortions can also trigger changes in the electronic structure and, consequently, affect the material's conductivity. However, due to the frequent co-occurrence of spin-crossover transitions and structural transitions, determining the driving force behind the pressure-induced Mott insulator-to-metal transition can be challenging.

In contrast to a Mott transition, where the transition from metal to insulator is driven by changing the bandwidth or filling parameter, in the case of weaker U/t, the onset of AFM order alone can be sufficient to create an insulating gap. The establishment of AFM ordering induces a change in the unit cell size and leads to the folding of the Brillouin zone, resulting in band splitting at the zone boundary and ultimately leading to an insulating state. Unlike the Mott transition, the so-called Slater transition exhibits the characteristic that the temperature of the IMT coincides with the temperature of the magnetic transition, and the size of the charge gap depends on the magnetic order parameter.

Spin crossover transition

Crystal electric field (CEF) splitting is a pivotal phenomenon that governs the electronic structure of TMC. It arises from the interaction between the transition metal ion's d orbitals and the surrounding ligands in the crystal lattice. This interaction causes the degeneracy of the d orbitals to be lifted, leading to the formation of energy levels that depend on the local symmetry of the crystal field and the Coulombic interaction between the ligands and the metal ions. For example, in an octahedral MO_6 with O_h symmetry, the d orbitals overlap with the $2p$ orbitals on the oxygen sites. The $d_{x^2-y^2}$ and d_{z^2} orbitals have a higher energy due to a larger overlap with the metal-ligand bonds. On the other hand, the d_{xy}, d_{yz}, and d_{xz}

orbitals, with lobes pointing between the metal-ligand bonds, have lower energy. The original degenerate five-fold d level splits into a lower-energy triplet t_{2g} level and a higher-energy doublet e_g level. The energy difference between these two levels is denoted as Δ_{CF}. In the case of $5d$ TMCs, the CEF splitting is generally larger than in $3d$ or $4d$ systems due to the extended nature of the $5d$ orbitals and their stronger interaction with the ligands. Hydrostatic pressure directly decreases the metal-ligand bond lengths, thereby increasing the d-p orbital hybridization and the CEF splitting. It is important to note that the degeneracy of the t_{2g} and e_g states can be further lifted by factors such as the rotation of the octahedral cage or Jahn-Teller distortion. Although the intra-state splitting is generally smaller than the main inter-state splitting, it plays a critical role in determining the insulating or metallic behavior in certain cases. In such situations, the effect of hydrostatic pressure on the CEF and electronic band structure can be complex and difficult to predict.

In TMCs, the partially filled d orbitals can adopt different spin states, namely high-spin (HS, all unpaired), low-spin (LS, all paired), or intermediate-spin (IS) configurations (Vankó et al., 2006). The stability of these spin states is primarily determined by the balance between Hund's exchange coupling and CEF splitting. Hund's exchange coupling tends to equalize the populations of different orbitals, allowing electrons distributed in all available orbitals to take advantage of the reduction in Coulomb repulsion through intra-atomic exchange, thus favoring the HS state. Conversely, CEF splitting leads to energy differences between orbitals. This splitting opposes the equalization of orbital populations and can favor LS or IS states if the energy gap surpasses the benefits gained from Hund's coupling. Therefore, the competition between Hund's coupling and CEF splitting governs the spin state selection in TMCs. The delicate interplay between these factors makes the determination of the dominant spin state a complex and intriguing aspect of understanding the behavior of TMC.

The spin-crossover transition (SCT) refers to the transition between different spin states in response to an external stimulus. In $3d$ transition metal oxides, the CEF splitting is typically around 1 - 1.5 eV, while J_H hovers around 0.8 - 0.9 eV, favoring the HS state under ambient conditions. In contrast, $5d$ transition metal oxides, with their more extended $5d$ wave function, exhibit a larger Δ_{CF} ($\sim$ 2.5 - 3.0 eV) and a smaller J_H ($\sim$ 0.5 eV), leading to a preference for the LS state, as observed in iridates. (Typical energy scales for correlations are taken from Table 1.1 in Vale,

2017).

The SCT can be induced by applying pressure, which enhances the strength of the CEF splitting. It is important to note that the ionic radii of HS and LS states of the same ion differ significantly, with LS ions being smaller than their HS counterparts. Therefore, the application of pressure tends to stabilize the LS state, promoting the transition from HS to LS and resulting in a substantial reduction in volume.

Quantum spin liquid

Quantum spin liquid (QSL) represents a prime example arising from the interplay of competing forces (Balents, 2010). They are characterized the absence of long-range magnetic order even at absolute zero temperature resulting from quantum fluctuation, despite being subject to strong magnetic correlation. QSLs have piqued the interest of the condensed matter physics community owing to their exotic properties, including the emergent gauge fields and fractional particle excitations, which renders QSLs a unique class of materials, distinguished from conventional magnets. Nonetheless, despite extensive investigations spanning several decades, QSLs have remained an enigma with only a few putative candidates identified. The recent utilization of hydrostatic pressure has emerged as a promising approach for exploring and inducing QSLs, offering a novel tool to probe the behavior of these intriguing materials (Biesner and Uykur, 2019).

Hydrostatic pressure has been shown to effectively destabilize the competing interactions that govern the magnetic state, including super-exchange and dipolar coupling, CEF interactions, and Dzyaloshinskii–Moriya (DM) interaction. For example, in the Kagome lattice material Herbertsmithite $ZnCu_3(OH)_6Cl_2$, a quantum phase transition from a QSL ground state to an ordered antiferromagnetic phase was detected at 2.5 GPa via susceptibility measurements (Kozlenko et al., 2012). Despite the preservation of the crystal structure's $R\bar{3}m$ symmetry, the decrease in Cu-O bond length and trigonal distortion caused by CuO_4-plane tilting reduced the DM versus Heisenberg interaction ratio, leading to magnetic ordering. Similarly, ordered phases have been observed in the spin ice candidates Pyrochlore oxides $Yb_2Ti_2O_7$ (Kermarrec et al., 2017) and $Tb_2Ti_2O_7$ (Mirebeau et al., 2004) under low pressure. These studies demonstrate the sensitivity of such a degenerated antiferromagnetic ground state manifold to pressure perturbations, establishing pressure as an effective tool for tuning the magnetic properties of frustrated compounds. As an alternative, pressure can be used to produce new frustrated magnets by treating

samples under pressure. Both the 6H-B phase of $Ba_3NiSb_2O_9$ and the 3C phase of $Ni_{\frac{2}{3}}Sb_{\frac{1}{3}}$ can be obtained in this manner, both of which exhibit no magnetic ordering down to 0.35 K and a saturated susceptibility, indicating QSL states (Cheng et al., 2011).

The quest for QSL stands as a central and compelling pursuit within the realm of frustrated magnets. External pressure emerges as a potent and versatile instrument, capable of deftly modulating the intricate interplay of competing magnetic couplings, thereby offering the tantalizing potential to drive and stabilize the elusive QSL state. Nonetheless, these explorations are not without their challenges. Undesirable structural distortions and intricate phase transitions conspire to complicate the interpretation of experimental findings. Technical challenges associated with performing low temperature experiments under pressure may restrict the observation of certain excitations and hinder the differentiation between various possible ground states. Notwithstanding these hindrances, the pursuit of QSLs using pressure remains a dynamic and active field of study.

Topological superconductivity

Topological superconductivity (TSC) is a fascinating area of research due to the prospect of the emergent Majorana fermions (MF), which can potentially serve as topological qubits, the basic building block for quantum computer. MF, a solution with real wave functions for the relativistic Dirac equation, is a particular class of particles which are identical to their antiparticle in all aspects. With non-Abelian Anyonic statistics, when two MFs are exchanged, their quantum state is transformed in a nontrivial way, which is topologically protected from the details of operation. In an MF-based quantum computer, topological qubits are encoded in the nonlocal degrees of freedom of multiple MFs. The qubits are robust against decoherence and external noise, which is a major challenge for the stability of traditional qubits. This property makes MFs a promising approach for building fault-tolerant quantum computers and other applications in quantum information storage and processing.

In a solid state, the MFs are created as a mixture of electron and hole operators. This can be achieved in intrinsic topological superconductors (Wilczek, 2009). For example, in the p-wave superconductor, where Cooper pairs have orbital angular momentum 1 (p_x + ip_y - wave), it is predicted that the vortex cores can host MFs. Alternatively, it can be achieved in artificially engineered superconductors, for example, by bringing a topological insulator in proximity to a conventional

superconductor.

Additionally, the application of hydrostatic pressure has been identified as a viable means to induce superconductivity in certain TIs. High pressure has been serving as a means of manipulating and inducing SC. Pressure facilitates the induction of SC phases and/or increases Tc in numerous elemental materials; by driving competitions between electronic and magnetic orders, both Cu-based and Fe-based unconventional SC exhibit a dome-like phase boundary in the PD. Notably, hydrogen-rich systems have produced the staggering achievement of a record-high Tc via pressure levels of up to 300 GPa (Gor'kov and Kresin, 2018; P. Kong et al., 2021; Dasenbrock-Gammon et al., 2023). Within the realm of topological materials, the application of pressure has enabled the realization of SC in topological insulators (TI), Dirac semimetals (DSM), and Weyl semimetals (WSM), thereby establishing them as promising candidates for TSC (Yupeng Li and Z.-A. Xu, 2019; M. M. Sharma et al., 2022).

One example of a TI that exhibits pressure-induced superconductivity is Bi_2Te_3, which is a prototypical 3D TI with a non-trivial topology. At ambient pressure, Bi_2Te_3 is an insulator with a bulk energy gap of about 0.3 eV. However, when subjected to high pressure , Bi_2Te_3 undergoes a transition to SC state at around 3 GPa (J. L. Zhang et al., 2011). When further increasing pressure, another SC transition occurs which accompanied by a structural transition from a rhombohedral $R-3m$ structure to a monoclinic $C2/m$ structure. Furthermore, according to density functional theory (DFT) calculations, due to the unchanged structure and the small change in lattice parameters, the topologically nontrivial electronic states are expected to persist in the low-pressure SC state (3 GPa - 8 PGa), which could potentially induce MFs due to the proximity effect of the SC in bulk (J. L. Zhang et al., 2011). A similar phase transition sequence is also detected in Sb_2Te_3, in which the insulator to SC transition occurs before the structural transition. In contrast, other TIs, such as Bi_2Se_3 (Yonghui Zhou, X. Chen, et al., 2016; P. P. Kong et al., 2013), BiTeX (X = Cl (Ying et al., 2016; VanGennep et al., 2017), Br, and I (Qi et al., 2017)), upon being pressurized, experience structural transitions at the same time as or even before the SC appears.

SC phases have also been detected in Dirac semimetals (DSM) and Weyl semimetals (WSM). Examples of the former includes Cd_3As_2 (He et al., 2016), $ZrTe_5$ (Yonghui Zhou, J. Wu, et al., 2016). However, In both cases, the SC states are in structural phases different than the ambient ones, which, as suggested by a combination of

high-pressure X-ray diffraction measurements and DFT calculation, don't support 3D DSM. Examples of the latter include the type I WSM TaP, and type II WSM WTe_2, $MoTe_2$ etc. However, most of them are accompanied by a structural transition that changes the topology of electronic bands. Since the TSC requires the coexistence of SC and topologically nontrivial states, theoretical and experimental confirmation of both plays a key role in the search for TSC. Unfortunately, it is currently not possible to perform experiments such as angle-resolved photoemission spectroscopy (ARPES) and scanning tunneling microscope (STM), to confirm the nontrivial topology under high pressure. Despite the difficulties in confirmation, by tuning the electronic states, pressure is a valuable tuning knob for searching for and investigating TSC, which cannot be naturally synthesized.

Chapter 2

EXPERIMENTAL TECHNIQUES

2.1 High-Pressure Technique

In the field of condensed matter physics, several commonly used techniques are employed to apply high pressures to materials and investigate their properties under extreme conditions. These techniques enable scientists to explore the behavior of matter under compression and gain insights into various physical phenomena. One widely used method is the diamond anvil cell (DAC), which utilizes two opposing diamond anvils to exert pressure on a sample placed between them. Additionally, dynamic shock wave compression techniques allow us to achieve conditions comparable to those of the Earth's core and study the material's response to large sudden impacts. In this technique, gun powder and/or compressed gas are used to launch at the material at high speed. The collision generates a strong shock wave that rapidly compresses and heats the sample. However, in a shock plane shock-wave experiment, the compression is essentially a one-dimensional strain along the shock prorogation. Only when the subject material is fluid, the stress configuration is hydrostatic.

Diamond Anvil Cell

The diamond anvil cell (DAC) is the most widely employed high-pressure technique in condensed matter physics and materials science research. It consists of two opposing diamond anvils, typically made from synthetic diamonds due to their exceptional hardness and transparency. The anvils are shaped into small flat tips, creating a small culet area where the sample is placed. The sample, usually in the form of a small single crystal or powder, is compressed between the two diamond anvils to generate high pressures.

To apply pressure, the diamond anvils hold a metal gasket, which acts as a seal and allows for the containment of a pressure-transmitting medium. The gasket material can vary depending on the pressure and temperature range required for the experiment. Common choices include rhenium, tungsten, or stainless steel, which exhibit high strength and resistance to deformation under pressure. To create pressure, the two diamond anvils are brought closer together by adjusting the height of the DAC assembly using a loading mechanism, such as a hydraulic or mechanical press. As

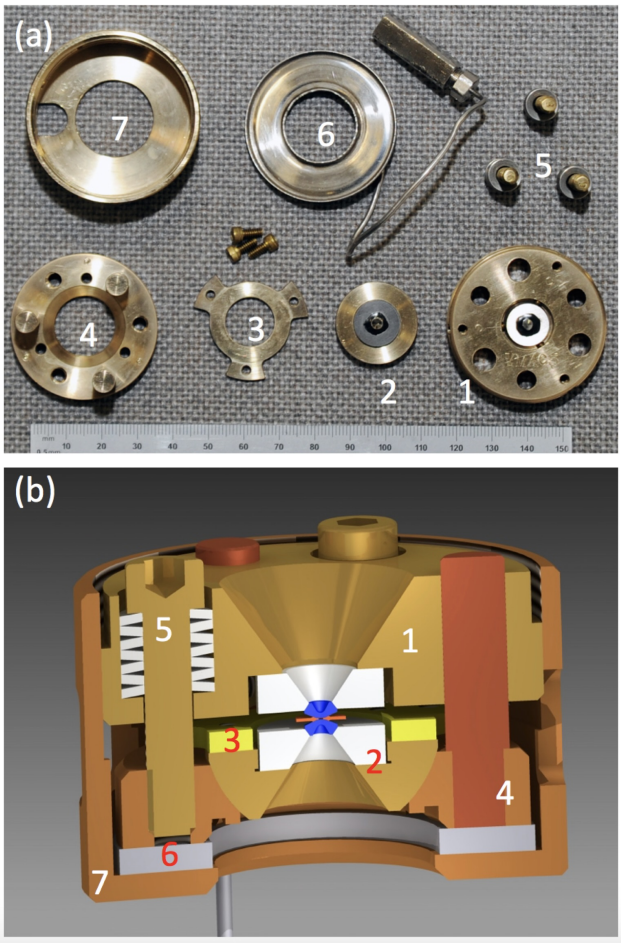

Figure 2.1: 3-pin diamond anvil cell. (a) Photograph of actual cell components. Numbers correspond to those in panel b. (b) Cross-sectional view of a modified three-pin Merrill-Bassett type diamond anvil pressure cell. (1), (2): Upper and lower pieces of the cell body. Pins press-fit into the lower part to align the two pieces with each other. (3),(4): Rear-perforated diamonds mounted on tungsten carbide seats; one seat is mounted on a rocker for angular alignment. The partially-perforated diamond anvils are specially designed to remove background signals from the diamonds in scattering experiments. A retaining ring (5) holds the rocker and seat in position. Screws and stacks of Belleville disc washers (6) provide the sealing force and initial room-temperature pressurization. A helium bellows actuator (7) and retaining cap (8) allow for *in situ* cryogenic pressurization. The figures are adapted from Y. Wang, 2018

the anvils move closer, the sample placed at the culet area experiences compressive forces, leading to an increase in pressure. The pressure can be determined indirectly by measuring the known compression of a reference material, such as ruby fluorescence or a pressure-sensitive material, embedded alongside the sample.

The diamond anvils themselves play a crucial role in the DAC. Due to their exceptional hardness, they can withstand extremely high pressures without breaking. Moreover, their transparency allows for the use of various characterization techniques, such as optical microscopy, Raman spectroscopy, and X-ray diffraction, to study the behavior of the sample under pressure. In specific cases, experiments necessity diamonds with customized shapes or materials due to the undesired signals produced by diamonds.

The diamond anvil cell offers several advantages for high-pressure experiments. It can generate pressures in the range of megapascals (MPa) to hundreds of gigapascals (GPa), covering a broad spectrum of pressure regimes. It is also compatible with a wide range of temperature conditions, including cryogenic temperatures (Palmer 2015) and high-temperature environments.

However, the diamond anvil cell also has certain limitations. The sample size is typically limited due to the small culet area, which restricts the types of measurements that can be performed. Furthermore, the pressure distribution within the sample can be non-uniform, leading to challenges in interpreting experimental data accurately. Efforts are made to improve the pressure distribution through various techniques, such as using pressure-calibrating materials or employing different gasket and liquid medium designs.

Despite these limitations, the diamond anvil cell remains a valuable tool in the field of high-pressure research, enabling scientists to explore and understand the properties of materials under extreme conditions. Its versatility, reliability, and ability to reach ultrahigh pressures make it an indispensable technique for investigating the fundamental behavior of matter and discovering novel physical phenomena.

The DAC we used for the experiments discussed in this thesis is a 3-pin Merill-Basset type DAC, the details of which can be found in Y. Wang, 2018 Chapter 2. 2.1 shows a photo of the cell components (a) and a schematic of the cell assembly (b). Both figures are adapted from Y. Wang, 2018. To incorporate the sizable DAC into the cryostat for cryogenic measurement, a customized dome and shielder were machined (2.2).

DAC preparation procedure

Operating a diamond anvil cell (DAC) entails a precise and intricate procedure that allows for the generation of high pressures in a controlled laboratory setting.

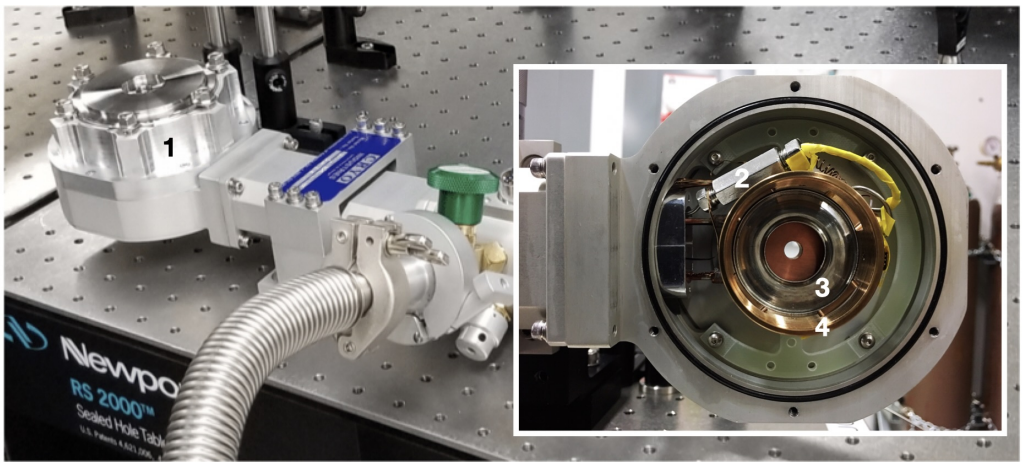

Figure 2.2: Photographs showcasing the specially customized cryostat designed for pressure measurement. Key elements within the photograph include: 1) The custom dome designed to accommodate the sizable DAC; 2) The connector facilitating the connection between the actuator bellow and the capillary linked to the room-temperature helium gas reservoir; 3) The actuator bellow responsible for pressurizing the DAC; and 4) The secure cage ensuring the stability of the DAC.

- Choose material: use diamond, and choose the suitable shape and size of the diamonds for specific experiments and the target pressure range.
- Mount the diamond: Glue the diamonds onto the seats with jigs and harden the epoxy. Make sure the diamonds are well-centered.
- Clean cell and diamonds: Clean the cell and diamonds with acetone, methanol, or ethanol. Make sure that acetone does not attack the glue holding diamonds
- Align cell: Align the diamonds translationally and rotationally. Make sure that the polygon culet edges for the upper and lower diamonds coincide when the cell is gently closed. Tune the diamond tilting angle. Make sure the number of Newton rings is equal to or less than five. Even if no diamond is replaced from the last measurement, fine alignment should be performed.
- Prepare single-crystalline sample: Polish and cut the sample down to a desired size. In general, to maintain a good hydrostatic condition, the sample-to-cell ratio should be kept below 1/10 throughout the whole experiment.
- Prepare gasket: Punch out a small round sheet piece of gasket. Pre-indent it into the desired thickness and drill a hole in the center. Typically, the diameter of the hold is 1/2 to 1/3 of the culet size, and the indented thickness

is approximately 1/3 of the hole diameter which determines the initial size of the chamber.

- Load sample and ruby: Mount the gasket on the diamond tip while maintaining the orientation. Carefully place the sample and ruby spheres in the gasket hole area. For optical measurement in a vertical geometry, glue such as N grease is required to keep the sample in place.
- Perform measurement under ambient pressure.
- Seal the cell: When using a mixture of organic fluid as a liquid medium, after dropping liquid into the gasket hole, quickly and symmetrically apply force with the screws to seal and pressurize the cell. If using condensed noble gases as the liquid medium, please refer to other references.
- Check: Check the bubble under a microscope and measure the pressure through ruby fluorescence. If a bubble appears or no pressure is added, repeat the last step.
- Load pressure: Connect the capillary line. After securing the DAC into the shell, pump He gas into the membrane to engage and tune in-cell pressure.
- Start measurement: For cryogenic measurement, mound additional thermal sensor on the DAC, and start measurement.

Gasket preparation

Gasket preparation: The gasket used as the wall of the pressure chamber is made of a small thin piece of flat metal with a centered hole. To construct the metal into the desired shape and prevent distortion during pressurization, the gasket material should be both hard and ductile. Commonly used materials include Re, CuBe, Stainless steal, and a series of Ni dominated superalloys. In most of our pressure measurements, we use MP35N, a nonmagnetic, nickel-cobalt alloy that maintains acceptable ductility and can be hardened by elevated temperature. A detailed discussion of its properties compared with other materials can be found in Palmer et al 2015.

The gasket should be pre-indented to a desired thickness by manually pressurizing the aligned DAC with screws. The manual force should be applied by turning at a small angle each screw one by one to uniformly load pressure onto the gasket, which also helps with avoiding DAC alignment change. The dependence of the indented

thickness on the turning angle of screws is determined by gasket material, diamond culet size, and the design and assembly of DAC. Achieving a target thickness requires experience. Over-pressurization can lead to the diamond break. Therefore, keeping a record of the turning angle and the corresponding indented thickness is recommended. Some also recommend the force should be increased by applying it a few degrees at a time and then completely removing it, which can further prevent breaking the diamond. In the subsequent pressure measurement, the orientation of the gasket should be kept the same as when it is indented. Use a scalpel to mark it. After the indentation, we utilize Electrical Discharge Machining to drill a centered and vertical hole. The hole position of both the front and back surface should be checked under a microscope. Finally, heat treatment for hardening should be done depending on the material's needs.

Typically, the diameter of the hole should be about $1/3$ to $1/2$ of the culet diameter, and the gasket thickness should be about $1/3$ of the hole diameter. To maintain a near-hydrostatic condition, the sample-to-cell (STC) volume ratio should be kept below $1/10$. The prepared gasket determines the initial STC ratio. However, during one or a series of compression, the cell room inevitably shrinks. A thinner gasket allows a higher maximum pressure. However, it limits the cell volume. Therefore, the balance should be taken depending on the desired sample size as well.

Sample preparation and handling

Handling small samples for the DAC can be the most tedious and difficult of all operations.

To achieve optimal hydrostatic and homogeneity conditions, we aim to minimize the sample size while maintaining a certain surface area for accurate optical measurements. Specifically, our practice involves keeping the content-to-cell ratio below 1:3 and ensuring the lateral dimension of the sample is greater than 80 um when using a beam spot with a diameter of approximately 40 um. In the initial stage of sample preparation, we thin and cut the sample to an appropriate dimension. We polish it to a thickness of 10-20 um while preserving its as-grown surface. During polishing, thin wires of varying gauges are placed around the sample as markers for the remaining thickness. When cutting the sample, care must be taken to prevent it from jumping out of view. This can be avoided by securing it with grease or immersing it in alcohol. To store the sample, it can be secured with grease on a slide or transferred to a slightly adhesive surface such as tape. It is crucial to avoid

cutting the sample on soft tape as this can result in crushing.

Moving the sample and ruby onto the DAC is a delicate process that requires precision and skill to minimize the risk of losing the sample. There are a variety of techniques and tools, and the choice must finally be made according to personal preference and experience. The sample should be lifted, deposited, and pushed around, and this is typically done with a sharp, pointed instrument. Flexible springy tools must be avoided since the sample will easily be sent flying. In our operation, we utilize thin shovel-like tips made by breaking the wooden sticks of Q-tips. The shovel-like tip can easily pick up the sample flake, and the wooden fibers help to secure the sample. When delivering the sample to the diamond surface, we use either another wooden tip to swipe the sample down onto the glue in the center of the diamond culet, or flip the tip and drop the sample onto the diamond culet. However, both methods have their drawbacks, such as the sample getting stuck onto the tip or being lost during flipping. An alternative method involves using a needle with a trace of glue to pick up the sample by the edge, which has a higher success rate but requires the use of glue.

During the subsequent optical measurement, a vertical configuration is utilized, requiring the cryostat and DAC to stand up. To maintain the sample's position and keep its surface normal to the optical axis, glue is needed. However, the use of glue can compromise the hydrostatic condition, particularly in low-temperature measurements. To circumvent this issue, a horizontal optical measurement configuration should be employed.

Loading the ruby sphere onto the DAC is relatively straightforward, utilizing the electrostatic attraction of a sharp needle tip to transport and deposit it. After depositing the sample and before the rubies, we lower the gasket onto the diamond culet, using the gasket hole to verify that it does not push the sample. Once the sample, rubies, and gasket are in place, the cell can be sealed.

Liquid medium, pressure loading and tuning

Liquid medium

In addition to the selection of an appropriate gasket, the choice of liquid mediums assumes a paramount role in maintaining a favorable sample-to-chamber volume ratio and ensuring optimal hydrostatic conditions. Deviations in these parameters can severely compromise the quality of pressurized single crystals. Within the realm of diamond anvil cells, two primary categories of pressure-transmitting mediums

prevail condensed noble gases, encompassing helium, neon, nitrogen, and argon, and mixtures of organic fluids such as methanol and ethanol in a 4:1 ratio. Notably, Tateiwa and Haga (2009) conducted a comprehensive evaluation of 14 liquid media, spanning pressures up to 10 GPa and temperatures as low as 4.2 K. They gauged the nonhydrostaticity of the pressure by scrutinizing the broadening effect of the ruby R1 fluorescence line. Through a direct comparison of the R1 fluorescence line widths, they observed significantly diminished broadening effects in condensed gas media compared to other mediums. Feng et al. (2010), in their examination of individually positioned ruby spheres, noted comparable inhomogeneity between helium and methanol: ethanol 4:1 mixtures up to 20 GPa when measuring the individual R1 peak positions. However, by assessing the averaged line width, they discovered discernible anisotropy, with helium medium exhibiting superior performance beyond 10 GPa. Conversely, the crucial factor of the sample-to-cell volume ratio becomes particularly salient, especially when considering the rearrangement of pressure distribution. Noble gases as a medium yield substantial cell shrinkage at low pressures (below 10 GPa) due to their significant compressibility, thereby influencing the sample properties. Nevertheless, Feng et al. emphasized that while the choice of the liquid medium is pivotal for achieving a suitable pressure environment, other sample chamber parameters also exert an influential role.

In our pressure measurements below 20 GPa, balancing operational convenience and performance, we have adopted a 4:1 mixture as the liquid medium. However, as we delve into higher pressure regimes, helium medium emerges as the recommended choice, given its more favorable characteristics.

Pressure loading Once the sample and ruby spheres are properly deposited and the gasket is well seated, the cell may be sealed with a liquid medium. A droplet of the mixture is placed onto the gasket hole. After closing the cell, check visually for bubbles and finger-tighten the screws. Use a screwdriver to incrementally turn each screw, ensuring the pressure is consistently and uniformly applied to the diamond culet, until sealing the cell. It is essential to note that the requisite pressure and corresponding turning angle will vary depending on the anvil dimensions, gasket material, and initial gasket thickness. Therefore, these parameters should be determined through prior experience. To minimize the rate of evaporation and impede bubble formation, it is advisable to complete the above process as expeditiously as possible. Moreover, some literature suggests that the cell should be cooled on ice or in a refrigerator before loading alcohol.

Pressure tuning

The 3-pin Merrill-Bassett type DAC we use supports both the *in-situ* variable pressure tuning mechanism via a gas-driven actuator and the mechanical loading through screws. As compared to mechanical loading, which necessitates the removal of the DAC from the cryostat and loading at room temperature, the *in-situ* pressure increase is more convenient. This not only saves a considerable amount of time from thermal cycling but also maintains the sample's position during optical measurement and pressure-dependent measurement at a fixed low temperature, which is crucial.

The gas-driven bellow-based actuator realizes *in-situ* control of cell pressure. As depicted in 2.2, the toroidal bellows are placed in the shell with internal threads mounted on the cryostat cold finger. A stainless steel capillary line (0.50 mm ID, 0.80 mm OD) connects the bellow to a room-temperature He gas reservoir and a manifold. To thermalize the room-temperature helium gas, the steel capillary tubing is wound around the cryostat bobbin. A needle valve in the manifold provides fine control of the pressure applied to the bellow and accurately determines the applied force.

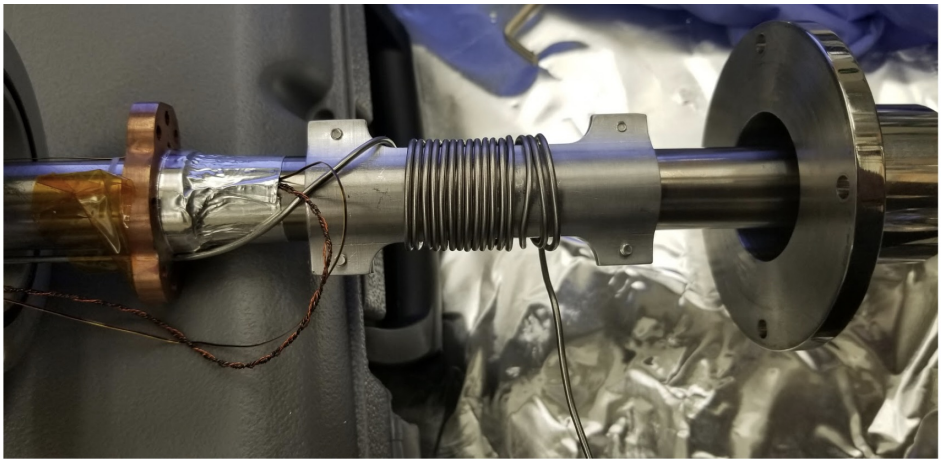

Figure 2.3: A stainless steel capillary line connects the bellow to a room-temperature He gas reservoir and a manifold. To thermalize the room-temperature helium gas, the steel capillary tubing is wound around the cryostat bobbin.

Once the sealed DAC is securely fastened into the shell, He gas can be gradually compressed into the bellow to pressurize the cell. The initial step requires a certain amount of gas to engage the cell, and subsequently, the in-cell pressure begins to increase. Depending on the culet size, one bar on the capillary gauge will correspond to different pressures in the DAC. You can estimate the pressure by taking a ratio

of the membrane area to the culet area. Pressure estimation can be achieved by calculating the ratio of membrane area to culet area. Awaiting several minutes is necessary for the cell to reach equilibrium. During the experiment, it is advisable to maintain a plot of membrane vs. sample pressure and to monitor the gasket shape through an optical imaging system. Nonlinear pressure change or visible distortion of the gasket shape can give an early indication of problems, for instance, an impending gasket failure. If issues arise, special care should be taken, and, if necessary, terminate the experiment to prevent a diamond crush.

It is worth noting that during extreme low-temperature measurements, He-4 can enter the superfluid and solid states. The large thermal conductivity of superfluid He limits the base temperature. On the other hand, solid He-4 may block the capillary line. To avoid this situation, cell pressure adjustment must be performed above the helium melting temperature.

Pressure releasing

To reduce the pressure in the DAC, we should gradually release the bellow pressure. Similar to the pressure loading process, there will likely be no change in the DAC pressure until several bellow bars have been released. However, it is common for the pressure to get stuck at a high level. To perform measurements during the pressure-decreasing process, manual and gradual unscrewing of the DAC *in-situ* while monitoring the pressure change is suggested for room temperature measurements. For low-temperature measurements, a specially designed tool should be employed. However, the pressure decrease is not as smooth as the pressure increase, and it is important to note that measurements taken during the pressure cycling show considerable hysteresis, possibly due to non-invertible physics or the residue pressure inside the sample.

Temperature determination

When conducting low-temperature measurements, utmost care must be taken in mounting an appropriate temperature sensor. Due to the large size of the cell, the original thermal sensor mounted in proximity to the cryostat's cold finger is inadequate in reflecting the actual temperature. In our study, we affixed two additional sensors to the cell and use a small amount of N grease on the surface of the thermometers to ensure good thermal contact. However, due to the distance between the sample and sensors, it is essential to consider the potential for temperature misreporting.

Pressure determination with ruby fluorescence

The precise and expedient determination of sample pressure is of paramount importance, as is the continuous *in-situ* control of pressure. Here, the standard ruby fluorescence method is employed as a manometer. The *in-situ* pressure tunability enabled by the gas-driven actuator and the *in-situ* pressure measurement enabled by the ruby fluorescence allows for experiments to be carried out over a wide range of pressures and facilitate precise steps across abrupt phase transitions.

Ruby fluorescence as manometer

The standard ruby fluorescence method utilizes a tiny luminescent ruby crystal (Al_2O_3 :Cr_2O_3 with typically 0.5 wt % Cr). The spectrum of this crystal exhibits two primary absorption bands, with Y centered at approximately 549 nm, and U at approximately 403 nm. By irradiating the crystal with blue or green lasers, electrons in the Cr^{3+} ion ground state can be efficiently excited into the T1 (corresponding to Y band) and T2 (corresponding to U band) excited states, respectively. Subsequently, non-radiative decay occurs from the Y and U excited states into either the lower E2 state or the upper E2 state which are originated from the crystal electric field splitting, leading to two exceedingly sharp peaks in the ruby fluorescence spectrum, known as R1 and R2. Under pressure, the meta state E2 is lowered, and the R1 and R2 peaks display a quasi-linear redshift. Under ambient conditions, the populations of the upper and lower E2 levels are comparable, resulting in a similar intensity of the R1 and R2 peaks. However, as the temperature decreases, the population of the upper E2 level decreases, leading to the suppression of the R2 fluorescence line. Therefore, we rely on the R1 line location for pressure calculations.

Ruby fluorescence can also be utilized to calibrate the non-hydrostatic condition which leads to a line broadening of the spectral peaks. On the other hand, we can also position ruby pieces in separated locations to check the homogeneity across the chamber.

In terms of the pressure dependence on the R1 peak position, a number of different calibration has been proposed as standards with the differences mainly manifested in the high-pressure range. An extensive discussion can be found in Shilling Hamlin's thesis 2007. In our measurement, we use the formula of $P = A_0 ln(\lambda/\lambda_0)$ with A = 1762.0 adopted from Feng 2010.

Experimental setup

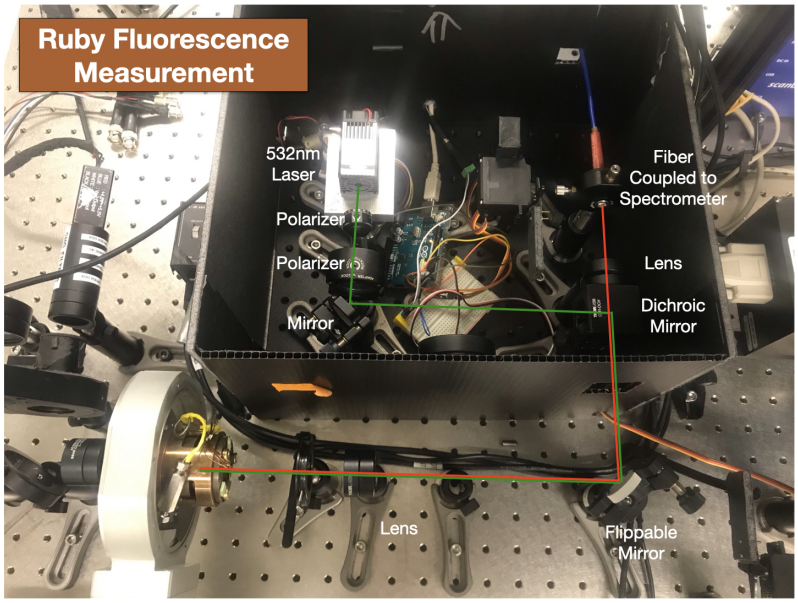

Figure 2.4: Photograph capturing the experimental configuration utilized for the measurement of ruby fluorescence.

2.4 depicts a photograph of the optical setup employed for measuring the ruby fluorescence to determine pressure. A 532 nm Diode-Pumped Solid State (DPSS) green laser is utilized to excite the ruby spheres. A pair of polarizers are implemented to attenuate the laser power, and three mirrors, including a flippable one and a dichroic one, are used to collimate the green laser with the optical axis of the ultrafast optical measurement. The flippable mirror switches between the optical measurement mode and the pressure measurement mode. When using the same focusing objective or lens (L1), the optical path for the former can be kept exactly unchanged, enabling the highly dependable data set through the whole T-P measurement. The red fluorescence light is collected by the same objective or lens (L1) and passes through the dichroic mirror (DM). The 605 nm long-pass DM serves to split the green laser and the radiated light, as well as to eliminate any unwanted short-wavelength reflected beam. The fluorescence is concentrated by a lens (L2) and directed to the entrance of a fiber optic cable that links to the spectrometer.

Typically, the customized spectrometer is necessary to meet the resolution requirements for locating the spectral peak location. In this study, we employed an HR1 spectrometer from ASEQ instruments, featuring an 1800 gr/mm grating that provides a spectral range of approximately 665-735 nm, and a 25um slit or single mode optical fiber, yielding a resolution of 0.07 nm.

In practice, there exist several technical tricks to ensure a dependable determination of pressure. One such method is the subtraction of the averaged background from the spectrum, which significantly assists in pinpointing the location of peaks. Prior to each T-P run, it is imperative to block the illuminating green lasers and measure and average the background spectra with the same integration time employed during the actual measurement, for at least 20 iterations. All ensuing spectra should be normalized with this baseline.

Moreover, the R1 line location not only relies on pressure but also on temperature, which can be affected by the heating of the ruby crystal caused by the illuminating green laser. This heating can distort the pressure calibration. Therefore, to circumvent the resultant heating, an attenuated laser beam, accompanied by an increased integration time, should be utilized.

Furthermore, maintaining the sample at a consistent position throughout the T-P run is crucial in generating dependable and seamless curves. To achieve this, the two mirrors and the dichroic mirror must be fine-tuned to focus the green laser onto the ruby sphere and maximize the fluorescence received by the spectrometer.

Another important aspect to consider is the content-to-cell ratio, which must be limited to prevent the hydrostatic condition from deteriorating. A trade-off must be found between the room occupied by the ruby and the fluorescence signal it yields. Generally, ruby spheres with a diameter of less than 10 μm are used. To assess the hydrostatic condition, the pressure of two ruby spheres located on either side of the cell is measured.

Hydrostatic condition and homogeneity condition

Both the hydrostatic condition and the homogeneity condition are important concepts in pressure measurement, but they refer to slightly different aspects of the pressure distribution within the sample.

The hydrostatic condition refers to a state where pressure is evenly distributed throughout a fluid or solid material, such that it is isotropic, i.e., the pressure is the same in all directions. The hydrostatic condition ensures that the pressure measured is representative of the true pressure of the sample, without any biases or variations caused by pressure gradients.

On the other hand, the homogeneity condition refers to a state where the sample is uniform and homogeneous, i.e., it has the same composition, density, and properties

throughout. The homogeneity condition is essential in pressure measurement, as any non-uniformity or heterogeneity in the sample can result in variations in pressure measurements. For example, if the sample contains air bubbles or impurities, it may not compress uniformly under pressure, leading to non-homogeneous compression and pressure variations.

In summary, while the hydrostatic condition refers to the even distribution of pressure within the sample, the homogeneity condition refers to the uniformity of the sample itself. Both conditions are critical for accurate pressure measurement, and they are often interdependent, as achieving one condition can help to ensure the other.

Incorporation of high-pressure environment and ultrafast laser measurements

The incorporation of high-pressure environment and the femtosecond pulsed laser enables measurements of the dynamic processes occurring within the material under extreme conditions. This enables scientists to capture and analyze the rapid changes in material behavior with exceptional temporal resolution. Additionally, the intense electric fields generated by the ultrafast laser pulses can induce nonlinear responses in the material such as high harmonic generations, providing valuable insights into its structural and electronic symmetry. Furthermore, the combination of ultrafast laser probes with high-pressure environments offers versatility in probing different aspects of the material. By making small adjustments to the experimental setup, researchers can switch to various optical detection techniques, such as Kerr microscopy, photoluminescence spectroscopy, or nonlinear optical spectroscopies, allowing for a comprehensive characterization of the material's properties under high pressure. Overall, the integration of ultrafast laser probes with high-pressure environments opens up exciting opportunities for exploring the behavior of materials under extreme conditions and contributes to advancements in fields such as solid-state physics, materials science, and geophysics.

2.2 Second Harmonic Generation and Time-Resolved Reflectivity Measurements under High Pressure

Second Harmonic Generation under High Pressure

Nonlinear optics is a fascinating field of study that explores the optical properties of materials beyond the realm of linear optics. In nonlinear optics, the induced polarization $P(t)$ can be expanded into multiple terms beyond the linear susceptibility $\chi^{(1)}$. 2.1 represents the general form of the polarization equation, accounting for higher-order terms:

$$P(t) = \chi^{(1)}E(t) + \chi^{(2)}E(t)E(t) + \chi^{(3)}E(t)E(t)E(t) \tag{2.1}$$

Each term in the equation corresponds to the generation of harmonics at multiples of the fundamental frequency. Higher-order terms, such as $\chi^{(2)}$ and $\chi^{(3)}$, contribute to the generation of second and third harmonics, respectively. However, the magnitude of the higher-order susceptibility decreases with increasing order, resulting in weaker higher-order frequency generation compared to the lower-order frequency generation. Therefore, intense light sources, such as femtosecond lasers, are necessary to observe harmonic generation.

Second harmonic generation (SHG) is attributed to three primary origins: electric field dipole (ED), electric field quadrupole (EQ), and magnetic dipole (MD) contributions. In non-centrosymmetric materials, the dominant contribution is from the ED, and the relationship between the polarization of the SHG signal and the susceptibility tensors can be mathematically described as follows:

$$P_i(2\omega) = \chi_{ijk}^{(2),ED} E(\omega)_j E(\omega)_k \tag{2.2}$$

Here, $P(2\omega)$ represents the induced second-order polarization at the SHG frequency 2ω, and $\chi^{(2)}$ is a third-rank tensor that characterizes the nonlinear optical properties of the material. The tensor possesses non-zero elements only for specific combinations of polarization states. In contrast, centrosymmetric materials exhibit a vanishing tensor $\chi^{(2),ED}$, resulting in the absence of SHG. However, the presence of surfaces or interfaces breaks the inversion symmetry, making SHG a sensitive probe for studying such structures. Furthermore, contributions from electric field quadrupole and magnetic dipole effects may also be observed, leading to a more complex form of the susceptibility tensor and its relation to the induced second-order polarization or magnetization and the oscillating electric and/or magnetic fields.

The MD contribution can arise from various sources, including the polarization induced by a combination of the electric field $E^{(\omega)}$ and the magnetic field $H^{(\omega)}$ (PEH), the oscillating magnetization $M^{(2\omega)}$ induced by a combination of two electric fields $E^{(\omega)}$ (MEE), and the magnetization induced by an electric field and magnetic field (MEH), among others (Shan, 2022). These processes are allowed in centrosymmetric media due to the axial nature of H and M. Regarding EQ, the oscillating quadrupole can be expressed as:

$$P_i(2\omega) = \chi^{(2),EQ}_{ijkl} E_j(\omega) \nabla_k E_l(\omega) + \chi^{(2),EQ}_{ijkl} E_j(\omega) \nabla_l E_k(\omega) \tag{2.3}$$

With an increasing number of independent elements in the susceptibility tensors, SHG is capable of differentiating between different point groups, providing valuable information about the symmetries, whether they are structural, electronic, orbital, or magnetic, of the systems under study.

In experimental setups, by appropriately controlling the polarization states of the incident and detected light, specific components of the susceptibility tensor can be determined. One commonly employed technique is rotational anisotropy SHG experiments, where the single crystal sample is rotated along the sample surface normal, and SHG is measured as a function of the sample rotation angle. However, this method faces difficulties, especially in cryogenic measurements where rotating the sample becomes impractical within the cryostat. Additionally, rotating the sample can lead to beam-walking, resulting in a change in the measured spot, which is especially problematic when dealing with non-uniform samples, such as those with domain distributions. Alternatively, the same effect can be achieved by rotating the scattering plane consisting of the incident light and SHG reflectivity. There are two typical approaches to accomplish this. One approach is to measure the polarization dependence angle by angle, employing a photomultiplier tube to detect the signal and a lock-in amplifier to reduce noise. This technique is generally applied when measuring normal incidence SHG and will be discussed in the experimental setup section in detail. Alternatively, in an oblique setting, a high-speed measurement method using a CCD is proposed. The key aspect of this setup is to spatially separate the signal corresponding to different polarizations and use a CCD to detect the signal. By rotating the entire system at a frequency of several hertz, this setup achieves not only high-speed measurements but also effectively reduces lower-frequency noise induced by laser power fluctuations or beam-pointing drift. Further details about high-speed measurement SHG rotational anisotropy using a CCD can be found in the work by Harter et al. (Harter, Niu, et al., 2015).

Incorporating a high-pressure environment into SHG experiments necessitates meticulous attention to various factors, including the choice of diamond and the DAC itself, to ensure accurate and reliable measurements.

The selection of the diamond type holds significant importance in achieving precise and reproducible SHG results. Type Ia diamonds commonly used in pressure studies

exhibit substantial changes in the patterns of reflected and transmitted SHG signals. These changes can be attributed to the presence of defects and impurities within the diamond crystal that gives large backgrounds. Moreover, they can also introduce complications such as local strain, which affects light polarization and distorts the SHG response. Therefore, utmost attention must be given to the quality and characterization of the diamond to minimize undesired effects on the experimental outcomes. Type IIa diamonds, characterized by high purity and low nitrogen impurity levels, exhibit remarkable stability in maintaining the symmetry of the reflected and transmitted SHG patterns. As shown in 2.5, the SHG pattern remains consistent and predictable for type IIa diamonds, making them advantageous in experimental setups and facilitating reliable interpretation of SHG signals.

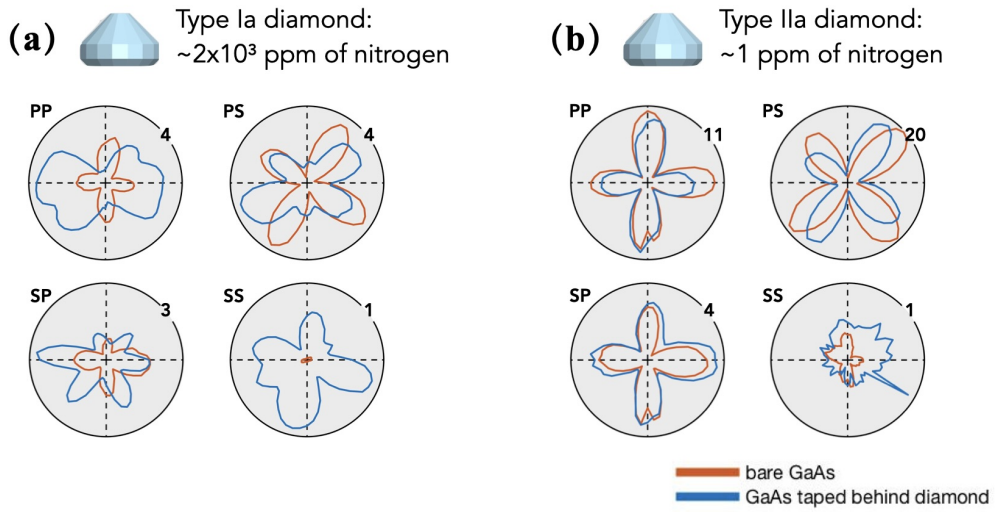

Figure 2.5: Comparison of SHG signals from a GaAs sample in a DAC using type Ia (a) and type IIa (b) diamonds.

Furthermore, when subjecting a diamond to high pressure within a DAC, additional factors come into play that can influence SHG measurements. Notably, the development of birefringence in the pressurized diamond affects the polarization properties of the SHG signal. Birefringence arises due to the anisotropic compression of the diamond lattice under pressure, leading to different refractive indices along distinct crystallographic directions. Consequently, the polarization of the SHG signal can become distorted, resulting in changes in the symmetry and intensity of the observed SHG patterns. Therefore, accounting for the birefringence effect and carefully analyzing the polarization properties of the generated harmonic signal become crucial when conducting SHG experiments under high-pressure conditions. A practical ap-

proach to mitigate this complication is to perform normal incidence measurements, where the incident and generated SH waves propagate along the same direction. In such settings, the quasi-uniaxial pressure applied to the diamond along its normal axis is particularly suitable for such measurements.

In addition to the diamond-specific effects, the diamond anvil cell (DAC) itself can introduce further complexities that need to be considered in high-pressure SHG measurements. One such complexity arises from the use of pressure-transmitting media within the DAC, which typically have different refractive indices compared to the sample and diamond. This refractive index mismatch occurs at the interface between the sample and the media and can lead to light scattering, absorption, and attenuation of the SHG signal, ultimately resulting in alterations in its polarization characteristics. Moreover, the size of the DAC necessitates the use of an objective with a specific working distance, which can impose limitations on the spatial resolution of the SHG measurements.

In summary, conducting SHG experiments in high-pressure environments requires meticulous management of the nonlinear optical properties of diamonds, careful consideration of birefringence effects induced by pressurized diamonds, and an understanding of the additional complexities introduced by the DAC. By addressing these factors, we can enhance the reliability and accuracy of SHG measurement in high-pressure settings

Experimental Setup

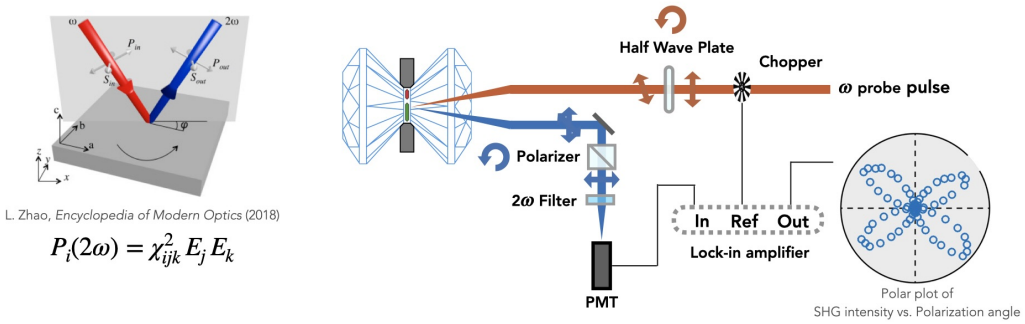

Figure 2.6: Illustration of the SHG-RA experimental configuration employed for the measurement of samples located within a DAC.

2.7 depicts a photograph of the experimental setup employed for measuring SHG response from the sample in normal incidence geometry. The whole system supports

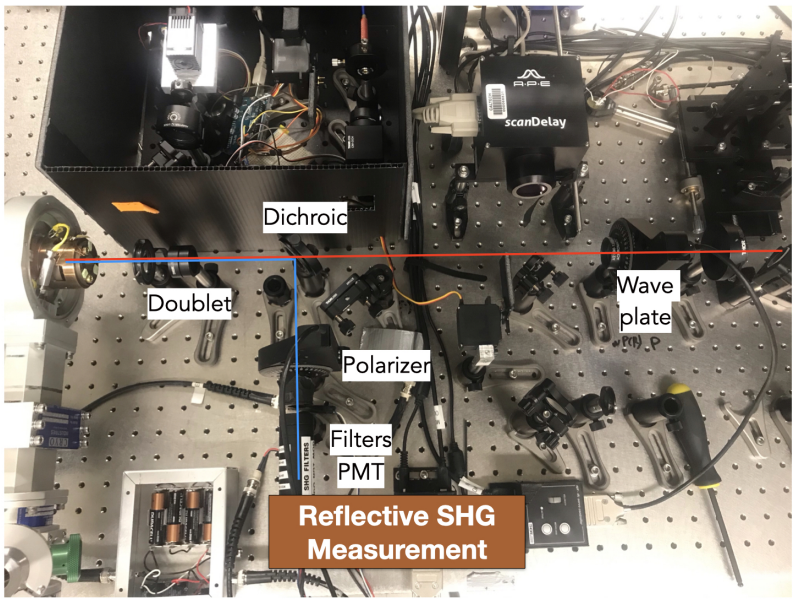

Figure 2.7: Photograph capturing the experimental setup of the SHG-RA technique utilized for the measurement of samples confined within a DAC.

a total of three optical measurements. Besides the reflective or transmissive normal incidence SHG (NI-SHG) measurement, with the help of a flippable mirror, we can switch to the ruby fluorescence measurement for pressure determination, or to the reflective and transmissive optical imaging to assist alignment and to monitor gasket shape.

In the normal incidence setting, the two distinct geometries are the parallel (denoted as P) and the perpendicular (denoted as S) one, depending on the relative polarization of the incoming fundamental and the outgoing second harmonic beam. To acquire the specular reflected SHG signal intensity as a function of the rotation azimuth angle φ, we use a half-wave plate (HWP) to adjust the incoming beam polarization and use a polarizer analyzer to selectively detect a certain polarization component of SHG response. By rotating HWP and the polarizer simultaneously, we acquire an effect equivalent to a rotating sample along the optical axis, while the former achieves better stability due to a fixed beam path. For a perfect normal incidence, we use the same objective or lens to collimate the incoming beam and collect the outgoing beam. They share the same optical path that goes through the optical axis of the lens and is split by a 45-degree long pass dichroic mirror (DM). To get rid of the undesired wavelength, in addition to the DM, a set of color filters is placed in front of the signal receiver: the photomultiplier tube (PMT). Different than the oblique incidence situation where the angle-dependent signal is spatially separated

and can be detected by CCD, in the NI setting, we employ a photomultiplier (PMT) to measure the signal in an angle-by-angle fashion, which is slower. However, the incorporation of the lock-in amplifier system greatly lowers the noise-to-signal ratio and is more sensitive to weak signals. Moreover, with a 50X objective, we can obtain a spatial resolution down to 1 μm, which is particularly essential in 2D material study where the field of uniform structure is usually limited.

Through a global fitting with a single susceptibility tensor to both the P and S channels, we can derive the point group or rule out the impossible ones, hence determining the underlying symmetry of the phases.

Time-resolved Reflectivity under High-Pressure

Time-resolved reflectivity techniques are powerful tools for investigating the dynamic behavior of materials on ultrafast timescales. One commonly used method is the pump-probe technique, which involves illuminating a sample with an intense laser pulse (pump) to induce an impulsive perturbation, followed by probing the sample with a time-delayed weaker pulse (probe) to measure the resulting changes in reflectivity. By varying the time delay between the pump and probe pulses, the temporal evolution of the reflectivity can be captured, providing valuable insights into the underlying processes and properties of the material.

In particular, time-resolved reflectivity can shed light on the electronic structure of materials. When a femtosecond laser pulse interacts with a sample, it can excite or perturb the electronic states, leading to changes in reflectivity. The time-resolved reflectivity signal contains information about the ultrafast dynamics of these excited states, such as relaxation, recombination, and carrier transport processes, as well as the properties that govern the behavior of materials under dynamic conditions. By analyzing the temporal evolution of the reflectivity signal, key parameters related to the electronic structure, such as the electron-phonon coupling strength, carrier lifetime, and bandgap renormalization, can be extracted. Overall, time-resolved reflectivity offers a non-destructive and sensitive approach to investigating the ultrafast dynamics and electronic structure of materials.

To measure the dynamic process of the excited system, we pump the material into a non-equilibrium state and probe the decay after a controlled time delay. While the probing method can be versatile (e.g. fundamental or SHG reflectivity), we focus on the experimental setup for time-resolved reflectivity (R) which measures the fractional change of the reflectivity ($\Delta R/R$) as a function of time delay.

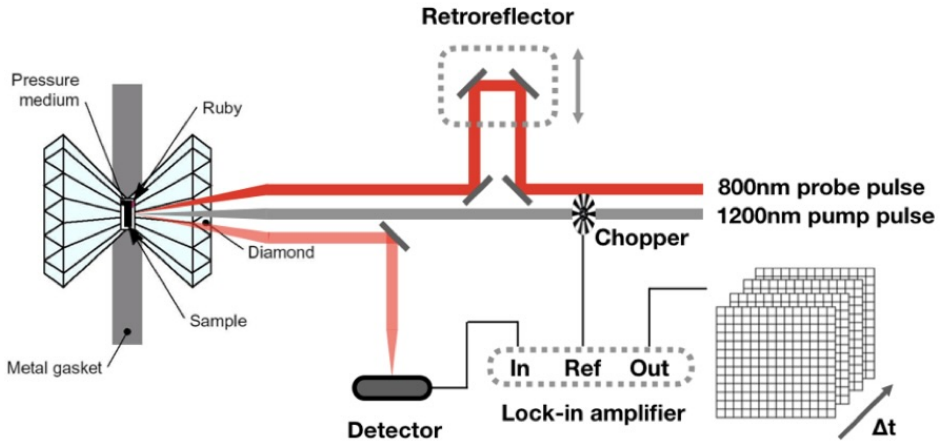

Figure 2.8: Illustration of the time-resolved reflectivity experimental configuration employed for the measurement of samples located within a DAC.

The schematic diagram shown in 2.8 demonstrates the pump-probe optical setup with the pump and probe light paths depicted as different colors. In the pump arm, we use a telescope composed of a pair of lenses to adjust the beam width. Decreasing the beam width creates an enlarged beam spot at focus. With a combination of a half-wave plate (HWP) or polarizer and a following polarizer, we can tune the beam power without changing the polarization. In a polarization-dependent measurement, an additional HWP should be placed following the polarizer. The same set of optics can be used in the probe path for changing beam width and power. We generally require the pump beam spot to be 2 to 3 times larger than the probe spot, and the fluence to be an order of magnitude larger. Time delay is controlled by a harmonically shaking retroreflector, whose movement changes the optical path length and hence the time of arrival of the beam. Finally, a semiconductor sensor is used to measure the reflected beam intensity.

In a lot of cases, the reflectivity transient exhibits quasi-exponential or multi-exponential-like behavior. By fitting, we can extract the characteristic time constants and decide the separate evaluation for different relaxation channels.

2.3 Magneto-Optic Kerr Effect Microscopy

Magneto-Optic Effects

The magneto-optical effect is a fascinating phenomenon that occurs when light interacts with the magnetization of a material, resulting in changes in its optical

properties. There are several distinct types of magneto-optical effects, including the Faraday effect, Kerr effect, Voigt effect, and magneto-optic gradient effect.

The Kerr and Faraday effects are categorized as linear magneto-optical effects, where there is a linear relationship between the magnetic field and the induced polarization rotation or ellipticity of light. The Faraday effect is observed in transmissive samples, while the Kerr effect describes changes in the polarization of reflected light. These effects, arising from the birefringence for left- and right-circularly polarized light, result in changes in the polarization and/or ellipticity of incident light, which are directly proportional to the magnetization of the material. Additionally, the Voigt effect exhibits quadratic dependence on magnetization, while the magneto-optic gradient effect manifests when there is a spatial gradient in the magnetization of a material, making it particularly useful for studying domain boundaries.

These linear and quadratic magneto-optical effects have wide-ranging practical applications. In the field of magneto-optic devices and components, they are utilized in modulators, isolators, switches, and sensors. Magneto-optic sensing and imaging techniques leverage these effects to measure and visualize magnetizations with high sensitivity and spatial resolution. In our study, we focus on microscopy based on the Kerr effect. One of the reasons for this choice is that the Kerr effect is the most versatile and flexible among all observation methods. By employing image processing techniques, domain contrast can be observed on virtually all ferro- and ferrimagnetic samples.

Geometries of MOKE Measurement

In MOKE measurement, three primary geometries can be discerned, namely polar, longitudinal, and transversal. These geometries are distinguished based on the relative orientation of the magnetization vector M, the reflection surface, and the plane of incidence. The utilization of these distinct configurations facilitates the acquisition of three distinct magnetization components. Specifically, the polar geometry offers sensitivity to the out-of-plane component Mp, whereas the longitudinal and transversal geometries exhibit sensitivity to the in-plane components Ml and Mt, respectively. The proper selection of the aforementioned geometries enables the determination of each magnetization component with precision.

Magneto-Optic Kerr Effect Microscopy

In magnetic materials, domains and domain walls (DW) play a vital role in determining the material's magnetic properties and behavior, and they are also the main focus of a lot of studies. Moreover, small-scale features such as vortices and defect can have a significant impact on bulk measurement as well. When studying magnetic thin films or layered structures, the behavior of individual layers, interfaces, and magnetic interactions between them should be distinguished. To visualize the intricate details of a material's magnetic structure at the micro- and nanoscale, we can apply MOKE microscopy. High spatial resolution in Kerr microscopy enables the detailed characterization and investigation of these features. For example, it allows researchers to study domain wall motion, nucleation processes, and magnetic phase transitions at the nanoscale. Such investigations provide valuable insights into the fundamental magnetic properties of the material and can inform the development of advanced magnetic devices and technologies.

Furthermore, spatial resolution in Kerr microscopy allows for quantitative analysis of magnetic properties. By accurately measuring the sizes and shapes of magnetic domains, researchers can determine important parameters such as domain wall widths, magnetization distribution, and magnetic anisotropy profiles. This quantitative information aids in the characterization and understanding of magnetic materials, leading to improved models and theories that describe their magnetic behavior.

Wide-field and Scanning Kerr Microscopy

Wide-field and scanning Kerr microscopies are two commonly used techniques in the field of magneto-optics for studying magnetic properties and domain structures in materials. The wide-field microscopy, also known as the parallel technique, immediately provides an image of a certain sample area. In the scanning method, a laser spot is scanned relative to the sample surface building up the image sequentially. Each technique has its own advantages and disadvantages, which make them suitable for different experimental scenarios.

Wide-field microscopy offers several advantages that make it a popular choice for magnetic imaging. One key advantage is its fast imaging speed. With wide-field microscopy, it is possible to acquire images of large areas or even the entire sample simultaneously, allowing for rapid characterization of magnetic domains or dynamic processes. This is particularly advantageous when studying materials with

fast magnetic dynamics or when a high throughput of samples is required.

Another advantage of wide-field microscopy is its simplicity and ease of operation. Wide-field setups typically consist of standard optical components, such as objectives, filters, and detectors, making them relatively straightforward to set up and use. On the other hand, scanning the beam spot relative to the specimen can be achieved through a sample-scanning fashion or a beam-scanning fashion, while the former is better at maintaining the angle of incidence and the polarization state of the incident and reflected rays. However, this technique often involves the use of a motorized positioning system with high precision, which is not only expensive but also hard to incorporate into the cooling system.

In wide-field magnetic force microscopy (MFM), the spatial resolution is limited by the Rayleigh criterion. Due to the diffraction of light, the smallest separation between two resolvable point objects should be larger than $D_{min} = 0.5\ \lambda/\mathrm{NA}$, where λ is the light wavelength and NA is the objective or lenses used for the sample. For example, with a green light with a wavelength of 550 nm and an oil-emerged objective with NA of 1.4, we can reach a theoretical resolution of 300 nm. Compared with the wide-field MFM, the laser scanning method can in general achieve superior spatial resolution, which is determined by the beam spot size, depending on λ, the objective's focal length, and the width of the incoming beam as well. For both ways, to increase the resolution for detailed imaging of the small magnetic structure, digital analysis can be helpful.

Through the implementation of lock-in detection and a modulated laser beam, laser scanning microscopy significantly improves the signal-to-noise ratio by selectively amplifying the signal at the modulation frequency and rejecting noise at other frequencies. This is particularly beneficial when studying small polarization rotation or ellipticity or weak signals in the presence of significant background noise. Moreover, the application of lock-in also allows the detection of ac magnetization dynamics modulated by the high-frequency field. Through the point-to-point scanning fashion, this method retains most of the advantages possessed by the point magneto-optical (MO) measurement, hence its versatility. For example, it can utilize interferometry-based MOP detection, and can simultaneously obtain signals for in- and out-of-plane magnetization components. These are valuable advantages possessed by the scanning method.

Experimental Setup

A typical wide-field Kerr microscope setup is shown in 2.9, which is composed of two main parts: the illuminating system, which is illustrated as the yellow-ray diagram, and the polarization microscope. To observe the detailed magnetic structure, a wide-field Kerr microscope can be applied, where the distinct MO responses from different sample positions are converted into the intensity contrast of the MO image. However, not only the MO-induced Kerr rotation or ellipticity but also the light intensity that illuminated the specimen area determined the intensity of the corresponding pixel. Therefore, a homogeneous illumination field of view plays a vital role in obtaining a constant MO contrast across the viewing field, which is essential for direct observation and the following digital processing and analysis. To achieve this goal, Kohler illumination is applied.

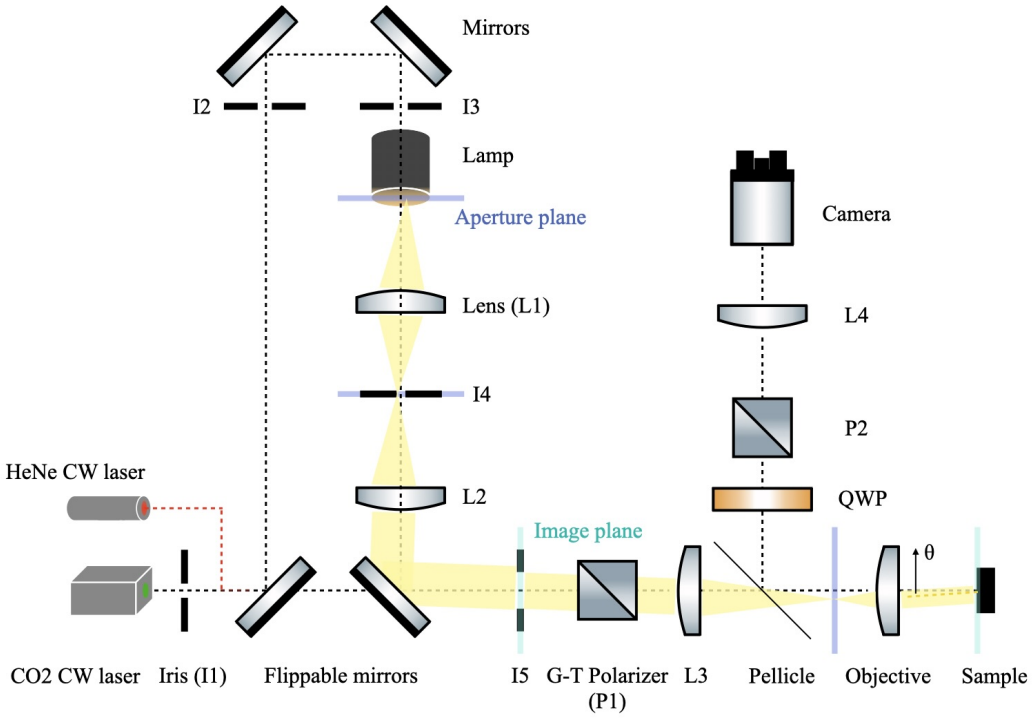

Figure 2.9: Schematic of the MOKE microscope experimental setup.

Light emitted from the lamp is focused by a lens (L1) onto the plane of the aperture diaphragm. An adjustable iris (I1) performs as an aperture. By changing the position of the iris, we change the incident angle of the bundle rays onto the sample, and different Kerr measurement configurations can be achieved. A centered iris scheme leads to a polar Kerr configuration, where, due to the symmetry, lights of oblique angles cancel each other out. On the other hand, when we move the iris center

off the optical axis of the beam path, we can achieve longitudinal or transverse configurations with different incidence angles and polarization combinations. By adjusting the iris opening, we can tune the largest azimuth angle of the light cone onto the sample, and thus the intensity and the depth of field. In principle, a point light source is ideal for a sufficient defocus of light; therefore we aim to close the iris as much as possible. However, with the limited power of the light source, a decreased intensity is detrimental to the high contrast. It is a trade-off. Following the iris, a second lens (L2) focuses the light rays into infinity, and the beam width is controlled by another iris (I2). Ideally, this iris is placed in a conjugate plane of the sample surface, and therefore the aperture will be imaged onto the sample. Hence, it is called the image diaphragm. By tuning the opening, we adjust the illuminated area without changing illumination intensity or spatial resolution. After the beam passes through the linear polarizer (P1), the third lens focuses it onto the back focal plane of the objective for the sample, which eventually defocuses the light rays and uniformly illuminates the field of view. In practice, the realization of Kohler illumination relies on the proper alignment of two sets of conjugate planes. The aperture planes include a lamp, AP, and the back focal plane of the sample objective. The image planes are the image diaphragm and the sample surface.

In the image formation process, the light that is reflected from the specimen is captured using the same objective that was utilized to illuminate the sample. A pellicle beamsplitter is placed between the last lens and the objective in order to direct the reflection beam toward the analyzing arm. The analyzing arm comprises a quarter wave plate (QWP) and a polarizing analyzer (P2). The QWP plays a crucial role in converting any helicity difference that arises from variations in the magnetization state into a difference in linear polarization. The P2 then takes this difference and further converts it into image contrast that is linearly dependent on the magnetization magnitude.

Alternative to the confocal MO imaging setup described above, where the incident and reflected light share the same objective lens, the illumination and observation paths can be totally separated with a large incidence angle. This scheme has the advantage of measuring the in-plane magnetization, where the longitudinal or transverse configuration should be applied, and the MO signal is proportional to the in-plane component of the detection light. However, there are several severe drawbacks due to the inclination of the imaging scheme, which includes a strip-like focused area, induced by a tilted objective focal plane, and a distortion of the image

as a result of inhomogeneous magnification. Through precise adjustment of the optics and digital processing, these problems can be alleviated.

Data Processing and Data Analysis

The data processing of Kerr images involves several steps to extract meaningful information from the acquired images. Firstly, the raw Kerr images, which capture the magnetization-induced optical contrast, are typically captured using a sensitive camera or detector. These images are then subjected to contrast enhancement and background correction to eliminate any non-magnetic signal contributions, such as uneven illumination or noise, which become especially obvious at near-crossed polarization. Since the Kerr-induced rotation or ellipticity is weak, the background severely obscures the magnetic features. The noise can be lowered by averaging multiple images or extending exposure or integrating time. To enhance the contrast, it's suggested to obtain a different image by subtracting averaged domain-free images from the raw Kerr image with magnetic features. The former can be acquired in a field-induced saturated state or in a paramagnetic state at a high temperature. However, in our measurement, we aim to track the evolution of domain structure. The application of saturating magnetic field should be avoided. On the other hand, the thermal drifting of the cryostat, though small, not only changes the field of view but also varies the illumination distribution, making direct subtraction hard. Alternatively, we make the subtraction between images corresponding to different polarization states of the analyzing polarizer. When the magnetization is along the sample surface normal, the two domain components with opposite M directions lead to an opposite Kerr rotation relative to the cross-polarization, where the two domains are indistinguishable in an ideal situation. The clockwise and anti-clockwise deviation from a cross-polarization will symmetrically favor one of the domains. Meanwhile, in principle, the average of these two images shows a pure illumination distribution without magnetic domains showing up. By making subtraction between the two anti-symmetric images and dividing subtraction by the average, we enhanced the visibility of the magnetic features and partially correct the non-uniform illumination. 5.2 (a) and 5.2 (b) show direct output images by CMOS when the deviation angle is 7.5 degrees, and 5.2 (c) shows the difference image made from (a) and its counterpart (b).

Chapter 3

HIGH-PRESSURE CONTROL OF OPTICAL NONLINEARITY IN THE POLAR WEYL SEMIMETAL TAAS

The transition metal monopnictide family of Weyl semimetals recently has been shown to exhibit anomalously strong second-order optical nonlinearity, which is theoretically attributed to a highly asymmetric polarization distribution induced by their polar structure. We experimentally test this hypothesis by measuring optical second harmonic generation (SHG) from TaAs across a pressure-tuned polar to non-polar structural phase transition. Despite the high-pressure structure remaining non-centrosymmetric, the SHG yield is reduced by more than 60% by 20 GPa as compared to the ambient pressure value. By examining the pressure dependence of distinct groups of SHG susceptibility tensor elements, we find that the yield is primarily controlled by a single element that governs the response along the polar axis. Our results confirm a connection between the polar axis and the giant optical nonlinearity of Weyl semimetals and demonstrate pressure as a means to tune this effect *in situ*.

3.1 Introduction

The Weyl semimetal is a gapless three-dimensional phase of matter in which spin-polarized valence and conduction bands touch at isolated points —Weyl nodes —in the Brillouin zone (Armitage, Mele, and Vishwanath, 2018; Wan et al., 2011; S.-Y. Xu et al., 2015; Lv et al., 2015; L. X. Yang et al., 2015). Weyl nodes serve as sinks and sources of Berry curvature in momentum space and can thus only be removed by pairwise annihilation, rendering them topologically stable. The presence of Weyl nodes, which is only allowed in the absence of time-reversal or inversion symmetry, has been shown to endow materials with exotic DC transport properties including the chiral anomaly (Zyuzin and Burkov, 2012; C.-L. Zhang et al., 2016; Jia, S.-Y. Xu, and Hasan, 2016; Parameswaran et al., 2014; X. Huang et al., 2015), anomalous Hall (K.-Y. Yang, Y.-M. Lu, and Ran, 2011; Burkov, 2014; Sun et al., 2016) and surface Fermi arc mediated cyclotron motion (Moll et al., 2016; Koshino, 2016; Peng Li et al., 2017).

The transition metal monopnictide family of inversion broken Weyl semimetals has garnered additional attention for its band structure geometry induced second-order

nonlinear AC response (Orenstein et al., 2021). Headlined by TaAs, observations include strong light helicity-dependent injection (Q. Ma et al., 2017; Sirica et al., 2019; Gao et al., 2020) and helicity-independent shift photocurrents (Sirica et al., 2019; Osterhoudt et al., 2019; J. Ma et al., 2019), as well as a record-setting shift current-induced optical second harmonic generation (SHG) efficiency in the near-infrared spectral range (L. Wu et al., 2017; Patankar et al., 2018). This SHG response has been attributed theoretically to a large skewness in the polarization distribution originating from the polar structure of these materials (Patankar et al., 2018; Z. Li et al., 2018). Experimentally testing this hypothesis would not only advance our fundamental understanding of the nonlinear optical properties of inversion broken Weyl semimetals, but also illuminate new pathways to control them.

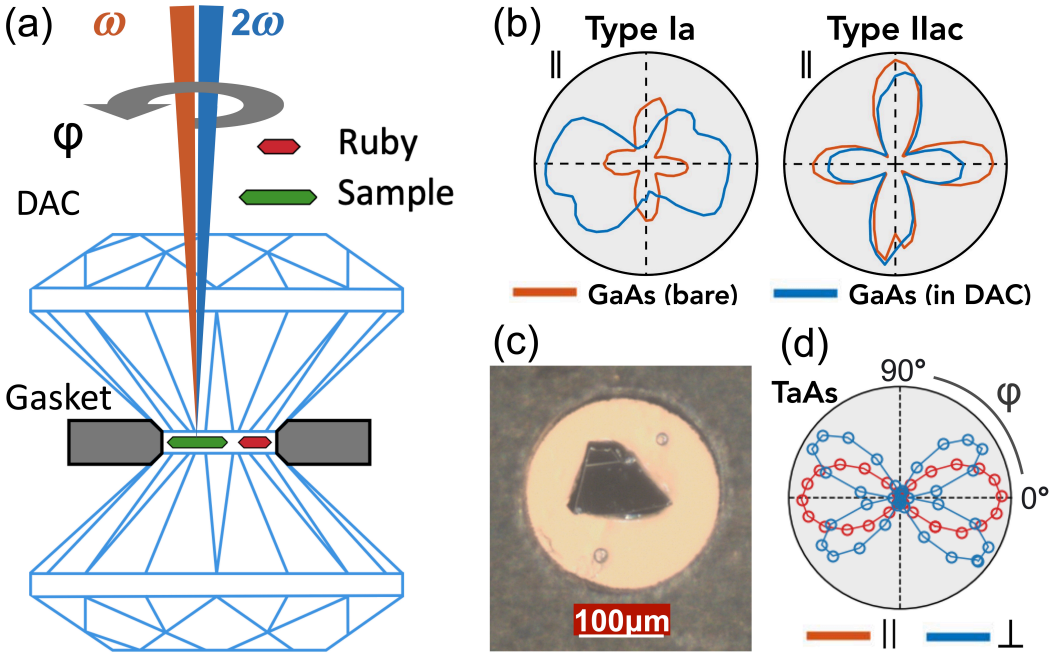

Figure 3.1: (a) Schematic of the diamond anvil cell (DAC) based SHG-RA setup. Incident and reflected SHG light are shown in red and blue, respectively. The angle between the polarization of the incident beam and the [1,1,-1] axis of TaAs is defined as φ. (b) Ambient pressure SHG-RA data from GaAs (001) obtained in a parallel polarization geometry through type Ia and type IIac diamonds (blue lines), compared to data taken on the bare sample outside the DAC (orange lines). The slight asymmetries in the SHG-RA patterns are due to GaAs surface imperfections. (c) Microscope image showing a TaAs (112) crystal sealed inside the DAC and the locations of ruby spheres for checking pressure homogeneity. (d) Ambient pressure SHG-RA data from bare TaAs (112) obtained in parallel and crossed polarization geometries.

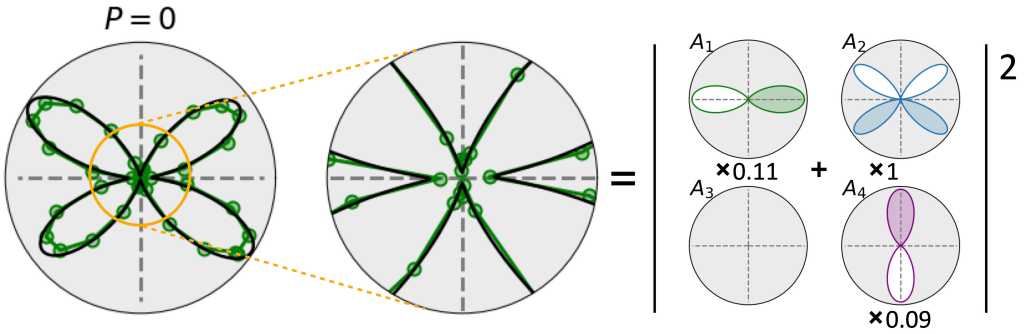

Figure 3.2: Typical cross-polarized SHG-RA pattern from TaAs (112) acquired at ambient pressure outside the DAC (left). A zoom-in (middle) shows a lifting of the nodes at 0° and 180°, indicating a finite A_1 term. Fits to the general form for $I_\perp(\varphi)$ are overlaid as black lines. A decomposition of the fits into its $A_1 \rightarrow A_4$ components is shown to the right. Filled versus empty lobes represent opposite signs of the associated trigonometric function. The fitted amplitude of the various terms is shown below, which are normalized to A_2 for $P < P_c$.

Powder x-ray diffraction measurements on TaAs (Yonghui Zhou, X. Chen, et al., 2016), supported by density functional theory calculations (ZhaoPeng Guo et al., 2018; Gupta et al., 2018; J. Zhang et al., 2017; M. Lu et al., 2016), have shown that hydrostatic pressurization above a critical value P_c = 14 GPa induces a phase transition from an inversion broken polar Weyl semimetal to an inversion broken non-polar Weyl semimetal. We present a pressure-dependent SHG rotational anisotropy (RA) study of single crystalline TaAs. We observe a structural symmetry change above P_c consistent with powder x-ray diffraction data, which is accompanied by a sharp decrease in overall SHG efficiency—approaching 60% at 20 GPa —despite the crystal symmetry remaining inversion broken. By tracking the pressure dependence of different components of the SHG susceptibility tensor, we show that this effect is dominated by the response along the polar axis, in line with a previous theoretical proposal. Moreover, we find evidence of reversibility upon slow decompression, providing a pathway to *in situ* tunable optical nonlinearity in Weyl semimetals.

3.2 Results and Discussion

Large hydrostatic pressures were applied using a 3-pin Merrill–Bassett diamond anvil cell (DAC) (Moggach et al., 2008). Continuous *in situ* pressure tuning was implemented using a helium gas-driven membrane and monitored via ruby fluorescence (3.1 (a)). Use of low defect density type IIac diamond (Almax easyLab) was essential for sufficiently reducing the SHG background to allow isolation of

reflected SHG light from the sample. A comparative study conducted on a GaAs test sample shows that its intrinsic SHG-RA pattern is hardly changed through a type IIa diamond, whereas it is completely obscured through a conventional type Ia diamond (3.1 (b)). Single crystals of TaAs were grown by vapor transport (Nair et al., 2020). As-grown (112) surfaces were identified for SHG measurements and polished from the backside to a thickness of 20 μm. Crystals were loaded inside a pre-indented MP35N gasket pressed between two diamonds with 600 μm culets (3.1 (c)). A mixture of methanol-ethanol (4:1) was used as the pressure medium. The sample was maintained at room temperature for all measurements. Light from a regeneratively amplified Ti:sapphire laser (1.5 eV photon energy, 100 kHz repetition rate) was focused at normal incidence onto a 30 μm spot (FWHM) on TaAs (112) with a fluence of 0.03 mJ/cm^2. Retro-reflected SHG light was reflected from a dichroic beamsplitter at a 45° angle of incidence onto a photomultiplier tube. The difference in reflectance for s- versus p-polarized light from the dichroic beamsplitter was less than 2 %, below our measurement noise level. Rotational anisotropy patterns were acquired by co-rotating a pair of input and output linear polarizers (D. Torchinsky et al., 2014; Harter, Niu, et al., 2015). Data collected in both parallel and crossed polarization geometries under ambient pressure agree closely with previously reported results (3.1 (d)).

Under ambient pressure, TaAs crystallizes in a body-centered tetragonal structure. Its $I4_1md$ space group (point group $4mm$) includes a polar axis along the z direction and two mirror planes (M_x, M_y) and two glide planes (M_{xy}, M_{-xy}) that contain the z axis. On the (112) surface, which is spanned by the [1,1,-1] and [1,-1,0] axes (3.3 (b)), the z axis and M_{xy} are projected onto [1,1,-1]. This results in SHG-RA patterns that are symmetric under reflection across the horizontally oriented [1,1,-1] axis (3.1 (d)). The high pressure phase is characterized by a non-polar hexagonal structure (space group $P\bar{6}m2$, point group $\bar{6}m2$) that breaks M_{xy} symmetry (Yonghui Zhou, X. Chen, et al., 2016). Therefore, the tetragonal-to-hexagonal phase transition can in principle be detected through the loss of horizontal reflection symmetry in the SHG-RA patterns (3.1 (d)).

For an ideal tetragonal crystal with point group $4mm$, the A_1 term in $I_\perp(\varphi)$ is forbidden by symmetry and the pattern should exhibit nodes at 0°, 90°, 180° and 270°. Yet we observe a small but finite A_1 component in our ambient pressure SHG-RA patterns taken outside the DAC (3.2), manifested as a lifting of the nodes at 0° and 180°. Our simulation results show that this is not due to misalignment,

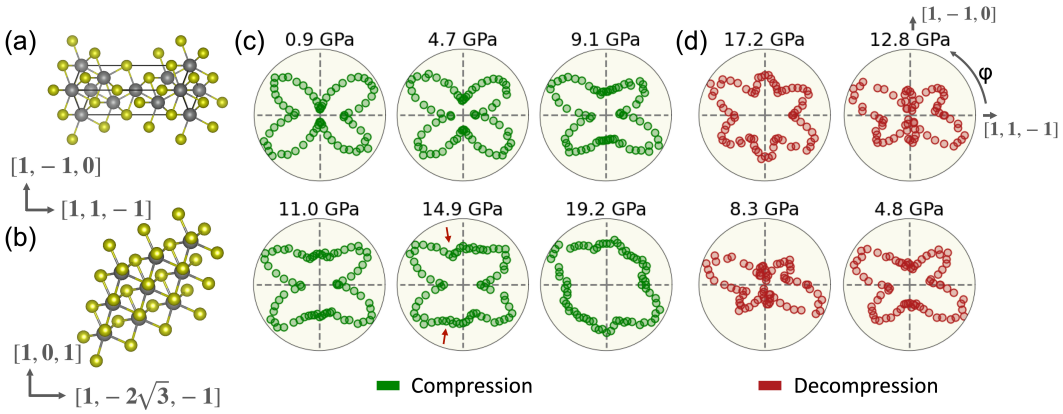

Figure 3.3: (a) Unit cell of ambient pressure tetragonal ($I4_1md$) TaAs projected onto the (112) surface. (b) Projection of high-pressure hexagonal TaAs ($P\bar{6}m2$) onto the same surface. (c) SHG-RA patterns at select pressures measured upon compression and (d) decompression after reaching a maximum pressure of 19.2 GPa. Pressure was tuned *in situ*, allowing all patterns to be acquired under identical alignment conditions. Horizontal and vertical dashed lines lie along the [1,1,-1] and [1,-1,0] axes respectively. The loss of horizontal mirror symmetry in the 14.9 GPa data can be seen from the presence of an intensity dip at $\varphi \approx 100°$ contrasted with hump at $\varphi \approx 260°$ (red arrows).

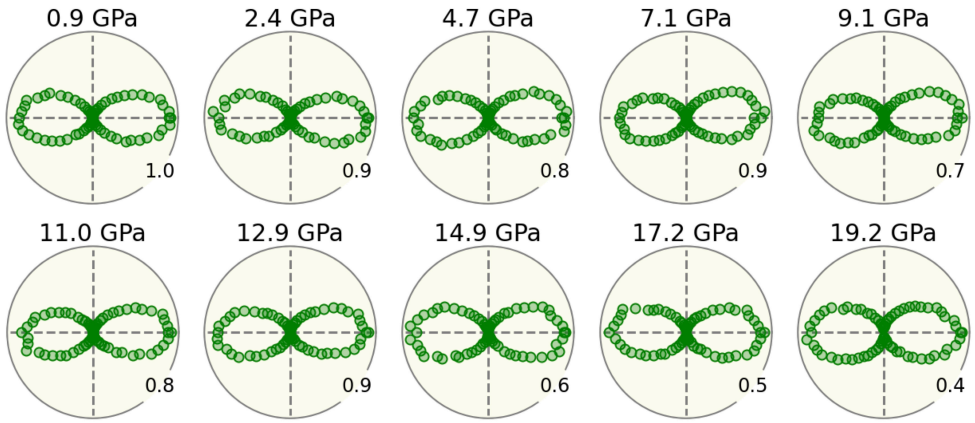

Figure 3.4: SHG-RA patterns at select pressure in parallel polarization geometry measured upon compression.

implying that the crystals may exhibit a slight departure from 4mm symmetry.

The most general form of the electric-dipole SHG-RA intensity in parallel polarized geometry under normal incidence is given by $I_{\parallel}(\varphi) \propto |B_1 \cos^3(\varphi) + B_2 \cos^2(\varphi) \sin(\varphi) + B_3 \cos(\varphi) \sin^2(\varphi) + B_4 \sin^3(\varphi)|^2$, similar to the case for crossed polarized geom-

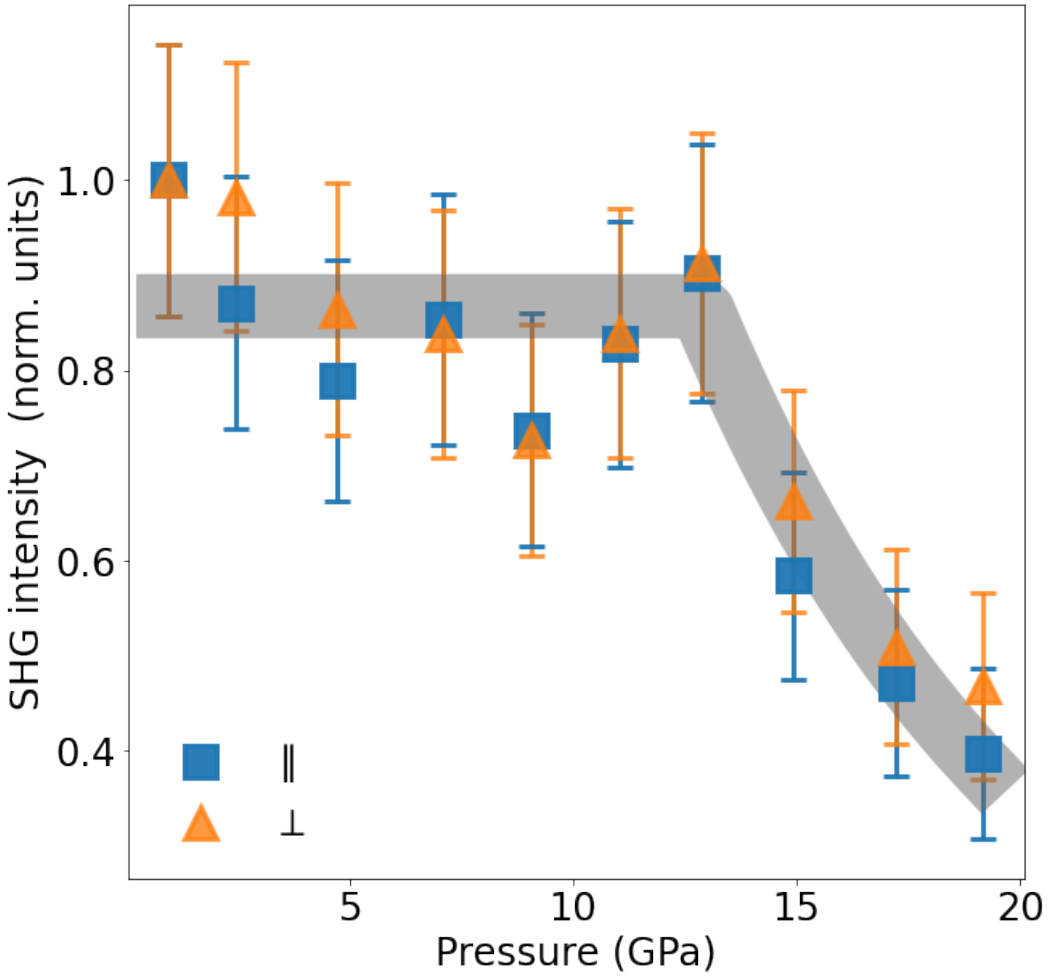

Figure 3.5: Pressure dependence of the φ-integrated SHG intensity from TaAs (112) measured upon compression for both parallel (blue squares) and crossed (orange triangles) polarization geometries. Each curve is normalized to its ambient pressure value. Error bars represent the intensity variation measured across different sample locations. Gray curve is a guide to the eye.

etry described in the main text. From the (112) face of TaAs in the tetragonal $4mm$ phase, $B_2 = B_4 = 0$ by symmetry, $B_1 = \gamma(2a^2\chi_{zxx} + 4a^2\chi_{xzx} + c^2\chi_{zzz})$ and $B_3 = \gamma(4a^2 + 2c^2)\chi_{xzx} + (2a^2 + c^2)\chi_{zxx}$, where $\gamma = 1/\left(\frac{2a^3}{c} + ac\sqrt{2 + \frac{c^2}{a^2}}\right)$ and a and c are the TaAs lattice constants.

3.3 (c) shows SHG-RA data on TaAs (112) in a crossed polarization geometry, acquired upon compression at an average rate of 1 GPa per hour. The intensities at different pressures are normalized to unity in order to better visualize the symmetry changes. At $P = 0.9$ GPa, the sealing pressure of the DAC, the pattern is nearly indistinguishable from ambient (3.1 (d)). Upon increasing pressure to 4.7

GPa, 9.1 GPa and 11 GPA, the intensity at 90° and 270° increases relative to the four major lobes, but the patterns continue to exhibit reflection symmetry about the horizontal axis. Therefore, these changes predominantly should arise from tetragonal symmetry-preserving lattice distortions. In contrast, at 14.9 GPa and 19.2 GPa the patterns become six-lobed and exhibit a clear loss of horizontal reflection symmetry, indicating a transition into the hexagonal structure. This is consistent with a previous high-pressure powder x-ray diffraction study (Yonghui Zhou, X. Chen, et al., 2016) that assigned P_c = 14.4 GPa and found phase coexistence over a finite pressure range around P_c, which cannot be ruled out in our SHG data. However, whereas the x-ray diffraction study showed that the hexagonal phase persists upon decompression below P_c, we find that the tetragonal SHG-RA pattern is restored upon decompression, although the intensity does not recover its ambient pressure value. This demonstrates that the transition is hysteretic but possibly reversible (3.3 (d)). This discrepancy may be due to a combination of our use of slow decompression over 8 hours, our lower peak pressure (19.2 GPa as opposed to 53 GPa) and differences in the behavior of single crystal versus powder samples.

3.2 shows SHG-RA patterns at various pressures measured in parallel polarization geometry. For all pressures, the patterns are dominated by the χ_{zzz} containing B_1 term, which was previously shown to be an order of magnitude larger than both χ_{zxx} and χ_{xzx} (L. Wu et al., 2017). Nonetheless, careful examination of the patterns shows that the nodes at 90° and 270° are lifted at high pressure, evidencing appearance of a B_4 contribution that is only allowed in the hexagonal phase.

A measure of the overall SHG conversion efficiency can be obtained by integrating the SHG-RA intensity over φ from 0 to 2π. 3.5 shows the pressure dependence of the φ-integrated intensity in both parallel and cross polarization channels. The intensity remains essentially constant at low pressures and then starts to decrease above approximately 13 GPa, dropping to nearly 40% of the ambient pressure value by 19.2 GPa. The fact that the intensity decrease occurs over a wide pressure window suggests a gradual transfer of population from the tetragonal to the hexagonal structure, consistent with powder x-ray diffraction measurements (Yonghui Zhou, X. Chen, et al., 2016). Upon scanning the laser spot across different regions of the crystal, we observe a slight variation in intensity, which is captured by the error bars in 3.5. However, the overall trend versus pressure is the same. These results indicate that the large second-order optical nonlinearity of the tetragonal phase should be primarily attributed to the presence of a polar axis rather than the absence of an

inversion center, which is retained in the hexagonal phase.

To directly evaluate the contribution of the polar axis to the SHG intensity, we investigate the pressure dependence of the individual electric-dipole SHG susceptibility elements χ_{ijk}, which govern the relationship between the incident electric field at frequency ω and the induced polarization at 2ω via $P_i^{2\omega} = \chi_{ijk} E_j^{\omega} E_k^{\omega}$. Under normal incidence and cross-polarized geometry, the most general form of the electric-dipole SHG-RA intensity is given by $I_{\perp}(\varphi) \propto |A_1 \cos^3(\varphi) + A_2 \cos^2(\varphi)\sin(\varphi) + A_3 \cos(\varphi)\sin^2(\varphi) + A_4 \sin^3(\varphi)|^2$ where $A_1 \rightarrow A_4$ are complex numbers representing different χ_{ijk} combinations. In the case where light is normally incident on the (112) face of TaAs in the tetragonal $4mm$ phase, $A_1 = A_3 = 0$ by symmetry, $A_2 = \gamma(2a^2\chi_{zxx} + c^2\chi_{zzz} - 2c^2\chi_{xzx})$ and $A_4 = \gamma(2a^2 + c^2)\chi_{zxx}$, where $\gamma = 1/\left(\frac{2a^3}{c} + ac\sqrt{2 + \frac{c^2}{a^2}}\right)$ and a and c are the TaAs lattice constants. Notably, the SHG response along the polar axis χ_{zzz} is contained in A_2, which was previously shown to be an order of magnitude larger than both χ_{zxx} and χ_{xzx} (L. Wu et al., 2017). In the hexagonal $\bar{6}m2$ phase, $A_1 \rightarrow A_4$ all become symmetry allowed.

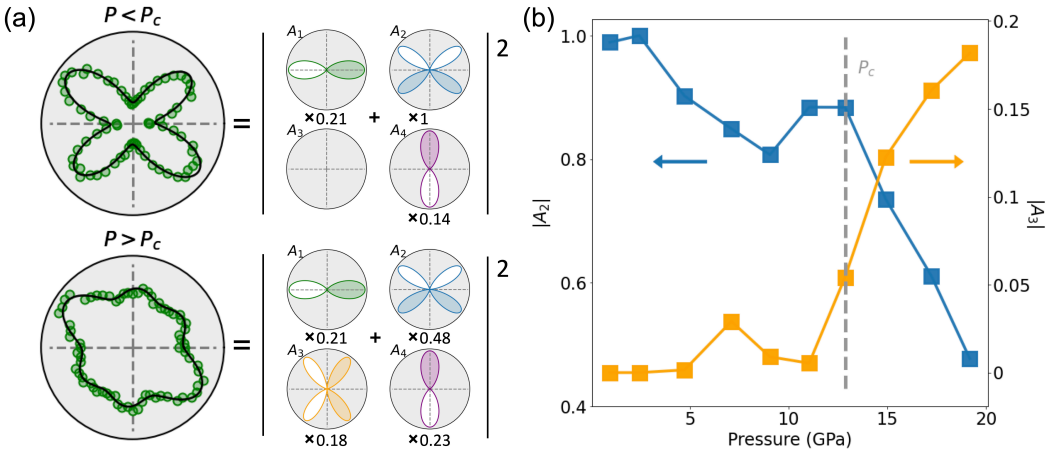

Figure 3.6: (a) Representative SHG-RA data acquired in crossed polarization geometry below and above P_c (green circles). Fits to the expression for $I_{\perp}(\varphi)$ given in the main text are overlaid as black lines. A decomposition of the fits into its $A_1 \rightarrow A_4$ components is shown to the right. Filled versus empty lobes represent opposite signs of the associated trigonometric function. The fitted amplitude of the various terms is shown below, which are normalized to the maximum value of A_2 for $P < P_c$. (b) Pressure dependence of the fitted amplitudes of A_2 (blue) and A_3 (orange).

The SHG-RA pattern at each measured pressure was fitted to the general expression for $I_{\perp}(\varphi)$. 3.6 (a) shows representative examples below and above P_c, which

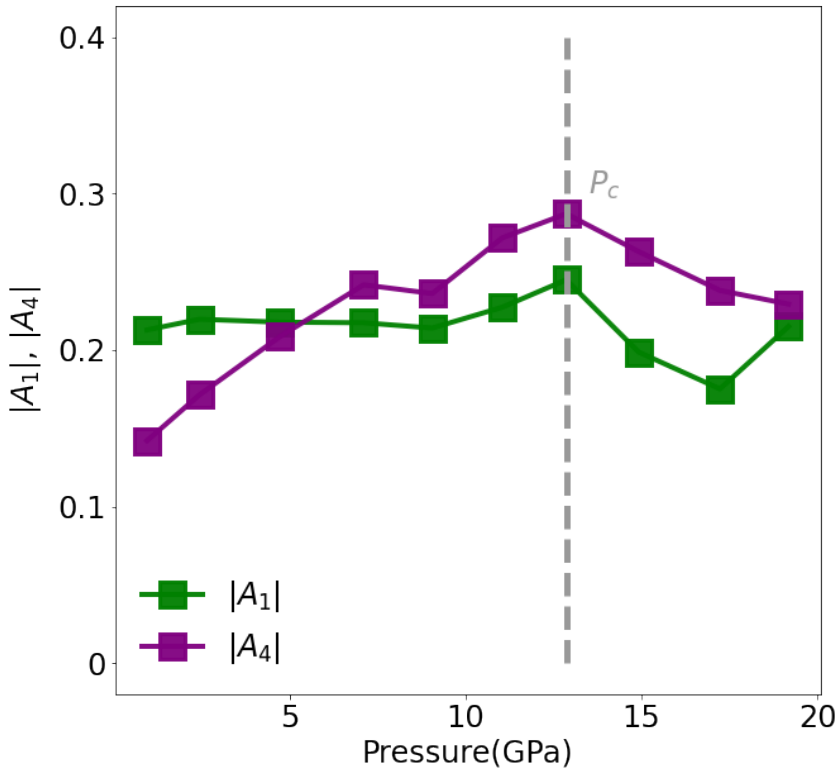

Figure 3.7: Pressure dependence of the fitted amplitudes of A_1 (green) and A_4 (purple) normalized to the maximum value of A_2 for $P < P_c$

demonstrates a high quality of fit, alongside the fitted amplitudes of $A_1 \rightarrow A_4$. As expected, for $P < P_c$ the fit is dominated by A_2 with an order of magnitude smaller contribution from A_4. We also note a small contribution from A_1 that is present even in data collected outside the DAC, possibly pointing to a slight departure of the ambient structure from $4mm$ symmetry. For $P > P_c$, all four terms become necessary in order to fit the SHG-RA patterns, with the growth of A_1 and A_3 being responsible for the loss of reflection symmetry about the horizontal axis. Moreover, the fit is no longer dominated by A_2, resulting in SHG-RA patterns with reduced anisotropy. The pressure dependence of $|A_2|$ and $|A_3|$ are plotted in 3.6 (b), which can be used to approximately track the order parameters associated with the polar tetragonal phase and non-polar hexagonal phase, respectively. We find that while neither $|A_2|$ nor $|A_3|$ exhibit strong pressure dependence below P_c, they undergo clear downward and upward trends respectively above P_c, with A_2 falling to less than 50 % of its ambient pressure value by 19.2 GPa. This reveals that the observed drop in overall SHG intensity above P_c (3.5) is predominantly due to a drastic reduction of χ_{zzz} induced by the loss of a polar axis in the hexagonal structure.

The SHG-RA patterns measured in crossed polarized geometry were fit to $I_{\perp}(\varphi) \propto |A_1 \cos^3(\varphi) + A_2 \cos^2(\varphi) \sin(\varphi) + A_3 \cos(\varphi) \sin^2(\varphi) + A_4 \sin^3(\varphi)|^2$. The fitted amplitudes of A_2 and A_3 are shown in the main text. 3.7 shows the pressure dependence of the fitted amplitudes of A_1 and A_4. Subtle kinks appear in $|A_1|$ and $|A_4|$ around the critical pressure P_c. However, as expected, $|A_4|$ does not change as drastically as $|A_2|$ because A_4 does not contain χ_{zzz}. Also, as expected, $|A_1|$ does not exhibit a clear kink at P_c as $|A_3|$ because A_1 is present in both the low and high-pressure phases.

These observations are qualitatively consistent with a recent theoretical proposal that relates χ_{zzz} to the third cumulant of the polarization distribution (C_3) (Patankar et al., 2018). In contrast to the first moment (C_1), which describes the average macroscopic polarization, C_3 characterizes the intrinsic asymmetry of the polarization distribution, independent of the electronic center-of-mass. Although C_3 is generally allowed whenever inversion symmetry is broken, a simplified two-band tight-binding model of TaAs showed that it is greatly enhanced by the polar structure. Therefore, the observed decrease in χ_{zzz} above P_c in our experiments can possibly be attributed to a drop in C_3 induced by the loss of a polar axis. Verification of this hypothesis will require detailed calculations of C_3 for realistic models of TaAs under pressure. By extension, our work opens a route to manipulate the large second-order nonlinearity of transition metal monopnictide Weyl semimetals by tuning their polar order parameter with hydrostatic pressure. More generally, our demonstration of high-pressure SHG-RA from single crystalline TaAs provides the means to search for symmetry breaking in the vicinity of high-pressure superconducting phases in non-centrosymmetric materials like TaP (Yufeng Li et al., 2017) or $Cd_2Re_2O_7$ (Harter, Zhao, et al., 2017; Malavi, Karmakar, and S. M. Sharma, 2016; Yamaura et al., 2017), which may be key to understanding their topological properties.

Chapter 4

PRESSURE-INDUCED PHASE TRANSITION IN SPIN-ORBIT-COUPLED MOTT INSULATOR Sr_2IrO_4

4.1 Introduction

Mott insulator with strong spin-orbit-coupling

In contrast to the 3D counterparts, where the underlying physics can be predominantly explained by the interplay between Coulomb interaction and kinetic energy within the Mott-Hubbard model, the 5d transition metal materials exhibit a distinctive behavior. In these materials, spin-orbit couplings (SOC) play a significant role in determining the states of matter. In addition to this, the enhanced crystal electric field (CEF) interaction and reduced Hund's coupling should also be considered in realistic cases. These parameters compete on similar energy scales, and their intricate coupling gives rise to a rich interplay of multiple degrees of freedom, leading to unique and captivating consequences.

The profound interplay described above finds a remarkable manifestation in the 5d transition metal oxide (5d-TMO) Sr_2IrO_4, where the influence of spin-orbit coupling (SOC) drives the emergence of a Mott insulating state. Despite the large spatial extension of the 5d orbitals, Sr_2IrO_4 exhibits an insulating ground state, a characteristic that can be attributed to the cooperative interplay of multiple factors. Firstly, the IrO_6 octahedral crystalline electric field (CEF) induces a splitting of the half-filled 5d band, resulting in the formation of an empty e_g band and a t_{2g} band containing five electrons. This t_{2g} band is further split into two energy levels: a lower fourfold degenerate level (J_{eff} = 3/2) and an upper twofold degenerate level (J_{eff} = 1/2) due to the influence of the spin-orbit interaction(0.2 ~ 1 eV). Finally, the combined effect of a moderate Coulomb interaction (0.5 ~ 2 eV) is sufficient to open a narrow charge gap (approximately 0.1 eV) within the half-filled J_{eff} = 1/2 level, leading to the emergence of an insulating magnetic ground state (B. J. Kim, Jin, et al., 2008).

Initially, the considerable enthusiasm surrounding Sr_2IrO_4 (214) stemmed from its resemblance to La_2CuO_4, the parent compound of the cuprate superconductors (SC), in terms of crystallographic, electronic, and magnetic structures. It was anticipated that chemically doped compounds of Sr_2IrO_4 would exhibit unconven-

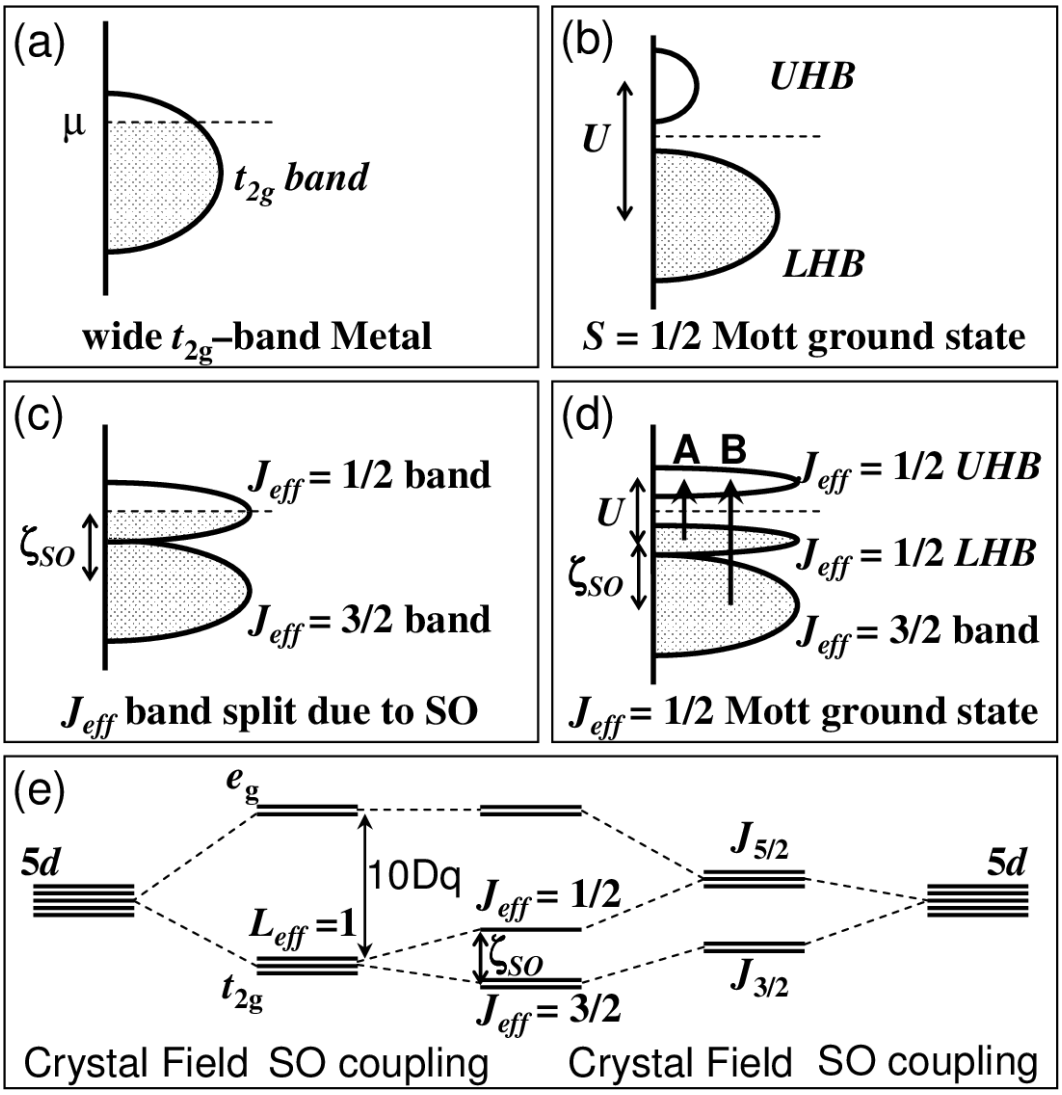

Figure 4.1: Schematic energy diagrams for the $5d^5$ (t_{2g}^5) configuration (a) without SO and Hubbard U, (b) with an unrealistically large U but no SO, (c) with SO but no U, and (d) with both SO and U . Possible optical transitions A and B are indicated by arrows. (e) 5d level splittings by the crystal field and SO coupling. The figure is adapted from (B. J. Kim, Jin, et al., 2008)

tional superconductivity. However, despite decades of dedicated research, the actual superconducting states have not been observed in Sr_2IrO_4.

Sr_2IrO_4 possesses a perovskite structure composed of layers of IrO_6 octahedra that share corners. These octahedra exhibit a uniform tetragonal distortion, characterized by elongation along the c-axis and a staggered rotation, leading to a two-sublattice structure. The IrO_6 cages undergo rotations around the c-axis, resulting in an angle of approximately $\phi = 12$ degrees. The magnetism in Sr_2IrO_4 arises from strongly

entangled spin-orbit (SO) moments with J_{eff} = 1/2, referred to as pseudospin hereafter. The moments within the layers order in a canted antiferromagnetic manner, as depicted in Figure 4.2b, and are confined to the ab plane under ambient pressure. The canting angle is approximately 12 degrees, which gives rise to a weak in-plane ferromagnetism and distinguishes the a and b axes. Considering the coupling between pseudospin and lattice, this magnetic ordering may induce a reduction in crystal symmetry from tetragonal to orthorhombic (Porras et al., 2019; H. Liu and Khaliullin, 2019). The inter-layer coupling is also AFM but can be easily aligned by applying a small magnetic field of 200 mT, resulting in a weak ferromagnetic order.

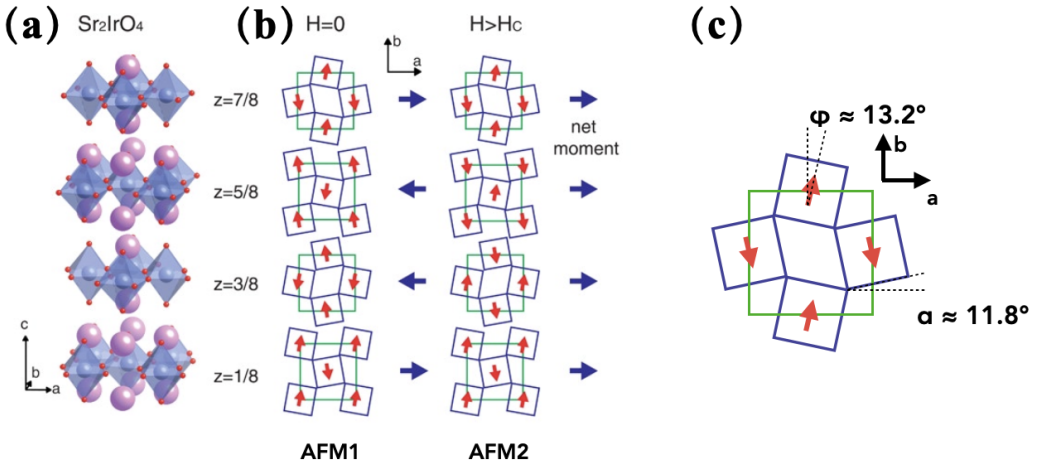

Figure 4.2: Magnetic ordering pattern of Sr_2IrO_4. (a) Layered crystal structure of Sr_2IrO_4, consisting of a tetragonal unit cell (space group *I41/acd*). The blue, red, and purple circles represent Ir, O, and Sr atoms, respectively. (b) Canted antiferromagnetic ordering pattern of J_{eff} = 1/2 moments (arrows) within IrO_2 planes and their stacking pattern along the c axis in zero field and in the weakly ferromagnetic state. The figure is adopted from (B. J. Kim, Ohsumi, et al., 2009). (c) the magnetic moment canting angle ϕ and oxygen octahedra rotation angle α.

However, recent studies have revealed slight deviations from this crystal structure. A combination of RA-SHG (Rotational Anisotropy Second Harmonic Generation) and RA-THG (Rotational Anisotropy Third Harmonic Generation) techniques (D. H. Torchinsky et al., 2015) provided valuable insights into the symmetry and distortions present in Sr_2IrO_4. The obtained results, with modulation in the magnitude of the RA pattern lobes, showed the best fitting with a 4/m point group, suggesting a departure from the previously assumed 4/mmm symmetry. The observed asymmetry was attributed to the inequivalent distortion in the two sublattices, which breaks the

mirror symmetry. With this picture, the observed perfect magnetoelastic locking can be explained.

Phase evolution under high pressure

Strong magneto-elastic coupling in Sr_2IrO_4 suggests the possibility of manipulating the magnetic structure via pressure-induced structural changes. Hydrostatic pressure offers a unique advantage as a tuning parameter since it directly acts on the crystallographic structure by adjusting interatomic distances and bond angles. This clean and controlled manipulation becomes particularly significant in systems where competing interactions of comparable strengths govern the behavior. Under such circumstances, applying pressure allows us to push the ground state away from its equilibrium state.

Given the expectation that, with compression, electron density increases and bandwidth broadens, one would typically anticipate a mixing of bands split by SOC and the onset of a metallic state. However, intriguingly, Sr_2IrO_4 exhibits an insulating behavior that persists even under extremely high pressures exceeding 185 GPa (C. Chen et al., 2020; Zocco et al., 2014; Haskel, Fabbris, Zhernenkov, et al., 2012). This unexpected insulating phase under pressure challenges the conventional understanding and prompts us to investigate further.

Delving into the magnetic properties of 214, we observe a series of magnetic phase transitions occurring at lower pressures, specifically below 20 GPa. Remarkably, a quantum paramagnetic phase emerges in 17 ~ 20 GPa, as evidenced by the continuum observed in the Raman scattering spectrum (X. Li et al., 2021) and the vanishing field-induced magnetization measured using x-ray magnetic circular dichroism (XMCD) (Haskel, Fabbris, J. H. Kim, et al., 2020; Haskel, Fabbris, Zhernenkov, et al., 2012). To gain deeper insights, Xiang Li et al. conducted meticulous studies on the pressure evolution of Raman active phonon and magnon modes, which revealed the presence of four successive magnetic phases in 214: an ambient magnetic phase below 3 GPa, coexistence of phases with different weak ferromagnetic (WFM) stackings from 3 GPa to 10 GPa, an antiferromagnetic (AFM) phase with spins flipped along the c-axis, and finally, a spin-disordered phase above ~ 20 GPa. It is noteworthy that the magnetic transition at 10 GPa, although not explicitly indicated by Haskel et al., is demonstrated by the significant suppression of x-ray resonant magnetic scattering intensity at ~ 9 GPa (see Fig.1 in (Haskel, Fabbris, J. H. Kim, et al., 2020)). Fig 4.3 (a), adapted from Haskel, Fabbris,

J. H. Kim, et al., 2020, illustrates the pressure-temperature (P-T) evolution of Ir magnetization in a powdered sample under a field of H = 0.5 T, as mapped out by XMCD. The line connecting the solid black circles depicts the potential trend of the magnetic ordering temperature with pressure, showing a decrease towards a quantum critical point.

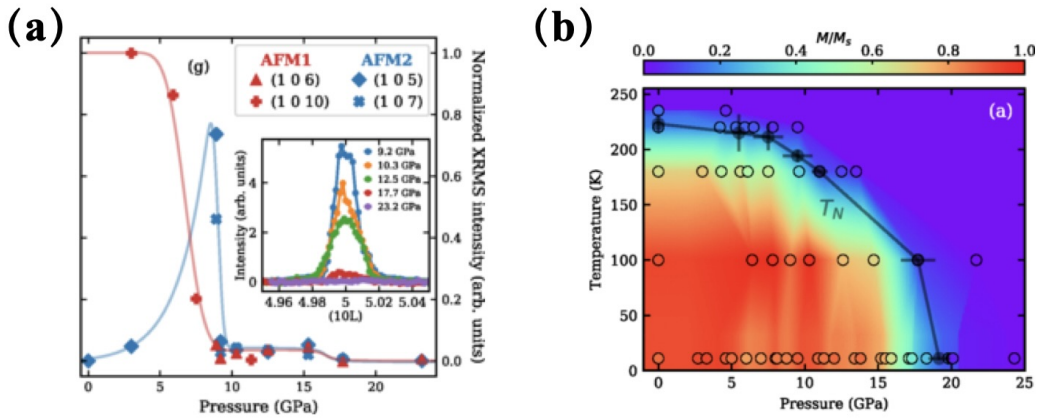

Figure 4.3: Pressure-induced quantum paramagnetic phase detected by X-ray resonant techniques. The figures are adopted from (Haskel, Fabbris, J. H. Kim, et al., 2020)

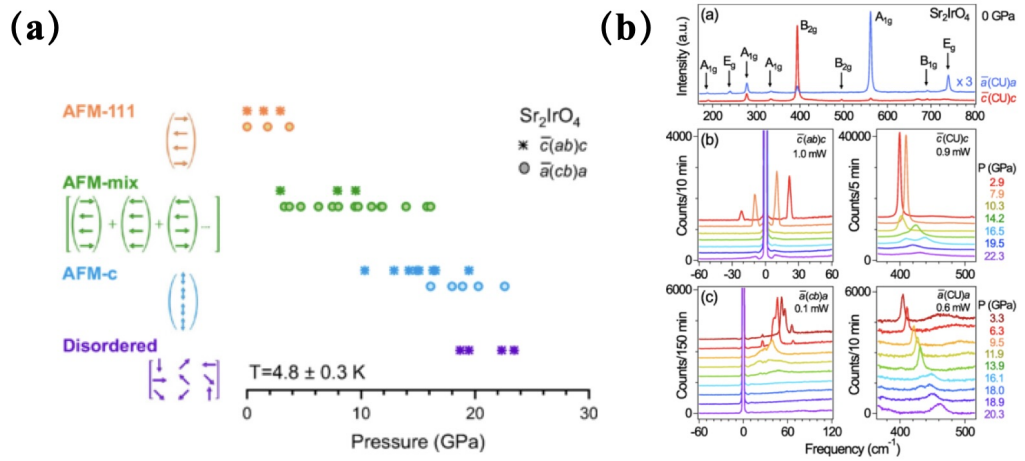

Figure 4.4: Raman studies of pressure-induced magnetic and structural transition under T = 5 K. (a) A summary of magnetic evolution, including schematics of four different spin arrangements under pressure. (b) Phonon Raman spectra in $\overline{c}$(CU)c and $\overline{a}$(CU)a configurations at ambient pressure and 4.8 K, with modes marked with arrows and the type. The figures are adopted from (X. Li et al., 2021)

Regarding crystallographic phase transitions, the Raman study reveals a quasi-

tetragonal-to-orthorhombic structural transition at 10 GPa under T = 5 K, coinciding with the magnetic spin-flip transition. A similar symmetry-lowering process is reported in room-temperature X-ray diffraction (XRD) studies conducted by Chen et al. and Samanta et al. (C. Chen et al., 2020; Samanta, Ardito, et al., 2018; Samanta, Tartaglia, et al., 2020). However, both studies suggest a critical pressure of approximately 40 GPa, as further supported by a minimum in resistivity connecting two monotonic trends in the pressure evolution (Chen 2020, Samanta 2018). Combining these pieces of information, we speculate that there may be an increasing critical pressure along with temperature, connecting the quasi-tetragonal and orthorhombic phases. It is possible that the downward magnetization line and the upward structural transition line intersect in the temperature-pressure (T-P) diagram, potentially leading to intriguing phenomena.

Keeping these questions and potential phenomena in mind, we apply a pump-probe technique to study the light-induced dynamics of Sr_2IrO_4 under high-pressure environments, aiming to shed light onto the behavior of electronic band gap.

4.2 Results and Discussion

Experimental details

We conducted a temperature-dependent time-resolved reflectivity measurement on the (001) cleaved face of a 214 single crystal while subjecting it to hydrostatic pressure conditions of up to approximately 14 GPa. To achieve this, we utilized a 3-pin Merrill-Bassett type diamond anvil cell (DAC) with a culet size of 600 μm. The gasket employed in the setup was constructed from MP35N foil of a thickness of 270 μm and pre-indented to approximately 100 μm. Furthermore, a hole with a diameter of a 250 μm was drilled through the center of the indentation. To apply pressure uniformly, we employed a 4:1 mixture of methanol and ethanol as the pressure medium. To accurately determine the pressure, we implemented an in-situ pressure control mechanism using a gas-driven membrane. The pressure values were determined in real-time through the widely adopted ruby fluorescence method. In order to account for pressure gradients within the sample chamber, we relied on the pressure difference measured by two ruby spheres located on opposing sides of the cell chamber, as well as the fluorescence peak broadening exhibited by each ruby. Throughout the experimental procedure, we maintained a fixed membrane pressure for each pressure point. However, it should be noted that due to thermal cycling, the exact pressure exerted by the DAC for each data point may have experienced slight variations, which were recorded accordingly.

In order to investigate the relaxation dynamics of photoexcited carriers, we employed a pulsed beam with a wavelength of 1200 nm (hν = 1.03 eV) to pump the sample. The reflectivity change was measured using an 800 nm beam (hν = 1.56 eV) as a function of delayed time. To minimize any undesired optical signals, we ensured that the pump and probe beams were cross-polarized and implemented a combination of short- and band-pass filters. To enhance measurement sensitivity and reduce 1/f noise, we utilized a lock-in amplifier for the pump beam and a mechanically oscillating optical delay line. Throughout the entire measurement process, the fluences for both the pump and probe beams were carefully controlled. The pump beam had a fluence of 1.24 mJ/cm^2 with a spot size of 80 μm full width at half maximum (FWHM), while the probe beam had a fluence of 0.17 mJ/cm^2 with a spot size of 60 μm. In addition, we ensured the reliability and comparability of the data by precisely aligning the sample and beam centers using a transmission image as a reference. This step was crucial in guaranteeing the generation of reliable and directly comparable data for our analysis.

Results

Figure 4.5 presents a representative example of time-resolved reflectivity transients acquired at T = 300 K and P = 8 GPa. The obtained trace was subjected to a double exponential decay fitting process, given by the equation:

$$\Delta R/R(t) = A_1 e^{-\frac{t}{\tau_1}} + A_2 e^{-\frac{t}{\tau_2}} + C \tag{4.1}$$

This equation combines two exponential decay terms, each characterized by its respective amplitude (A_1 and A_2) and decay time constant (τ_1 and τ_2). The fitted curves represent both the overall fit and the individual components. The fast and slow processes are depicted in dark orange and light orange, respectively. Notably, the fitting reveals a non-negligible constant term C, indicating the presence of a quasi-equilibrium state during the post-pump stage. This change may potentially be attributed to an elevated temperature that decays much slower than the first two dynamic processes.

To investigate the temperature-dependent evolution of the relaxation dynamics, we recorded the reflectivity transient traces ($\Delta R/R$) of Sr_2IrO_4 over a temperature range of 80 - 300 K, as shown in Figure 4.6. Remarkably, as the temperature decreases, a distinct observation emerges: both the characteristic time for the slow process (τ_2) and the constant term C undergo a non-monotonic evolution. Specifically, they

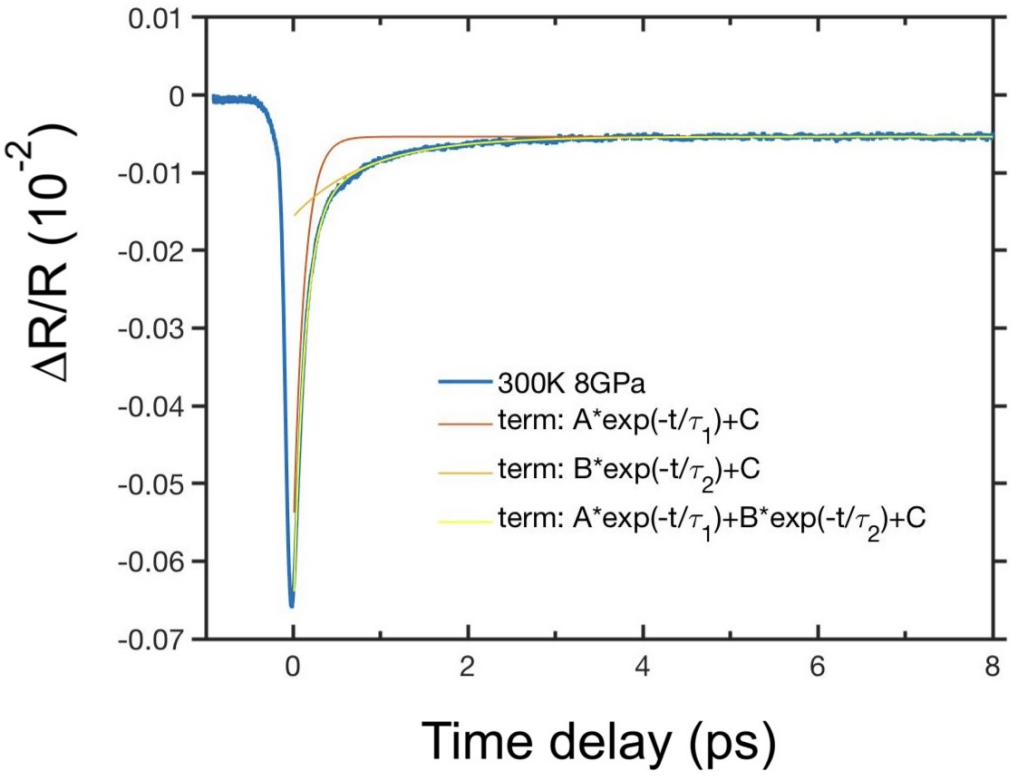

Figure 4.5: Transient reflectivity traces taken at T = 300 K and P = 8 GPa and fitted to double exponential decay. Curves show the overall fit as well as the separate components of the fit. Dark orange and light orange depict the fast and slow processes, respectively.

initially increase and subsequently decrease.

We performed a double-exponential fitting for the transient traces at each temperature and extracted the coefficients A_1, A_2, τ_1, τ_2, and C. This fitting approach proved reliable for all measured temperatures and pressures within the specified range. Figures 4.7 to 4.10 illustrate the temperature evolution of τ_1, τ_2, and C at selected pressures of 5.8 GPa, 8.2 GPa, 10.1 GPa, and 13.1 GPa. By plotting each coefficient as a function of temperature, we observed that while the fast process τ_1 showed less sensitivity to temperature, both τ_2 and C displayed prominent peaks or kinks around the magnetic transition temperature. Regarding the constant term C, we presented both the original extracted C values (black) and those normalized to the maximum value of the transient trace at time zero (red). The discrepancy between them may stem from laser power fluctuations, pulse overlap variations between the pump and probe beams, or other technical factors. Nevertheless, both sets of data exhibited

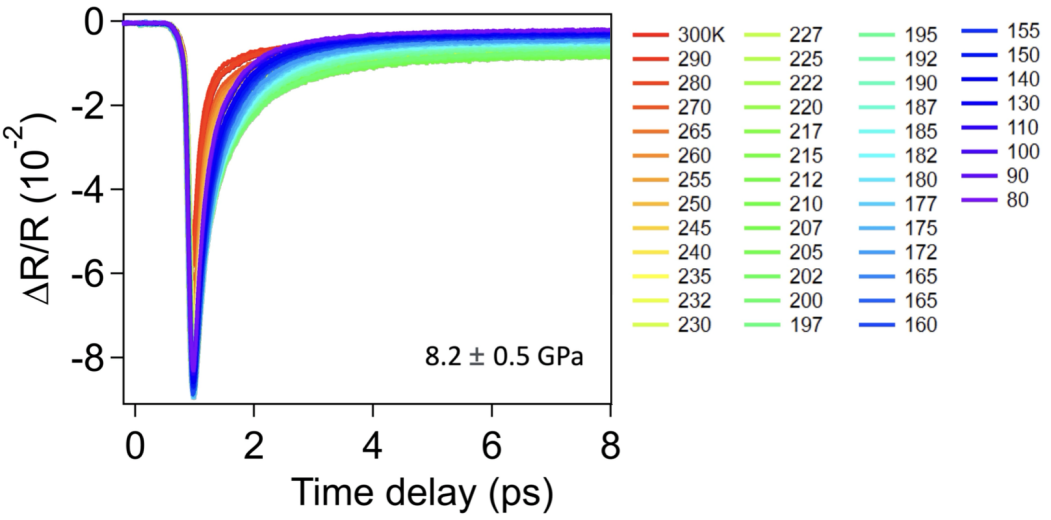

Figure 4.6: Time-resolved reflectivity traces ($\Delta R/R$) of Sr_2IrO_4 recorded over a temperature range of 80 - 300K. Notably, during the process of temperature decrease, a distinct observation emerges: the characteristic time for the slow process τ_2 and the constant C undergo a non-monotonic evolution. Specifically, they exhibit an initial increase followed by a subsequent decrease.

similar trends and peak behaviors.

Based on the distinctive peak behavior, we extracted critical temperatures corresponding to the maximum points. However, we observed a difference in the critical temperatures manifested as peaks in the τ_2 and C channels, which may be associated with different electronic processes, as discussed in (Hsieh et al., 2012).

The critical temperatures obtained from various measurement runs are summarized in Figure 4.11, with each run represented by distinct colors to differentiate the datasets. Throughout the temperature cycling process, the applied pressure was carefully determined based on the specific temperature which inevitably deviated slightly from the initial room temperature value. Notably, the pressure error bars associated with each transition point are estimated by considering the calibrated pressures for adjacent data points within a series of temperature runs. This comprehensive approach ensures an accurate assessment of pressure variations and enables a robust analysis of the pressure-dependent critical temperatures within the experimental framework. A notable observation is the high repeatability exhibited by the data across measurement runs. In the low-pressure range (below 10 GPa), the critical temperature (Tc) systematically decreases with increasing pressure. However, as the pressure is further increased, there is a turning point around 10 GPa where

Tc starts to rise. This behavior indicates a non-monotonic pressure dependence of the critical temperature and suggests the presence of intricate electronic processes at play within the material under investigation.

When comparing our findings with the phase boundary reported in the high-pressure magnetic study (Haskel, Fabbris, J. H. Kim, et al., 2020), as measured by XMCD, an interesting observation emerges. It is evident that the critical temperatures (Tc) extracted using the C parameter exhibit a good agreement with the magnetic boundary up to a pressure of 10 GPa. However, under high-pressure conditions, a noticeable deviation between the two is observed. This discrepancy may indicate a disentanglement between the Néel temperature associated with magnetic ordering and the electronic anomalies captured by the time-resolved reflectivity measurements. These results highlight the complex interplay between magnetic and electronic properties under extreme pressure conditions, warranting further investigation to fully comprehend the underlying physics in this regime.

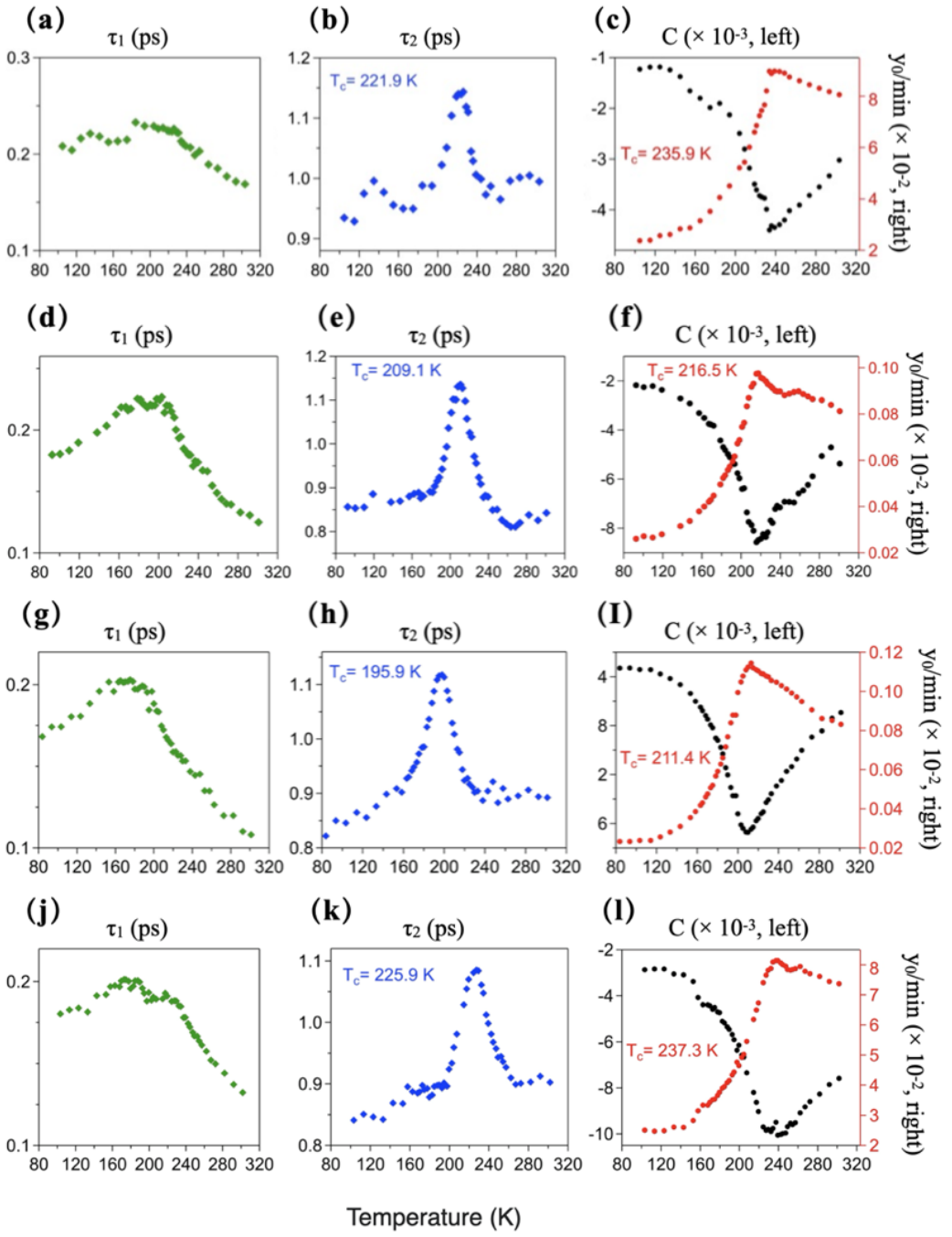

Figure 4.7: The temperature evolutions of τ_1 (a), τ_2 (b), and C (c) under a pressure of 8.2 GPa are illustrated. To mitigate fluctuations arising from laser power drifting and beam overlapping during thermal cycling, we normalized the constant term C to the maximum value of the reflectivity transient, denoted as C/min or y_0/min (shown in red in (c)). Notably, the critical temperatures extracted from the peaks of τ_2 and C are 221.9 K and 235.9 K, respectively, as indicated in the figures.
The temperature profiles for τ_1, τ_2, and C at 8.2 GPa are depicted in (d), (e), and (f), respectively, with critical temperatures noted as 209.1 and 216.5 K for τ_2 and C. At 10.1 GPa, they are shown in (g), (h), and (k), with critical temperatures of 195.9 K and 211.4 K, respectively. Finally, at 13.5 GPa, they appear in (j), (k), and (l), with critical temperatures of 225.9 K and 237.3 K.

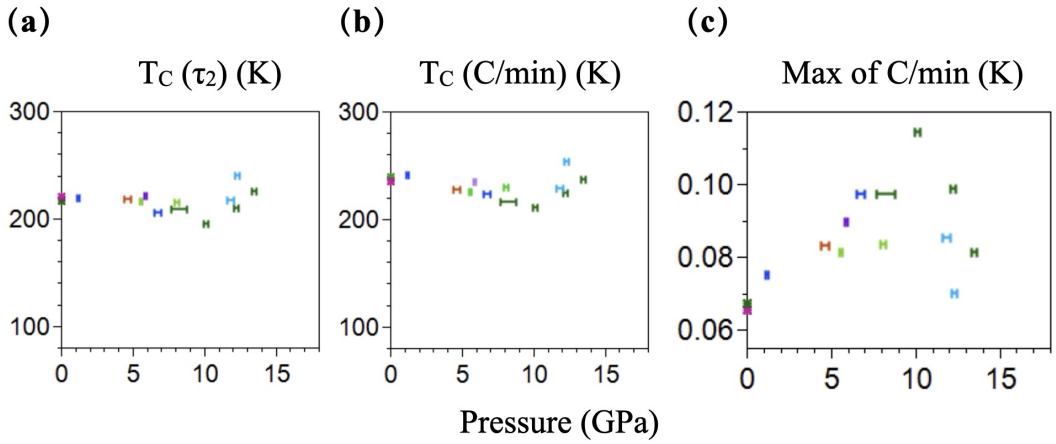

Figure 4.8: Pressure dependence of the critical temperatures tracked by τ_2 (a) and y_0/min (b). (c) depicts the maximum value of C in temperature measurements under varying pressures. The distinct colors employed in the graphical representation denote data obtained from different measurement runs. Throughout the temperature cycling process, the applied pressure is determined based on the specific temperature and is deviated from the room temperature value. Notably, the pressure error bars associated with each transition point are estimated by considering the calibrated pressures for adjacent data points within a series of temperature runs. This comprehensive approach ensures the accurate assessment of pressure variations and enables robust analysis of the pressure-dependent critical temperatures within the experimental framework.

Chapter 5

OBSERVATION AND MANIPULATION OF MAGNETIC DOMAIN STRUCTURE IN $C0_3Sn_2S_2$

In addition to inversion symmetry breaking, Weyl topology can also arise from time-reversal symmetry (TRS) breaking in magnetic systems, which provides a fertile ground to investigate the intricate relationship between magnetism and topological order. Efforts have been made to manipulate magnetism to tune the topological electronic band structure. A well-established ferromagnetic Weyl semimetal, $Co_3Sn_2S_2$, has recently attracted significant attention due to its magnetic anomalies well below the Curie temperature. Further research has shown that the distribution of magnetic domains and domain walls plays a crucial role in understanding these anomalies. In this study, we report on the observation of domain structures using a wide-field Kerr microscope, as well as the manipulation of domain structures using a mid-infrared laser and magnetic field. This study paves the way for further investigations into domain-related properties, including the potential for exotic topoogical properties shown on domain boundaries.

5.1 Introduction

Ferromagnetic Weyl semimetal

$Co_3Sn_2S_2$ is a shandite material based on cobalt, exhibiting ferromagnetic characteristics with a Curie temperature of approximately 175K (E. Liu et al., 2018; Q. Wang et al., 2018). The crystal structure of $Co_3Sn_2S_2$ comprises slabs of $CoSn_4S_2$ octahedra arranged in a hexagonal packing (A-B-C fashion) along the c axis, as depicted in FIG. 5.1a. Each Co atom is surrounded by four Sn and two S atoms, forming a distorted octahedron. These $CoSn_4S_2$ octahedra connect each other by face-sharing along the ab plane and corner-sharing along the c axis. Moreover, the Co atoms form a perfect kagome layer with corner-sharing triangles of Co atoms in the Co–Sn layer. $Co_3Sn_2S_2$ exhibits two distinct Sn sites, with half of the Sn atoms located at the centers of the kagome hexagons (FIG. 5.1b), while the other half is situated between the Co–Sn bilayers, connecting adjacent Co–Sn layers. The S atoms are situated above and below the Co–Sn layers. For plate-like $Co_3Sn_2S_2$ single crystals, the c axis is usually perpendicular to the crystal surface.

The topologically nontrivial nature of ferromagnetic $Co_3Sn_2S_2$ was first manifested

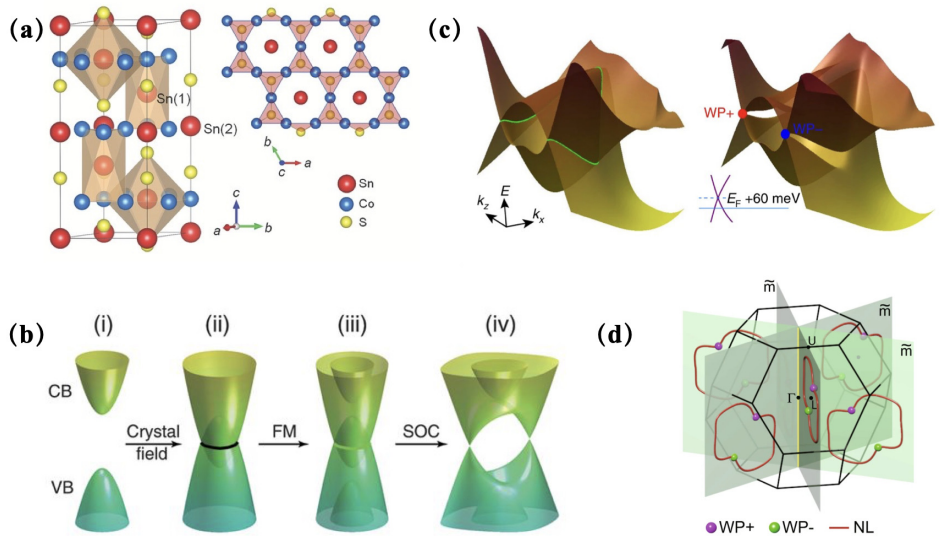

Figure 5.1: (a) Crystal structure of $Co_3Sn_2S_2$ and kagome layer made of Co atoms. The red, blue and yellow balls represent Sn, Co and S atoms, respectively. Sn atoms at Sn(1) and Sn(2) sites are label in the figure. (b) Mechanism for the magnetic WSM phase in $Co_3Sn_2S_2$. CB, conduction band; VB, valence band; FM, ferromagnetism; SOC, spin-orbital coupling. (c) Left: linear band crossings form a nodal ring in the mirror plane. Right: Spin–orbit coupling breaks the nodal ring band structure into opened gaps and Weyl nodes. The Weyl nodes are located just 60 meV above the Fermi level, whereas the gapped nodal lines are distributed around the Fermi level. (d) Schematic of the nodal line (NL) and Weyl points (WP) lying in three mirror planes of the bulk Brillouin zone. Magenta and green color points represent WP with positive (+) and negative (-) chirality, respectively. The figures are adopted from Guin et al., 2019; D. F. Liu, Liang, et al., 2019; E. Liu et al., 2018; D. F. Liu, E. K. Liu, et al., 2022 respectively

via its giant anomalous Hall effect (AHE), anomalous Hall angle (AHA) (E. Liu et al., 2018; Q. Wang et al., 2018) and anomalous Nernst effect (ANE) (Ding et al., 2019; Guin et al., 2019), and was later directly confirmed by angle-resolved photo-emission spectroscopy (ARPES) (D. F. Liu, Liang, et al., 2019; Rossi et al., 2021; D. F. Liu, E. K. Liu, et al., 2022) and corresponding first-principles calculations. The experimental ARPES results and calculation both demonstrate bulk linear dispersion of the Weyl points and the distinct surface Fermi arcs. The crystal's TRS-breaking Weyl semimetal (WSM) phase arises from a combination of crystal field, ferromagnetism (FM), and spin-orbital coupling (SOC) effects. The crystal field initially mixes the valence band (VB) and conduction band (CB), forming four-fold degenerate nodal lines, which are then lifted by the FM transition

to break TRS. When SOC is taken into account, the nodal ring structure almost opens a gap with anti-crossing lines, except for the pairs of the Weyl points, which remain. Due to the crystal's inversion and C_{3z} rotation symmetry, there are three such pairs in the first Brillouin zone, with the Weyl nodes located only 60 meV above the Fermi level, facilitating their detection in other experiments like a transverse electrical response.

The interplay between the electronic band structure and magnetic orders is a key focus when investigating magnetic topological materials. While TRB allows for the existence of Weyl nodes, the detailed magnetism determines the specific topologies. Theoretical research has shown that the energy, position, chirality, and number of Weyl nodes can be tuned by rotating the orientation of magnetic moments, with the separation of Weyl nodes being directly linked to the magnitude of the moment (Peigang Li et al., 2020; Ghimire et al., 2019). Recently, anomalies observed in multiple magnetic measurements imply the existence of a hidden phase, which has implications for the underlying band topology. When considering spatial resolution, experiments have revealed that unusual pinning and depinning of domains, as well as 2D transitions within domain walls, are critical for understanding magnetic anomalies (see next section for detailed discussion). Furthermore, the magnetic domain walls in Weyl semimetals can harbor exotic topologically nontrivial states and exhibit anomalous magnetoelectric transport and DW dynamics. To further investigate these phenomena, it is desirable to combine observations and manipulations of the domain and DW structures.

Magnetic anomalies

The FM order in $Co_3Sn_2S_2$ originates from the itinerant electrons emanating from the *d* orbitals of Co ions that are arranged in Kagome layers. Both experimental and numerical analyses have demonstrated that the magnetic moment of Co ions is approximately 0.3 μ_B/Co. The reduced value has been attributed to the formation of a local triangular Co cluster, which results in a S=1/2 state over three Co ions. $Co_3Sn_2S_2$ displays a robust magneto-crystalline anisotropy, with the magnetic moment preferentially aligned along the c-axis (E. Liu et al., 2018). Notably, the magnetization along the c-axis swiftly reaches saturation at a low field of 0.1 T, while the a-b plane boasts an exceptionally high saturation field of 20 T (C. Lee et al., 2022), confirming a predominantly out-of-plane magnetization in $Co_3Sn_2S_2$. Such a high anisotropy, coupled with modest magnetization and a quasi-2D Kagome structure, provides a fertile playground for a myriad of novel phenomena.

The magnetic structure of $Co_3Sn_2S_2$ has been long believed as a simple out-of-plane FM ordering. However, recent investigations have revealed a nonmonotonic temperature dependence of the magnetization and susceptibility below T_C, challenging this assumption (Mohamed A. Kassem et al., 2017). Specifically, a hump in field-cooled (FC) and a dip in zero-field-cooled (ZFC) magnetization measurements have been observed, which disappear at a saturation field of approximately 400 Oe, indicating a low-field anomalous state, dubbed phase-A, that is 'hidden' in the FM phase. This intriguing phenomenon has been consistently observed across a variety of samples and experimental techniques, including susceptibility, muon spin rotation (μSR) (Guguchia et al., 2020), neutron scattering (Soh et al., 2022; Q. Zhang et al., 2021), exchanged biased Hall effect (Lachman et al., 2020), and a series of microscopic measurements sensitive to localized dc and ac magnetization (Sugawara et al., 2019; Howlader et al., 2021; C. Lee et al., 2022; Shen et al., 2023). Despite these ubiquitous observations, the nature of these anomalies remains a topic of debate, with several proposed origins. For example, μSR experiments have detected two components in the μSR time spectra, suggesting a coexistence of two distinct magnetically ordered fractions with different oscillating frequencies and transition temperatures (Guguchia et al., 2020). The authors have proposed an in-plane AFM order that competes and coexists with the dominant out-of-plane FM order in the temperature range of 90K to 172K (separated from the T_C of 177K). Although the existence of AFM order is later disproved in the polarized neutron diffraction measurement (Soh et al., 2022; Q. Zhang et al., 2021), the possibility of a canted FM order is proposed and a phase transition belonging to the tiny in-plane component is evidenced by a detailed direction-dependent susceptibility measurement (Živković et al., 2022), with a sample-independent genuine transition temperature, distinctive from the sample-dependent out-of-plane anomalies. Alternatively, non-trivial spin textures, such as Skyrmions, based on the characteristic slow dynamics shown in the ac susceptibility and the geometrically induced spin frustration imprinted in the Kagome lattice (Mohamed A. Kassem et al., 2017; Sugawara et al., 2019; Mohamed A Kassem et al., 2021), and spin-glass based on the exchange biased mechanism exhibited in Hall measurement have also been proposed (Lachman et al., 2020).

While in the bulk measurement, the signal is averaged over the entire sample, spatially-resolved measurements unveil the physics of individual segments of the sample, and sets apart magnetization intrinsic to every single domain from that due to the presence of multiple domains and domain walls. Microscopic studies have been carried out through magnetic force microscopy (MFM) (Howlader et al.,

2021), Lorentz transmission electron microscopy (Lorentz TEM) (Sugawara et al., 2019), Sagnac interferometric scanning microscope (Shen et al., 2023) and scanning Kerr microscopy (C. Lee et al., 2022). From the investigation of temperature and field-dependent domain evolution, the first three studies all observe higher domain mobility under a field above 130K, thereby reaching a consensus that the 'A'-phase is a result of anomalous depinning of domain walls.

However, an intriguingly contradictory phenomenon was observed by C. Lee et al., 2022. To study the ac dynamics of the local magnetization, C. Lee et al., 2022 performed a scanning ac MOKE measurement, which not only allows for direct observation of the domain evolution with temperature but the magnetic response to an oscillating external field near domain walls as well. Upon heating, aside from the domain boundary becoming increasingly convoluted, they noted an unanticipated deep minimum of the domain displacement as well as the effective domain mobility at around 135K, which defied explanation within the confines of a standard Bloch domain wall picture. Drawing upon the step-change in the temperature dependence of the effective domain mobility, they proposed a continuous 2D transition from Bloch (where M rotates with constant magnitude in the plane of the DW) to Linear (where M is aligned along the easy axis and passes through zero at the DW center) wall type within the domain wall, which is motivated by the competition between the energy associated with the magnetic moment changing in orientation and magnitude.

The interplay between magnetic domain walls and spatially averaged responses such as electrical transport has been a subject of intensive study, with numerous opportunities for exploration and potential practical applications. DWs that link magnetism with topologically nontrivial bands are especially fascinating due to their potential to exhibit unique and compelling physics. In the context of magnetic WSM, for instance, it has been proposed that the mismatch of electron helicity across a DW could result in a DW width-independent magnetoresistance effect (Kobayashi, Ominato, and Nomura, 2018). Furthermore, theorists have suggested the existence of bound modes with a band structure resembling that of the Fermi arcs on a surface (Araki, Yoshida, and Nomura, 2016; Araki, Yoshida, and Nomura, 2018). By assuming a collinear DW texture, they have analytically derived a localized charge and equilibrium current, which may be viewed as the edge equivalent of the AHE observed in bulk magnetic WSMs.

5.2 Results and Discussion

Observation of magnetic domain structure via MOKE microscopy

As expounded upon in the preceding section, the magnetic domain and domain wall are believed to play a pivotal role in elucidating the anomalous phenomena exhibited in the magnetic measurement of $Co_3Sn_2S_2$. Moreover, the boundary state of these magnetic entities may potentially manifest intriguing transport properties that hold high application potential. Consequently, the ability to observe the domain structure with precision is indispensable in establishing a bridge between the mesoscale domain distribution and the macroscopic bulk properties. To this end, we employ the optical wide-field Kerr ellipticity-based microscopy.

In the magnetic Weyl semimetals, the intense Berry curvature associated with the Weyl points and anti-crossing line structures not only gives rise to giant anomalous Hall effect and Hall angle but also strongly enhances the magneto-optic effect (Okamura et al., 2020), providing an avenue to transform local magnetization into a spatially resolved optical signal. In order to achieve this goal, prior efforts have been made employing techniques such as magnetic force microscopy, Lorentz transmission electron microscopy, scanning Kerr microscopy, and Sagnac interferometric scanning microscopy. The Lorentz microscopy, although having a high spatial resolution of 0.85 μm, suffers from weak contrast due to small magnetization ($0.3\mu_B$/Co) resulting in compromised image quality, particularly in the vicinity of Tc, which precludes the determination of detailed spin configurations. In comparison to scanning probes, wide field microscopy offers several advantages, including a simplified setup construction, speedy image acquisition, an increased view scope, and the capability to seamlessly integrate with other optical measurements, such as CO_2 laser for domain manipulation as will be described below.

Single crystals of $Co_3Sn_2S_2$ were synthesized via the flux method. In our measurements, all samples were prepared in flake-like shapes, oriented with magnetization along the surface normal. To detect magnetic domains, we employed optical wide-field Kerr ellipticity microscopy with normal incidence light in the optical spectrum range.

To measure the Kerr ellipticity, we employ a quarter-wave plate (QWP) to convert the differences in ellipticity resulting from variations in the magnetization state between distinct domains into differences in linear polarization. This polarization difference is subsequently captured by the polarizer. The polarizer axis can be initially set to an extinction angle for the paramagnetic state, at which point the Kerr

ellipticity is zero. In the ferromagnetic phase, the two types of domains exhibit magnetization of equal magnitude but opposite orientation, leading to elliptically reflected light with opposite handedness. After passing through the QWP, these orientations are effectively transformed into a polarization rotation represented by an angle α. This angle α is directly proportional to the magnetization in a small angle limit and takes on positive or negative values for the two types of domains, respectively. By slightly rotating the polarizer axis away from the initial position by an angle ϕ, the angle between beam polarization ϕ and the polarizer axis is denoted as $\beta = 90 + \alpha - \phi$. As a result, the intensity becomes proportional to $\cos(\beta)$. Consequently, the domains with α aligned in the opposite direction to ϕ are favored, appearing brighter in the image and revealing their boundaries. Ideally, the optimal contrast is achieved when α equals ϕ, resulting in a vanishing signal for one of the domains. However, in practice, due to imperfections in the polarizer's extinction ratio and the sensitivity limitations of the signal-receiving camera, a larger angle ϕ is used. Furthermore, to enhance image contrast, improve the visibility of magnetic features, and mitigate non-uniform illumination, we capture two sets of images with positive and negative ϕ, which we refer to as anti-symmetric images. We then subtract the two anti-symmetric images and divide the result by their average for each pixel. In the difference image, the intensity for each pixel is proportional to $\beta(\phi) - \beta(-\phi)$. To optimize domain observation, we experimentally determined that a deviation angle of 7.5 degrees from the extinction angle provided the best image contrast. Figure 5.10 (a) and (b) display the direct output images captured by the CMOS sensor when the deviation angle was set to positive and negative 7.5 degrees, respectively, showing weak domain contrast. Figure 5.10 (c) illustrates the difference image, where the domain features are more clearly discernible. The color bar represents the pixel-wise subtraction divided by the average. However, it should be noted that the non-uniformity of the reflected beam polarization induced by either the optical system or the sample itself hinders the quantitative analysis of magnetization at each site. Comparing the Kerr images across different samples is therefore not valid. Instead, the obtained measurements serve as relative values to demonstrate the domain structures. For more technical details on our measurement setup, please refer to Chapter 2.3, which includes a schematic diagram of the experimental arrangement provided in Figure 2.3.1.

In 5.3, a representative Kerr image acquired after being zero-field-cooled (ZFC) to a base temperature of 80 K is shown. The distinct contrast between dark and bright regions reveals domains with magnetization parallel and anti-parallel to the surface

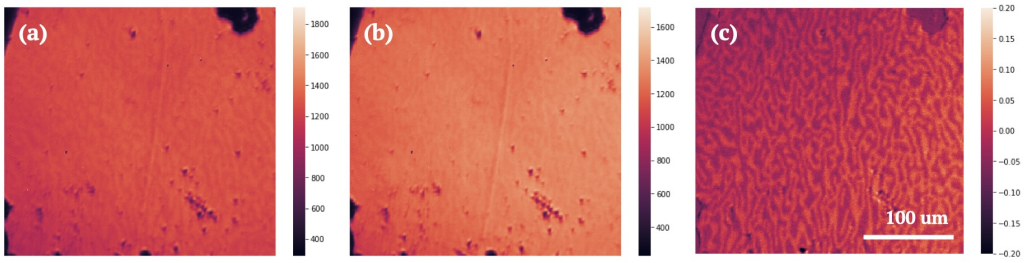

Figure 5.2: Direct output Kerr images acquired from the CMOS and their corresponding difference image. Panel (a) and (b) show the direct output images captured by the CMOS with a deviation angle of +7.5 degrees and -7.5 degrees, respectively. The color bars indicate the intensity values measured by the CMOS for each pixel. Panel (c) displays the difference image, revealing clearer domain features. The color bar represents the pixel-wise subtraction divided by the average.

normal, respectively. In the absence of an external magnetic field, the domains exhibit a labyrinthine pattern with a typical width of approximately 10 μm. In thinner flake-like specimens, the domain width is reduced. 5.4 shows labyrinthine domains exhibited on samples with varying thicknesses. After thermal cycling, the mesoscopic domain distribution evolves dynamically, suggesting that domains are not pinned by external factors such as strain or impurities generated during sample growth or mounting.

5.3 provides a comprehensive depiction of the intricate temperature evolution observed within the labyrinthine domain structure under ZFW. Below the threshold of 140 K, the domain distributions exhibit remarkable stability, remaining largely unchanged. However, as the temperature surpasses this critical point, a gradual redistribution process unfolds, indicative of a depinning phenomenon taking place. Remarkably, within the temperature range of 160 K to 170 K, the domain density experiences a substantial surge. Eventually, upon reaching the T_C, the domains vanish altogether.

These observations align with the conventional viewpoint, suggesting that in the low-temperature regime, domain wall motion remains dormant due to robust pinning effects. However, as the temperature rises, thermal depinning stimulates the activation of domain wall motion. The observed redistribution arises from the interplay between magneto-static energy and domain wall energy (Shen et al., 2023). Notably, the low-field magnetization during ZFW exhibits an anomalous deviation from the expected monotonic decreasing curve, a departure absent under saturat-

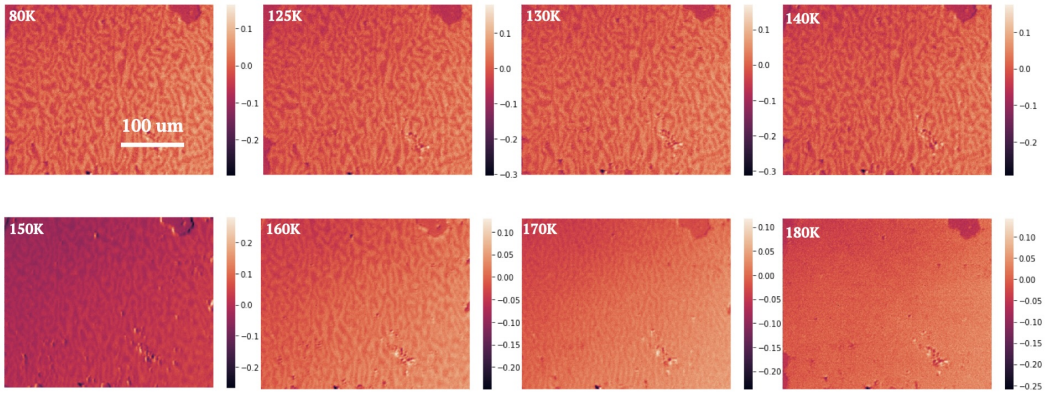

Figure 5.3: The temperature evolution of the labyrinthine domain structure under zero field warming. The sample, approximately 100 μm thick, exhibits domains with an average width of around 10 μm. Below 140 K, the domain distributions remain largely unchanged. However, as the temperature rises above 140 K, a gradual redistribution process occurs, indicating a depinning process. Notably, between 160 K and 170 K, the domain density significantly increases. Eventually, at T_C, the domains completely disappear. The color bar represents the pixel-wise subtraction of two anti-symmetric images divided by the average.

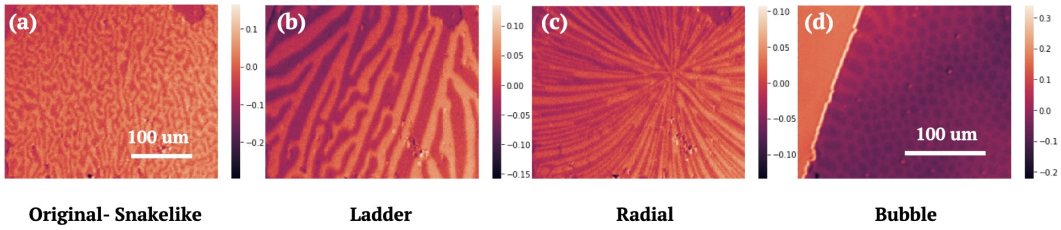

Figure 5.4: Domain structures obtained under different experimental conditions. (a) After zero field cooling, $Co_3Sn_2S_2$ naturally exhibits a labyrinthine, snake-like domain structure. (b) Following a field cooling/zero field warming (FC/ZFW) protocol, a single saturated domain persists until approximately 140 K, beyond which domains with nearly equal populations of both types emerge. The ladder domain structure is observed just above the temperature of sudden appearance. (c) If a CO_2 laser is illuminated onto the sample during cooling, a radial domain structure is formed. (d) When the sample is rapidly cooled across the Curie temperature under a weak magnetic field, a bubble-like domain structure is formed. The color bar represents the pixel-wise subtraction of two anti-symmetric images divided by the average. (a), (b) and (c) share the same scale bar.

ing field conditions. This peculiar behavior hints at a nontrivial evolution of the pinning/depinning process governing domain wall motion. To gain deeper insights into the domain structure, it becomes imperative to extract additional information,

such as domain width or domain wall density, through systematic digital image processing techniques.

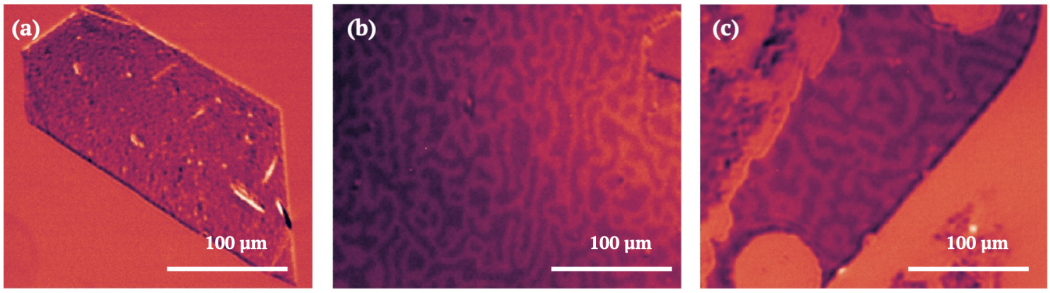

Figure 5.5: Labyrinthine domains exhibited on samples with varying thickness. (a), (b), and (c) correspond to samples with a thickness of approximately 10 μm, 100 μm, and 200 μm, respectively. A noticeable trend emerges: the domain width expands as the sample thickness increases. The color bar represents the pixel-wise subtraction of two anti-symmetric images divided by the average.

Manipulation of magnetic domains with magnetic field and CO_2 laser

When investigating magnetic anomalies, the presence of magnetic domains has hindered our ability to fully comprehend the results of bulk magnetic measurements. Although the advent of the Kerr microscope has allowed us to observe the domain structure, the ability to manipulate domains on-demand facilitates the design of sophisticated experiments capable of distinguishing the bulk signal contributed by various domain and domain wall configurations. Furthermore, controlling the density and configuration of these walls will prove instrumental in gaining a deeper understanding of the exotic and fascinating edge states that may emerge within domain walls.

There are several methods for manipulating ferromagnetic domains, with the most widely used and efficient being the use of an external magnetic field. Other methods include passing an electric current, applying mechanical strains or hydrostatic pressure, chemical doping, and applying laser illumination. Among these, the laser has the significant advantage of being non-invasive and easily and precisely controlled.

Continuous wave (CW) and ultrafast lasers have been creatively utilized to control domains. In ferro- and ferrimagnetic materials, magnetization reversals have been realized using circularly (CP) pico- or femtosecond laser pulses through opto-magnetism, such as the inverse Faraday effect (Kalashnikova, Kimel, and Pisarev, n.d.). The target magnetization is determined by the helicity of the laser pulses,

and the reversal process is referred to as all-optical helicity-dependent switching (AO-HDS) (Mangin et al., 2014; Stanciu et al., 2007; Lambert et al., 2014). In such experiments, laser pulses are directed at samples that have already been cooled down into the magnetically ordered phase. Another noteworthy study on $Co_3Sn_2S_2$ was carried out by Yoshikawa et al (Yoshikawa et al., 2022). They achieved magnetization reversal on a thin film of $Co_3Sn_2S_2$ with CP MIR pulsed laser through magnetic circular dichroism. With each single pulse, due to the inequivalent heating, one type of domain was selectively heated above Tc and reordered into two oppositely oriented states with a certain probability. After several pulses, that type of domain was almost reversed.

Laser illumination has been established as a powerful tool for interacting with and controlling the magnetic order in several cases. However, most studies focus on local domain switching or selective formation of a homogeneous domain in a specific area, which is undoubtedly important for potentially high impact on data storage and manipulation or preventing signals from small domains from canceling each other out. To study the effect of different domain and domain wall structures, a methodology for achieving overall control of domain shape, orientation, and density in a specific area is necessary. In the following section, we will demonstrate how we use a mid-infrared CO_2 laser and magnetic field applied with a permanent magnet to obtain a variety of domains with different shapes, orientations, and densities. Figure 5.4 shows examples of the domain patterns we obtained.

Labyrinthine domain

The labyrinthine domains are formed after ZFC or low-field-cooling. The higher the field, the wider the domain width. The temperature evolution of the labyrinthine domains has been elaborated on in the last section.

Radial-patterned domain

By shining CW mid-infrared light on $Co_3Sn_2S_2$ while cooling it below the critical temperature, radial-patterned domains (5.3) are generated, where the center of the radial pattern aligns with the focus of the CO_2 laser. Moving the field of view away from the radial center reveals the cessation of domain rays and the emergence of labyrinthine domains beyond a circular range. Increasing the light power extends the circular range, expanding the pattern. Notably, the pattern shape and population ratio of domains with moments parallel or antiparallel to the c-axis remains unaffected by

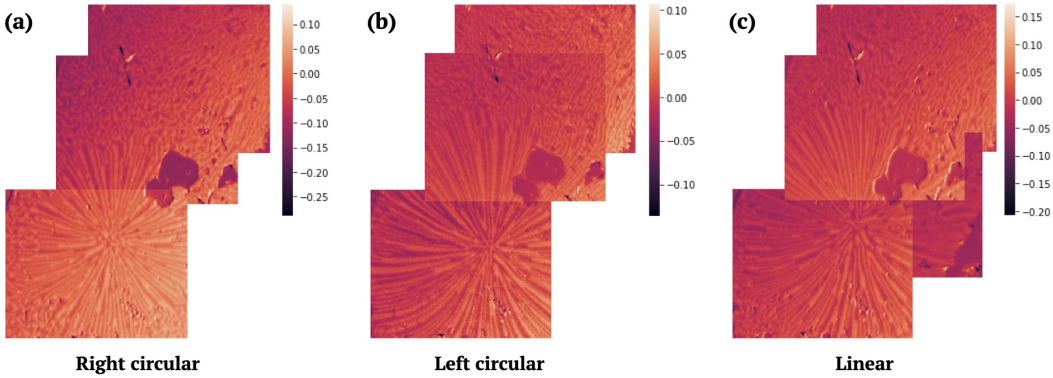

Figure 5.6: CO_2 laser helicity dependence of the radial domain formation. The domain patterns are observed after subjecting the sample to laser cooling using a CO_2 laser with right circular polarization (a), left circular polarization (b), or linear polarization (c). Interestingly, no significant differences are observed among the resulting domain patterns, indicating a lack of helicity dependence in the formation process. The color bar represents the pixel-wise subtraction of two anti-symmetric images divided by the average.

the helicity of the training light. This observation suggests that the pattern's origin lies in laser heating, specifically the thermal gradient, rather than polarization-dependent opto-magnetism.

Upon crossing Tc, the illuminated portion of the sample remains above Tc due to laser heating, while regions farther from the laser illumination transition into labyrinthine domains. By precisely controlling the temperature decrease, spins along a circular region of the sample freeze into the same state as their neighboring spins in the outer ring, resulting in the gradual formation of domain rays upon cooling from the outer regions. To verify this proposition, the laser is intentionally blocked during the cooling process, and Kerr images are captured, as depicted in 5.7 (b) demonstrating the connection of domain rays between two regions of labyrinthine domains. This concept enables the deliberate creation of domain patterns by manipulating the thermal distribution. For instance, the implementation of a cylindrical lens would facilitate the generation of a linear thermal gradient, thereby inducing parallel domains.

Unfortunately, a current limitation arises due to the shared light path between the CO_2 training laser and the normal incidence Kerr measurement, necessitating the resolution of an obstacle in monitoring the process of radial domain formation during cooling. In future, this challenge can be overcome by introducing an oblique incidence for the CO_2 training, offering a promising solution for the continuous

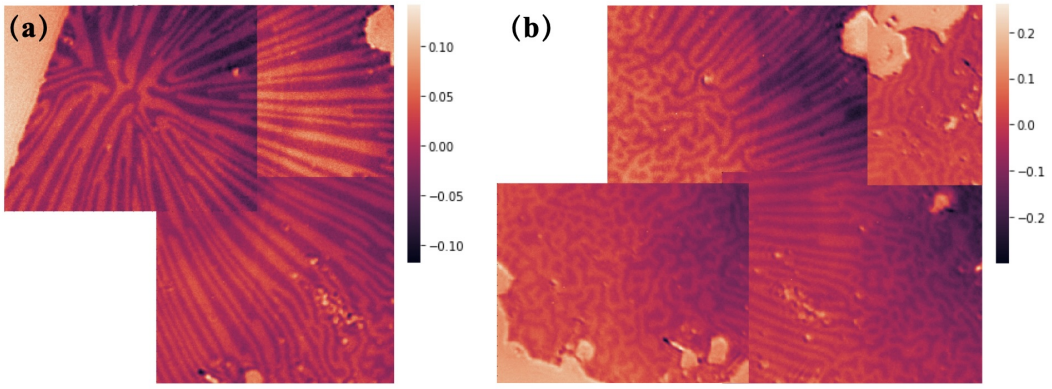

Figure 5.7: Radial domain formation observed in the sample following one-stage (a) or two-stage laser cooling (b). (a)In the one-stage cooling process, the sample was cooled directly to 80K with laser shined onto the sample. (b)In the two-stage cooling process, the sample was cooled directly to 80K, and above 165K, the laser was activated, while below 165K, the laser was blocked. Remarkably, the resulting images reveal the presence of snake-like domains both within and outside the areas occupied by the radial domains. The color bar represents the pixel-wise subtraction of two anti-symmetric images divided by the average.

monitoring and investigation of the radial domain formation process.

Subjecting the sample to an external magnetic field and subsequently imaging it after the magnetic field is removed reveals an expansion in domain width, corresponding to an increase in magnetic field strength. Remarkably, this behavior is exhibited by both domains with magnetization parallel and antiparallel to the external field, as depicted in 5.8. This discovery presents a promising avenue for the continuous adjustment of domain and domain wall density within the same sample area.

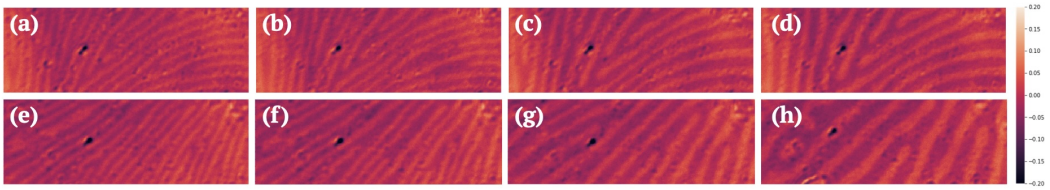

Figure 5.8: The domain width expands alongside an increase in magnetic field strength. Notably, both domains with magnetization parallel and antiparallel to the external field exhibit this behavior. Figures (a) to (d) and figure (e) to (h) depict two independent measurement runs. The color bar represents the pixel-wise subtraction of two anti-symmetric images divided by the average.

Ladder domain

Deep within the ferromagnetic phase, magnetic anomalies manifest themselves in various types of measurements, such as μSR, neutron scattering, exchanged biased Hall measurement, susceptibility, and magnetization. However, the multitude of experimental results often appear perplexing and contradictory. An intriguing observation arises from the FC/ZFW process, where both neutron scattering and magnetization measurements exhibit a sudden jump (Soh et al., 2022), indicating a vanishing of bulk magnetization. Implementing the same protocol, we initially cool the sample under a sufficiently strong magnetic field to saturate its magnetization, observing a single-domain state at the base temperature. As we embark on the zero-field warming process, this single-domain state persists until approximately 140K, beyond which domains emerge with a nearly equal population of both types. To better understand the temperature dependence and characteristics of domain formation, we refined our measurements, employing smaller temperature increments of 0.1K. Remarkably, within this narrow temperature range, we observed a sudden and abrupt emergence of domains. As the temperature continued to rise, the density of these domains progressively increased.

It is important to note that this sharp transition occurs within a temperature window of less than 0.1K and is highly dependent on the specific characteristics such as shape and size of the sample. We tentatively attribute this abrupt jump in the domain structure to the demagnetization factor, which is influenced by the shape of the sample. It is worth mentioning that this observation may differ from other sample-independent anomalies observed in alternative experiments. For example, the 2D transition occurring within the DWs manifested as a deep minimum of DW mobility in ac Kerr imaging, is expected to be sample-independent as an intrinsic transition (C. Lee et al., 2022). However, to gain a comprehensive understanding of the relation between our observation of domain structure and the previously reported magnetic anomalies, further systematic investigations are warranted.

Bubble domain

The observation of a bubble lattice on ferromagnetic systems has provided intriguing insights into the domain formation process. When the sample is rapidly cooled under a weak magnetic field, a distinct bubble-lattice structure emerges. While previous studies have reported the existence of round-shaped domains within a narrow temperature range of 165K to 175K, this is the first time that a lattice-like domain structure has been observed, persisting at least until 80K.

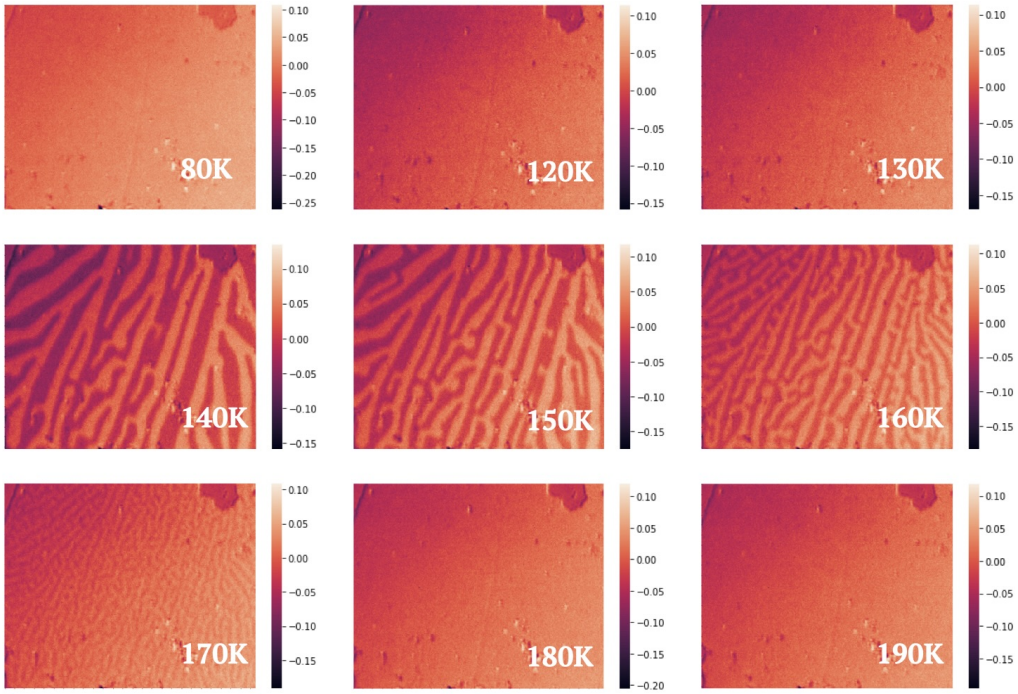

Figure 5.9: Temperature evolution of the saturated single domain structure under zero field warming demonstrates an abrupt appearance of ladder domains around 140K. The critical temperature exhibits a strong dependence on the sample shape and external magnetic field, indicating the influence of the demagnetization factor. The color bar represents the pixel-wise subtraction of two anti-symmetric images divided by the average.

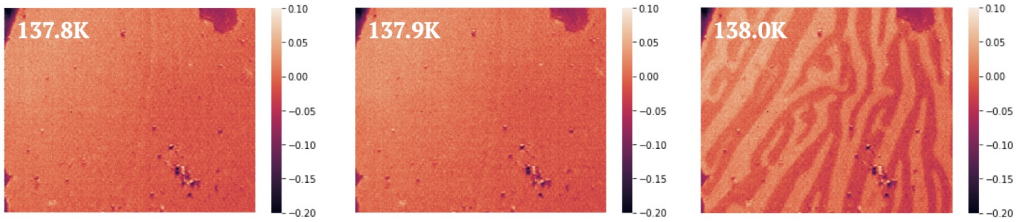

Figure 5.10: Temperature evolution of the saturated single domain structure under zero field warming near the critical temperature of 138.0K with temperature increments of 0.1K. The color bar represents the pixel-wise subtraction of two anti-symmetric images divided by the average.

The bubble lattice exhibits intriguing similarities to skyrmions, which are topologically protected vortex-like spin textures. Theoretical investigations have proposed the spontaneous formation of triangular-lattice skyrmions facilitated by the Dzyaloshinskii-Moriya (DM) interaction. Experimental confirmation of such skyrmion

lattices has been achieved in noncentrosymmetric cubic chiral and rotationally symmetric polar crystals under finite fields, in proximity to the Curie temperature (TC). However, it is worth noting that the size of the observed bubble domains far exceeds the typical dimensions associated with skyrmions, with sizes reaching up to 100nm.

An alternative theoretical perspective suggests that the formation of domain tubes, akin to the observed bubble lattice, may arise from the interplay of competing magnetic interactions (Garel and Doniach, 1982). Introducing a weak magnetic field during the cooling process or its abrupt application generates a distinctive honeycomb-like lattice structure referred to as the bubble lattice within the inner portion of the sample.

Overall, the observation of the bubble lattice in our ferromagnetic systems provides valuable insights into the complex dynamics of domain formation. While the origin of these lattice-like structures may not be directly attributed to skyrmions, their existence highlights the intricate interplay between competing magnetic forces and offers intriguing possibilities for further exploration and understanding of domain physics in ferromagnetic materials.

Chapter 6

CLOSING REMARKS AND OUTLOOK

In correlated electron systems, the intricate interplay among various degrees of freedom gives rise to rich phase diagrams, replete with exotic phenomena. As a result, subtle external stimuli can shift the delicate balance between coexisting and competing ground states. Among the array of available methodologies, pressure tuning via diamond anvil cells (DACs) stands out due to its disorder-free nature and continuous tunability.

Despite its efficacy, the DAC presents challenges for various measurement techniques. Notably, methods requiring close point contacts, such as scanning tunneling microscopy (STM), and electron-based spectroscopic approaches, like angle-resolved photoemission spectroscopy (ARPES), encounter limitations within this setup. However, the inherent transparency of diamonds across a wide spectral range renders DACs naturally amenable to optical measurements. This compatibility broadens the horizons for investigating quantum materials under high pressure, leveraging techniques such as second harmonic generation (SHG) and transient reflectivity, which remain compatible with the diamond environment.

In this thesis, we presented a compendium of compelling examples. We demonstrated the possibility of performing high-sensitivity SHG polarimetry measurements in a DAC. Using this technique, we revealed a connection between the polar axis and the giant optical nonlinearity of the Weyl semimetal TaAs and showed how pressure can be used to tune this effect in situ. We also demonstrated the ability to perform time-resolved optical reflectivity measurements in a DAC. We applied this technique to Sr_2IrO_4 to show anomalies in the carrier relaxation dynamics under high pressure, suggesting a complex interplay between crystallographic structure, electronic structure, and magnetism.

Going forward, we anticipate that these techniques can also contribute to the understanding of quantum criticality - the behavior of materials across zero-temperature phase transitions that are driven by quantum fluctuations. Hydrostatic pressure serves as an ideal knob to fine-tune the system continuously across a quantum phase transition. By deploying probes such as SHG and ultrafast pump-probe spectroscopy, it may be possible to detect subtle symmetry-breaking signals, gap formations, and

even their spatial inhomogeneity near a quantum critical point.

In conclusion, the integration of high-pressure techniques with advanced optical measurements presents a powerful toolkit for probing and understanding the complex behaviors of correlated electron systems. This approach holds promise for accessing and interrogating new regions of phase space that may harbor new structural and electronic phases of matter.

BIBLIOGRAPHY

Araki, Yasufumi, Akihide Yoshida, and Kentaro Nomura (Sept. 2016). "Universal charge and current on magnetic domain walls in Weyl semimetals". en. In: *Physical Review B* 94.11, p. 115312. ISSN: 2469-9950, 2469-9969. DOI: 10.1103/PhysRevB.94.115312. URL: https://link.aps.org/doi/10.1103/PhysRevB.94.115312 (visited on 05/23/2023).

– (July 2018). "Localized charge in various configurations of magnetic domain wall in a Weyl semimetal". en. In: *Physical Review B* 98.4, p. 045302. ISSN: 2469-9950, 2469-9969. DOI: 10.1103/PhysRevB.98.045302. URL: https://link.aps.org/doi/10.1103/PhysRevB.98.045302 (visited on 05/23/2023).

Armitage, N. P., E. J. Mele, and Ashvin Vishwanath (Jan. 2018). "Weyl and Dirac semimetals in three-dimensional solids". In: *Reviews of Modern Physics* 90.1. Publisher: American Physical Society, p. 015001. DOI: 10.1103/RevModPhys.90.015001. URL: https://link.aps.org/doi/10.1103/RevModPhys.90.015001 (visited on 02/25/2022).

Balents, Leon (Mar. 2010). "Spin liquids in frustrated magnets". en. In: *Nature* 464.7286, pp. 199–208. ISSN: 0028-0836, 1476-4687. DOI: 10.1038/nature08917. URL: https://www.nature.com/articles/nature08917 (visited on 05/31/2023).

Biesner, Tobias and Ece Uykur (Dec. 2019). "Pressure-Tuned Interactions in Frustrated Magnets: Pathway to Quantum Spin Liquids?" en. In: *Crystals* 10.1, p. 4. ISSN: 2073-4352. DOI: 10.3390/cryst10010004. URL: https://www.mdpi.com/2073-4352/10/1/4 (visited on 05/31/2023).

Burkov, A. A. (Oct. 2014). "Anomalous Hall Effect in Weyl Metals". In: *Phys. Rev. Lett.* 113 (18), p. 187202. DOI: 10.1103/PhysRevLett.113.187202. URL: https://link.aps.org/doi/10.1103/PhysRevLett.113.187202.

Chen, Chunhua et al. (Apr. 2020). "Persistent insulating state at megabar pressures in strongly spin-orbit coupled S r 2 Ir O 4". en. In: *Physical Review B* 101.14, p. 144102. ISSN: 2469-9950, 2469-9969. DOI: 10.1103/PhysRevB.101.144102. URL: https://link.aps.org/doi/10.1103/PhysRevB.101.144102 (visited on 06/02/2023).

Cheng, J. G. et al. (Nov. 2011). "High-Pressure Sequence of Ba 3 NiSb 2 O 9 Structural Phases: New S = 1 Quantum Spin Liquids Based on Ni 2 +". en. In: *Physical Review Letters* 107.19, p. 197204. ISSN: 0031-9007, 1079-7114. DOI: 10.1103/PhysRevLett.107.197204. URL: https://link.aps.org/doi/10.1103/PhysRevLett.107.197204 (visited on 05/31/2023).

Dasenbrock-Gammon, Nathan et al. (Mar. 2023). "Evidence of near-ambient superconductivity in a N-doped lutetium hydride". en. In: *Nature* 615.7951, pp. 244–250. ISSN: 0028-0836, 1476-4687. DOI: 10.1038/s41586-023-05742-0. URL:

https://www.nature.com/articles/s41586-023-05742-0 (visited on 05/31/2023).

Ding, Linchao et al. (Dec. 2019). "Intrinsic Anomalous Nernst Effect Amplified by Disorder in a Half-Metallic Semimetal". en. In: *Physical Review X* 9.4, p. 041061. ISSN: 2160-3308. DOI: 10.1103/PhysRevX.9.041061. URL: https://link.aps.org/doi/10.1103/PhysRevX.9.041061 (visited on 05/23/2023).

Dunstan, D J and I L Spain (Nov. 1989). "Technology of diamond anvil high-pressure cells: I. Principles, design and construction". en. In: *Journal of Physics E: Scientific Instruments* 22.11, pp. 913–923. ISSN: 0022-3735. DOI: 10.1088/0022-3735/22/11/004. URL: https://iopscience.iop.org/article/10.1088/0022-3735/22/11/004 (visited on 05/31/2023).

Erickson, A. S. et al. (July 2007). "Ferromagnetism in the Mott Insulator Ba 2 NaOsO 6". en. In: *Physical Review Letters* 99.1, p. 016404. ISSN: 0031-9007, 1079-7114. DOI: 10.1103/PhysRevLett.99.016404. URL: https://link.aps.org/doi/10.1103/PhysRevLett.99.016404 (visited on 05/31/2023).

Gao, Y. et al. (Feb. 2020). "Chiral terahertz wave emission from the Weyl semimetal TaAs". en. In: *Nature Communications* 11.1. Number: 1 Publisher: Nature Publishing Group, p. 720. ISSN: 2041-1723. DOI: 10.1038/s41467-020-14463-1. URL: https://www.nature.com/articles/s41467-020-14463-1 (visited on 02/25/2022).

Garel, T. and S. Doniach (July 1982). "Phase transitions with spontaneous modulation-the dipolar Ising ferromagnet". In: *Phys. Rev. B* 26 (1), pp. 325–329. DOI: 10.1103/PhysRevB.26.325. URL: https://link.aps.org/doi/10.1103/PhysRevB.26.325.

Georges, Antoine, Luca De' Medici, and Jernej Mravlje (Apr. 2013). "Strong Correlations from Hund's Coupling". en. In: *Annual Review of Condensed Matter Physics* 4.1, pp. 137–178. ISSN: 1947-5454, 1947-5462. DOI: 10.1146/annurev-conmatphys-020911-125045. URL: https://www.annualreviews.org/doi/10.1146/annurev-conmatphys-020911-125045 (visited on 05/31/2023).

Ghimire, Madhav Prasad et al. (Dec. 2019). "Creating Weyl nodes and controlling their energy by magnetization rotation". en. In: *Physical Review Research* 1.3, p. 032044. ISSN: 2643-1564. DOI: 10.1103/PhysRevResearch.1.032044. URL: https://link.aps.org/doi/10.1103/PhysRevResearch.1.032044 (visited on 05/23/2023).

Gor'kov, Lev P. and Vladimir Z. Kresin (Jan. 2018). "*Colloquium* : High pressure and road to room temperature superconductivity". en. In: *Reviews of Modern Physics* 90.1, p. 011001. ISSN: 0034-6861, 1539-0756. DOI: 10.1103/RevModPhys.90.011001. URL: https://link.aps.org/doi/10.1103/RevModPhys.90.011001 (visited on 05/31/2023).

Guguchia, Z. et al. (Jan. 2020). "Tunable anomalous Hall conductivity through volume-wise magnetic competition in a topological kagome magnet". en. In: *Nature Communications* 11.1, p. 559. ISSN: 2041-1723. DOI: 10.1038/s41467-020-14325-w. URL: https://www.nature.com/articles/s41467-020-14325-w (visited on 05/23/2023).

Guin, Satya N. et al. (June 2019). "Zero-Field Nernst Effect in a Ferromagnetic Kagome-Lattice Weyl-Semimetal Co $_3$ Sn $_2$ S $_2$". en. In: *Advanced Materials* 31.25, p. 1806622. ISSN: 0935-9648, 1521-4095. DOI: 10.1002/adma.201806622. URL: https://onlinelibrary.wiley.com/doi/10.1002/adma.201806622 (visited on 05/23/2023).

Guo, ZhaoPeng et al. (Jan. 2018). "High-pressure phases of Weyl semimetals NbP, NbAs, TaP, and TaAs". en. In: *Science China Physics, Mechanics & Astronomy* 61.3, p. 038211. ISSN: 1869-1927. DOI: 10.1007/s11433-017-9126-6. URL: https://doi.org/10.1007/s11433-017-9126-6 (visited on 02/25/2022).

Gupta, Satyendra Nath et al. (May 2018). "Pressure-induced Lifshitz and structural transitions in NbAs and TaAs: experiments and theory". eng. In: *Journal of Physics. Condensed Matter: An Institute of Physics Journal* 30.18, p. 185401. ISSN: 1361-648X. DOI: 10.1088/1361-648X/aab5e3.

Hansmann, P. et al. (July 2013). "Mott-Hubbard transition in V $_2$ O $_3$ revisited: Mott-Hubbard transition in V $_2$ O $_3$ revisited". en. In: *physica status solidi (b)* 250.7, pp. 1251–1264. ISSN: 03701972. DOI: 10.1002/pssb.201248476. URL: https://onlinelibrary.wiley.com/doi/10.1002/pssb.201248476 (visited on 05/31/2023).

Harter, J. W., L. Niu, et al. (Oct. 2015). "High-speed measurement of rotational anisotropy nonlinear optical harmonic generation using position-sensitive detection". In: *Opt. Lett.* 40.20, pp. 4671–4674. DOI: 10.1364/OL.40.004671. URL: https://opg.optica.org/ol/abstract.cfm?URI=ol-40-20-4671.

Harter, J. W., Z. Y. Zhao, et al. (Apr. 2017). "A parity-breaking electronic nematic phase transition in the spin-orbit coupled metal Cd2Re2O7". In: *Science* 356.6335. Publisher: American Association for the Advancement of Science, pp. 295–299. DOI: 10.1126/science.aad1188. URL: https://www.science.org/doi/full/10.1126/science.aad1188 (visited on 02/26/2022).

Haskel, D., G. Fabbris, J. H. Kim, et al. (Feb. 2020). "Possible Quantum Paramagnetism in Compressed Sr 2 IrO 4". en. In: *Physical Review Letters* 124.6, p. 067201. ISSN: 0031-9007, 1079-7114. DOI: 10.1103/PhysRevLett.124.067201. URL: https://link.aps.org/doi/10.1103/PhysRevLett.124.067201 (visited on 06/02/2023).

Haskel, D., G. Fabbris, Mikhail Zhernenkov, et al. (July 2012). "Pressure Tuning of the Spin-Orbit Coupled Ground State in Sr 2 IrO 4". en. In: *Physical Review Letters* 109.2, p. 027204. ISSN: 0031-9007, 1079-7114. DOI: 10.1103/PhysRevLett.

109.027204. URL: https://link.aps.org/doi/10.1103/PhysRevLett.109.027204 (visited on 06/02/2023).

He, Lanpo et al. (Sept. 2016). "Pressure-induced superconductivity in the three-dimensional topological Dirac semimetal Cd3As2". en. In: *npj Quantum Materials* 1.1, p. 16014. ISSN: 2397-4648. DOI: 10.1038/npjquantmats.2016.14. URL: https://www.nature.com/articles/npjquantmats201614 (visited on 05/31/2023).

Howlader, Sandeep et al. (Feb. 2021). "Domain structure evolution in the ferromagnetic Kagome-lattice Weyl semimetal Co $_3$ Sn $_2$ S $_2$". en. In: *Journal of Physics: Condensed Matter* 33.7, p. 075801. ISSN: 0953-8984, 1361-648X. DOI: 10.1088/1361-648X/abc4d1. URL: https://iopscience.iop.org/article/10.1088/1361-648X/abc4d1 (visited on 05/23/2023).

Hsieh, D. et al. (July 2012). "Observation of a metal-to-insulator transition with both Mott-Hubbard and Slater characteristics in Sr 2 IrO 4 from time-resolved photocarrier dynamics". en. In: *Physical Review B* 86.3, p. 035128. ISSN: 1098-0121, 1550-235X. DOI: 10.1103/PhysRevB.86.035128. URL: https://link.aps.org/doi/10.1103/PhysRevB.86.035128 (visited on 06/02/2023).

Huang, Xiaochun et al. (Aug. 2015). "Observation of the Chiral-Anomaly-Induced Negative Magnetoresistance in 3D Weyl Semimetal TaAs". In: *Physical Review X* 5.3. Publisher: American Physical Society, p. 031023. DOI: 10.1103/PhysRevX.5.031023. URL: https://link.aps.org/doi/10.1103/PhysRevX.5.031023 (visited on 02/25/2022).

Imada, Masatoshi, Atsushi Fujimori, and Yoshinori Tokura (1998). "Metal-insulator transitions". en. In: *Rev. Mod. Phys.* 70.4.

Jia, Shuang, Su-Yang Xu, and M. Zahid Hasan (Nov. 2016). "Weyl semimetals, Fermi arcs and chiral anomalies". en. In: *Nature Materials* 15.11. Number: 11 Publisher: Nature Publishing Group, pp. 1140–1144. ISSN: 1476-4660. DOI: 10.1038/nmat4787. URL: https://www.nature.com/articles/nmat4787 (visited on 02/25/2022).

Kalashnikova, A M, A V Kimel, and R V Pisarev (n.d.). "Ultrafast optomagnetism". en. In: ().

Kassem, Mohamed A et al. (Jan. 2021). "Unconventional critical behaviors at the magnetic phase transition of Co $_3$ Sn $_2$ S $_2$ kagomé ferromagnet". en. In: *Journal of Physics: Condensed Matter* 33.1, p. 015801. ISSN: 0953-8984, 1361-648X. DOI: 10.1088/1361-648X/abaf94. URL: https://iopscience.iop.org/article/10.1088/1361-648X/abaf94 (visited on 05/23/2023).

– (July 2017). "Low-field anomalous magnetic phase in the kagome-lattice shandite C o 3 S n 2 S 2". en. In: *Physical Review B* 96.1, p. 014429. ISSN: 2469-9950, 2469-9969. DOI: 10.1103/PhysRevB.96.014429. URL: http://link.aps.org/doi/10.1103/PhysRevB.96.014429 (visited on 05/23/2023).

Kermarrec, E. et al. (Mar. 2017). "Ground state selection under pressure in the quantum pyrochlore magnet Yb2Ti2O7". en. In: *Nature Communications* 8.1, p. 14810. ISSN: 2041-1723. DOI: 10.1038/ncomms14810. URL: https://www.nature.com/articles/ncomms14810 (visited on 05/31/2023).

Kim, B. J., Hosub Jin, et al. (2008). "Novel Jeff=1/2 Mott state induced by relativistic spin-orbit coupling in Sr2IrO4." In: *Physical review letters* 101 7, p. 076402.

Kim, B. J., H. Ohsumi, et al. (Mar. 2009). "Phase-Sensitive Observation of a Spin-Orbital Mott State in Sr $_2$ IrO $_4$". en. In: *Science* 323.5919, pp. 1329–1332. ISSN: 0036-8075, 1095-9203. DOI: 10.1126/science.1167106. URL: https://www.science.org/doi/10.1126/science.1167106 (visited on 06/02/2023).

Kobayashi, Koji, Yuya Ominato, and Kentaro Nomura (July 2018). "Helicity-Protected Domain-Wall Magnetoresistance in Ferromagnetic Weyl Semimetal". en. In: *Journal of the Physical Society of Japan* 87.7, p. 073707. ISSN: 0031-9015, 1347-4073. DOI: 10.7566/JPSJ.87.073707. URL: https://journals.jps.jp/doi/10.7566/JPSJ.87.073707 (visited on 05/23/2023).

Kong, P P et al. (Sept. 2013). "Superconductivity of the topological insulator Bi $_2$ Se $_3$ at high pressure". en. In: *Journal of Physics: Condensed Matter* 25.36, p. 362204. ISSN: 0953-8984, 1361-648X. DOI: 10.1088/0953-8984/25/36/362204. URL: https://iopscience.iop.org/article/10.1088/0953-8984/25/36/362204 (visited on 05/31/2023).

Kong, Panpan et al. (Aug. 2021). "Superconductivity up to 243 K in the yttrium-hydrogen system under high pressure". en. In: *Nature Communications* 12.1, p. 5075. ISSN: 2041-1723. DOI: 10.1038/s41467-021-25372-2. URL: https://www.nature.com/articles/s41467-021-25372-2 (visited on 05/31/2023).

Koshino, Mikito (July 2016). "Cyclotron resonance of figure-of-eight orbits in a type-II Weyl semimetal". In: *Phys. Rev. B* 94 (3), p. 035202. DOI: 10.1103/PhysRevB.94.035202. URL: https://link.aps.org/doi/10.1103/PhysRevB.94.035202.

Kozlenko, D. P. et al. (May 2012). "From Quantum Disorder to Magnetic Order in an s = 1 / 2 Kagome Lattice: A Structural and Magnetic Study of Herbertsmithite at High Pressure". en. In: *Physical Review Letters* 108.18, p. 187207. ISSN: 0031-9007, 1079-7114. DOI: 10.1103/PhysRevLett.108.187207. URL: https://link.aps.org/doi/10.1103/PhysRevLett.108.187207 (visited on 05/31/2023).

Lachman, Ella et al. (Jan. 2020). "Exchange biased anomalous Hall effect driven by frustration in a magnetic kagome lattice". en. In: *Nature Communications* 11.1, p. 560. ISSN: 2041-1723. DOI: 10.1038/s41467-020-14326-9. URL: https://www.nature.com/articles/s41467-020-14326-9 (visited on 05/23/2023).

Lambert, C-H. et al. (Sept. 2014). “All-optical control of ferromagnetic thin films and nanostructures”. en. In: *Science* 345.6202, pp. 1337–1340. ISSN: 0036-8075, 1095-9203. DOI: 10.1126/science.1253493. URL: https://www.science.org/doi/10.1126/science.1253493 (visited on 06/01/2023).

Lee, Changmin et al. (May 2022). “Observation of a phase transition within the domain walls of ferromagnetic Co3Sn2S2”. en. In: *Nature Communications* 13.1, p. 3000. ISSN: 2041-1723. DOI: 10.1038/s41467-022-30460-y. URL: https://www.nature.com/articles/s41467-022-30460-y (visited on 05/23/2023).

Li, Peigang et al. (July 2020). “Giant room temperature anomalous Hall effect and tunable topology in a ferromagnetic topological semimetal Co2MnAl”. en. In: *Nature Communications* 11.1, p. 3476. ISSN: 2041-1723. DOI: 10.1038/s41467-020-17174-9. URL: https://www.nature.com/articles/s41467-020-17174-9 (visited on 05/23/2023).

Li, Peng et al. (2017). “Evidence for topological type-II Weyl semimetal WTe2”. In: *Nature communications* 8.1, pp. 1–8.

Li, Xiang et al. (Nov. 2021). “Magnetic order, disorder, and excitations under pressure in the Mott insulator Sr 2 IrO 4”. en. In: *Physical Review B* 104.20, p. L201111. ISSN: 2469-9950, 2469-9969. DOI: 10.1103/PhysRevB.104.L201111. URL: https://link.aps.org/doi/10.1103/PhysRevB.104.L201111 (visited on 06/02/2023).

Li, Yufeng et al. (2017). “Concurrence of superconductivity and structure transition in Weyl semimetal TaP under pressure”. In: *npj Quantum Materials* 2.1, pp. 1–7.

Li, Yupeng and Zhu-An Xu (Sept. 2019). “Exploring Topological Superconductivity in Topological Materials”. en. In: *Advanced Quantum Technologies* 2.9, p. 1800112. ISSN: 2511-9044, 2511-9044. DOI: 10.1002/qute.201800112. URL: https://onlinelibrary.wiley.com/doi/10.1002/qute.201800112 (visited on 05/31/2023).

Li, Zhi et al. (2018). “Second harmonic generation in the Weyl semimetal TaAs from a quantum kinetic equation”. In: *Physical Review B* 97.8, p. 085201.

Liu, D. F., A. J. Liang, et al. (Sept. 2019). “Magnetic Weyl semimetal phase in a Kagomé crystal”. en. In: *Science* 365.6459, pp. 1282–1285. ISSN: 0036-8075, 1095-9203. DOI: 10.1126/science.aav2873. URL: https://www.science.org/doi/10.1126/science.aav2873 (visited on 05/23/2023).

Liu, D. F., E. K. Liu, et al. (Jan. 2022). “Direct observation of the spin–orbit coupling effect in magnetic Weyl semimetal Co3Sn2S2”. en. In: *npj Quantum Materials* 7.1, p. 11. ISSN: 2397-4648. DOI: 10.1038/s41535-021-00392-9. URL: https://www.nature.com/articles/s41535-021-00392-9 (visited on 05/23/2023).

Liu, Enke et al. (Nov. 2018). "Giant anomalous Hall effect in a ferromagnetic kagome-lattice semimetal". en. In: *Nature Physics* 14.11, pp. 1125–1131. ISSN: 1745-2473, 1745-2481. DOI: 10.1038/s41567-018-0234-5. URL: https://www.nature.com/articles/s41567-018-0234-5 (visited on 05/23/2023).

Liu, Huimei and Giniyat Khaliullin (Feb. 2019). "Pseudo-Jahn-Teller Effect and Magnetoelastic Coupling in Spin-Orbit Mott Insulators". en. In: *Physical Review Letters* 122.5, p. 057203. ISSN: 0031-9007, 1079-7114. DOI: 10.1103/PhysRevLett.122.057203. URL: https://link.aps.org/doi/10.1103/PhysRevLett.122.057203 (visited on 06/02/2023).

Lu, Mingchun et al. (Aug. 2016). "High-pressure crystal structures of TaAs from first-principles calculations". en. In: *Solid State Communications* 240, pp. 37–40. ISSN: 0038-1098. DOI: 10.1016/j.ssc.2016.04.024. URL: https://www.sciencedirect.com/science/article/pii/S0038109816300643 (visited on 02/25/2022).

Lupi, S. et al. (Nov. 2010). "A microscopic view on the Mott transition in chromium-doped V2O3". en. In: *Nature Communications* 1.1, p. 105. ISSN: 2041-1723. DOI: 10.1038/ncomms1109. URL: https://www.nature.com/articles/ncomms1109 (visited on 05/31/2023).

Lv, B. Q. et al. (July 2015). "Experimental Discovery of Weyl Semimetal TaAs". In: *Physical Review X* 5.3. Publisher: American Physical Society, p. 031013. DOI: 10.1103/PhysRevX.5.031013. URL: https://link.aps.org/doi/10.1103/PhysRevX.5.031013 (visited on 02/25/2022).

Ma, Junchao et al. (May 2019). "Nonlinear photoresponse of type-II Weyl semimetals". In: *Nature Materials* 18.5, pp. 476–481. ISSN: 1476-4660. DOI: 10.1038/s41563-019-0296-5. URL: https://doi.org/10.1038/s41563-019-0296-5.

Ma, Qiong et al. (2017). "Direct optical detection of Weyl fermion chirality in a topological semimetal". In: *Nature Physics* 13, pp. 842–847. DOI: 10.1038/nphys4146.

Malavi, Pallavi S., S. Karmakar, and S. M. Sharma (Jan. 2016). "$Cd_2Re_2O_7$ under high pressure: Pyrochlore lattice distortion-driven metal-to-nonmetal transition". In: *Physical Review B* 93.3. Publisher: American Physical Society, p. 035139. DOI: 10.1103/PhysRevB.93.035139. URL: https://link.aps.org/doi/10.1103/PhysRevB.93.035139 (visited on 02/26/2022).

Mangin, S. et al. (Mar. 2014). "Engineered materials for all-optical helicity-dependent magnetic switching". en. In: *Nature Materials* 13.3, pp. 286–292. ISSN: 1476-1122, 1476-4660. DOI: 10.1038/nmat3864. URL: https://www.nature.com/articles/nmat3864 (visited on 06/01/2023).

Mirebeau, I. et al. (Oct. 2004). "Pressure and Field Induced Magnetic Order in the Spin Liquid T b 2 T i 2 O 7 as Studied by Single Crystal Neutron Diffraction". en. In: *Physical Review Letters* 93.18, p. 187204. ISSN: 0031-9007, 1079-7114. DOI:

10.1103/PhysRevLett.93.187204. URL: https://link.aps.org/doi/10.1103/PhysRevLett.93.187204 (visited on 05/31/2023).

Moggach, Stephen A. et al. (Apr. 2008). "Incorporation of a new design of backing seat and anvil in a Merrill-Bassett diamond anvil cell". English. In: *Journal of Applied Crystallography* 41. Publisher: INT UNION CRYSTALLOGRAPHY, pp. 249–251. ISSN: 0021-8898. DOI: 10.1107/S0021889808000514. URL: https://www.research.ed.ac.uk/en/publications/incorporation-of-a-new-design-of-backing-seat-and-anvil-in-a-merr (visited on 02/25/2022).

Moll, Philip J. W. et al. (July 2016). "Transport evidence for Fermi-arc-mediated chirality transfer in the Dirac semimetal Cd3As2". In: *Nature* 535.7611, pp. 266–270. ISSN: 1476-4687. DOI: 10.1038/nature18276. URL: https://doi.org/10.1038/nature18276.

Nair, Nityan L. et al. (Aug. 2020). "Signatures of possible surface states in TaAs". In: *Phys. Rev. B* 102 (7), p. 075402. DOI: 10.1103/PhysRevB.102.075402. URL: https://link.aps.org/doi/10.1103/PhysRevB.102.075402.

Okabe, H. et al. (Apr. 2011). "Ba_2IrO_4 : $Aspin-orbitMottinsulatingquasi-two-dimensionalantiferromagnet$". In: *Phys. Rev. B* 83. DOI: 10.1103/PhysRevB.83.155118.

Okamura, Y. et al. (Sept. 2020). "Giant magneto-optical responses in magnetic Weyl semimetal Co3Sn2S2". en. In: *Nature Communications* 11.1, p. 4619. ISSN: 2041-1723. DOI: 10.1038/s41467-020-18470-0. URL: https://www.nature.com/articles/s41467-020-18470-0 (visited on 05/23/2023).

Orenstein, J. et al. (2021). "Topology and Symmetry of Quantum Materials via Nonlinear Optical Responses". In: *Annual Review of Condensed Matter Physics* 12.1. _eprint: https://doi.org/10.1146/annurev-conmatphys-031218-013712, pp. 247–272. DOI: 10.1146/annurev-conmatphys-031218-013712. URL: https://doi.org/10.1146/annurev-conmatphys-031218-013712 (visited on 02/25/2022).

Osterhoudt, Gavin B. et al. (May 2019). "Colossal mid-infrared bulk photovoltaic effect in a type-I Weyl semimetal". en. In: *Nature Materials* 18.5. Number: 5 Publisher: Nature Publishing Group, pp. 471–475. ISSN: 1476-4660. DOI: 10.1038/s41563-019-0297-4. URL: https://www.nature.com/articles/s41563-019-0297-4 (visited on 02/25/2022).

Parameswaran, S. A. et al. (Sept. 2014). "Probing the Chiral Anomaly with Nonlocal Transport in Three-Dimensional Topological Semimetals". In: *Physical Review X* 4.3. Publisher: American Physical Society, p. 031035. DOI: 10.1103/PhysRevX.4.031035. URL: https://link.aps.org/doi/10.1103/PhysRevX.4.031035 (visited on 02/25/2022).

Patankar, Shreyas et al. (Oct. 2018). "Resonance-enhanced optical nonlinearity in the Weyl semimetal TaAs". In: *Physical Review B* 98.16. Publisher: American Physical Society, p. 165113. DOI: 10.1103/PhysRevB.98.165113. URL: https://link.aps.org/doi/10.1103/PhysRevB.98.165113 (visited on 02/25/2022).

Porras, J. et al. (Feb. 2019). "Pseudospin-lattice coupling in the spin-orbit Mott insulator Sr 2 IrO 4". en. In: *Physical Review B* 99.8, p. 085125. ISSN: 2469-9950, 2469-9969. DOI: 10.1103/PhysRevB.99.085125. URL: https://link.aps.org/doi/10.1103/PhysRevB.99.085125 (visited on 06/02/2023).

Qi, Yanpeng et al. (May 2017). "Topological Quantum Phase Transition and Superconductivity Induced by Pressure in the Bismuth Tellurohalide BiTeI". en. In: *Advanced Materials* 29.18, p. 1605965. ISSN: 09359648. DOI: 10.1002/adma.201605965. URL: https://onlinelibrary.wiley.com/doi/10.1002/adma.201605965 (visited on 05/31/2023).

Rau, Jeffrey G., Eric Kin-Ho Lee, and Hae-Young Kee (Mar. 2016). "Spin-Orbit Physics Giving Rise to Novel Phases in Correlated Systems: Iridates and Related Materials". en. In: *Annual Review of Condensed Matter Physics* 7.1, pp. 195–221. ISSN: 1947-5454, 1947-5462. DOI: 10.1146/annurev-conmatphys-031115-011319. URL: https://www.annualreviews.org/doi/10.1146/annurev-conmatphys-031115-011319 (visited on 05/31/2023).

Rossi, Antonio et al. (Oct. 2021). "Electronic structure and topology across T c in the magnetic Weyl semimetal Co 3 Sn 2 S 2". en. In: *Physical Review B* 104.15, p. 155115. ISSN: 2469-9950, 2469-9969. DOI: 10.1103/PhysRevB.104.155115. URL: https://link.aps.org/doi/10.1103/PhysRevB.104.155115 (visited on 05/23/2023).

Samanta, K., F. M. Ardito, et al. (Sept. 2018). "First-order structural transition and pressure-induced lattice/phonon anomalies in Sr 2 IrO 4". en. In: *Physical Review B* 98.9, p. 094101. ISSN: 2469-9950, 2469-9969. DOI: 10.1103/PhysRevB.98.094101. URL: https://link.aps.org/doi/10.1103/PhysRevB.98.094101 (visited on 06/02/2023).

Samanta, K., R. Tartaglia, et al. (Feb. 2020). "Anisotropic lattice compression and pressure-induced electronic phase transitions in Sr 2 IrO 4". en. In: *Physical Review B* 101.7, p. 075121. ISSN: 2469-9950, 2469-9969. DOI: 10.1103/PhysRevB.101.075121. URL: https://link.aps.org/doi/10.1103/PhysRevB.101.075121 (visited on 06/02/2023).

Shan, Junyi (2022). "Non-thermal optical engineering of strongly-correlated quantum materials". en. In.

Sharma, M M et al. (Aug. 2022). "Comprehensive review on topological superconducting materials and interfaces". en. In: *Superconductor Science and Technology* 35.8, p. 083003. ISSN: 0953-2048, 1361-6668. DOI: 10.1088/1361-6668/

ac6987. URL: https://iopscience.iop.org/article/10.1088/1361-6668/ac6987 (visited on 05/31/2023).

Shen, Zihao et al. (Feb. 2023). "Anomalous depinning of magnetic domain walls within the ferromagnetic phase of the Weyl semimetal Co3Sn2S2". en. In: *Journal of Physics: Condensed Matter* 35.4. arXiv:2205.06420 [cond-mat], p. 045802. ISSN: 0953-8984, 1361-648X. DOI: 10.1088/1361-648X/aca57b. URL: http://arxiv.org/abs/2205.06420 (visited on 05/23/2023).

Sirica, N. et al. (May 2019). "Tracking Ultrafast Photocurrents in the Weyl Semimetal TaAs Using THz Emission Spectroscopy". In: *Physical Review Letters* 122.19. Publisher: American Physical Society, p. 197401. DOI: 10.1103/PhysRevLett.122.197401. URL: https://link.aps.org/doi/10.1103/PhysRevLett.122.197401 (visited on 02/25/2022).

Soh, Jian-Rui et al. (Mar. 2022). "Magnetic structure of the topological semimetal Co 3 Sn 2 S 2". en. In: *Physical Review B* 105.9, p. 094435. ISSN: 2469-9950, 2469-9969. DOI: 10.1103/PhysRevB.105.094435. URL: https://link.aps.org/doi/10.1103/PhysRevB.105.094435 (visited on 05/23/2023).

Stanciu, C. D. et al. (July 2007). "All-Optical Magnetic Recording with Circularly Polarized Light". en. In: *Physical Review Letters* 99.4, p. 047601. ISSN: 0031-9007, 1079-7114. DOI: 10.1103/PhysRevLett.99.047601. URL: https://link.aps.org/doi/10.1103/PhysRevLett.99.047601 (visited on 06/01/2023).

Sugawara, Akira et al. (Oct. 2019). "Magnetic domain structure within half-metallic ferromagnetic kagome compound C o 3 S n 2 S 2". en. In: *Physical Review Materials* 3.10, p. 104421. ISSN: 2475-9953. DOI: 10.1103/PhysRevMaterials.3.104421. URL: https://link.aps.org/doi/10.1103/PhysRevMaterials.3.104421 (visited on 05/23/2023).

Sun, Yan et al. (Sept. 2016). "Strong Intrinsic Spin Hall Effect in the TaAs Family of Weyl Semimetals". In: *Phys. Rev. Lett.* 117 (14), p. 146403. DOI: 10.1103/PhysRevLett.117.146403. URL: https://link.aps.org/doi/10.1103/PhysRevLett.117.146403.

Torchinsky, D. H. et al. (Mar. 2015). "Structural Distortion-Induced Magnetoelastic Locking in Sr 2 IrO 4 Revealed through Nonlinear Optical Harmonic Generation". en. In: *Physical Review Letters* 114.9, p. 096404. ISSN: 0031-9007, 1079-7114. DOI: 10.1103/PhysRevLett.114.096404. URL: https://link.aps.org/doi/10.1103/PhysRevLett.114.096404 (visited on 06/02/2023).

Torchinsky, Darius et al. (2014). "A low temperature nonlinear optical rotational anisotropy spectrometer for the determination of crystallographic and electronic symmetries". In: *Review of Scientific Instruments* 85.8, p. 083102. DOI: 10.1063/1.4891417. eprint: https://doi.org/10.1063/1.4891417. URL: https://doi.org/10.1063/1.4891417.

Vale, James George (2017). “The nature of the metal-insulator transition in 5d transition metal oxides”. en. In.

VanGennep, D et al. (July 2017). “Evolution of the Fermi surface of BiTeCl with pressure”. en. In: *Journal of Physics: Condensed Matter* 29.29, p. 295702. ISSN: 0953-8984, 1361-648X. DOI: 10.1088/1361-648X/aa73b7. URL: https://iopscience.iop.org/article/10.1088/1361-648X/aa73b7 (visited on 05/31/2023).

Vankó, György et al. (Jan. 2006). “Temperature- and pressure-induced spin-state transitions in LaCoO 3”. en. In: *Physical Review B* 73.2, p. 024424. ISSN: 1098-0121, 1550-235X. DOI: 10.1103/PhysRevB.73.024424. URL: https://link.aps.org/doi/10.1103/PhysRevB.73.024424 (visited on 05/31/2023).

Vasiliev, A. N. et al. (July 2005). “Long-range magnetic order in quasi-one-dimensional chromium-based (S = 3 2) pyroxenes (Li , Na) Cr (Si , Ge) 2 O 6”. en. In: *Physical Review B* 72.1, p. 012412. ISSN: 1098-0121, 1550-235X. DOI: 10.1103/PhysRevB.72.012412. URL: https://link.aps.org/doi/10.1103/PhysRevB.72.012412 (visited on 05/31/2023).

Wan, Xiangang et al. (May 2011). “Topological semimetal and Fermi-arc surface states in the electronic structure of pyrochlore iridates”. In: *Physical Review B* 83.20. Publisher: American Physical Society, p. 205101. DOI: 10.1103/PhysRevB.83.205101. URL: https://link.aps.org/doi/10.1103/PhysRevB.83.205101 (visited on 02/25/2022).

Wang, Qi et al. (Sept. 2018). “Large intrinsic anomalous Hall effect in half-metallic ferromagnet Co3Sn2S2 with magnetic Weyl fermions”. en. In: *Nature Communications* 9.1, p. 3681. ISSN: 2041-1723. DOI: 10.1038/s41467-018-06088-2. URL: https://www.nature.com/articles/s41467-018-06088-2 (visited on 05/23/2023).

Wang, Yishu (2018). “Antiferromagnetic quantum phase transitions: continuous tuning and direct probes of competing states”. en. In.

Watanabe, D. et al. (Sept. 2012). “Novel Pauli-paramagnetic quantum phase in a Mott insulator”. en. In: *Nature Communications* 3.1, p. 1090. ISSN: 2041-1723. DOI: 10.1038/ncomms2082. URL: https://www.nature.com/articles/ncomms2082 (visited on 05/31/2023).

Wilczek, Frank (Sept. 2009). “Majorana returns”. en. In: *Nature Physics* 5.9, pp. 614–618. ISSN: 1745-2473, 1745-2481. DOI: 10.1038/nphys1380. URL: https://www.nature.com/articles/nphys1380 (visited on 05/31/2023).

Witczak-Krempa, William et al. (Mar. 2014). “Correlated Quantum Phenomena in the Strong Spin-Orbit Regime”. en. In: *Annual Review of Condensed Matter Physics* 5.1, pp. 57–82. ISSN: 1947-5454, 1947-5462. DOI: 10.1146/annurev-conmatphys-020911-125138. URL: https://www.annualreviews.org/doi/10.1146/annurev-conmatphys-020911-125138 (visited on 05/31/2023).

Wu, Liang et al. (Apr. 2017). “Giant anisotropic nonlinear optical response in transition metal monopnictide Weyl semimetals”. en. In: *Nature Physics* 13.4. Number: 4 Publisher: Nature Publishing Group, pp. 350–355. ISSN: 1745-2481. DOI: 10.1038/nphys3969. URL: https://www.nature.com/articles/nphys3969 (visited on 02/25/2022).

Xu, Su-Yang et al. (Aug. 2015). “Discovery of a Weyl fermion semimetal and topological Fermi arcs”. In: *Science* 349.6248. Publisher: American Association for the Advancement of Science, pp. 613–617. DOI: 10.1126/science.aaa9297. URL: https://www.science.org/doi/full/10.1126/science.aaa9297 (visited on 02/25/2022).

Yamaura, Jun-ichi et al. (Jan. 2017). “Successive spatial symmetry breaking under high pressure in the spin-orbit-coupled metal $Cd_2Re_2O_7$”. In: *Physical Review B* 95.2. Publisher: American Physical Society, p. 020102. DOI: 10.1103/PhysRevB.95.020102. URL: https://link.aps.org/doi/10.1103/PhysRevB.95.020102 (visited on 02/26/2022).

Yang, Kai-Yu, Yuan-Ming Lu, and Ying Ran (Aug. 2011). “Quantum Hall effects in a Weyl semimetal: Possible application in pyrochlore iridates”. In: *Phys. Rev. B* 84 (7), p. 075129. DOI: 10.1103/PhysRevB.84.075129. URL: https://link.aps.org/doi/10.1103/PhysRevB.84.075129.

Yang, L. X. et al. (Sept. 2015). “Weyl semimetal phase in the non-centrosymmetric compound TaAs”. en. In: *Nature Physics* 11.9. Number: 9 Publisher: Nature Publishing Group, pp. 728–732. ISSN: 1745-2481. DOI: 10.1038/nphys3425. URL: https://www.nature.com/articles/nphys3425 (visited on 02/25/2022).

Ying, Jian-Jun et al. (Mar. 2016). “Realization of insulating state and superconductivity in the Rashba semiconductor BiTeCl”. en. In: *Physical Review B* 93.10, p. 100504. ISSN: 2469-9950, 2469-9969. DOI: 10.1103/PhysRevB.93.100504. URL: https://link.aps.org/doi/10.1103/PhysRevB.93.100504 (visited on 05/31/2023).

Yoshikawa, Naotaka et al. (Dec. 2022). “Non-volatile chirality switching by all-optical magnetization reversal in ferromagnetic Weyl semimetal Co3Sn2S2”. en. In: *Communications Physics* 5.1, p. 328. ISSN: 2399-3650. DOI: 10.1038/s42005-022-01106-8. URL: https://www.nature.com/articles/s42005-022-01106-8 (visited on 06/01/2023).

Zhang, Cheng-Long et al. (2016). “Signatures of the Adler–Bell–Jackiw chiral anomaly in a Weyl fermion semimetal”. In: *Nature communications* 7.1, pp. 1–9.

Zhang, J. L. et al. (Jan. 2011). “Pressure-induced superconductivity in topological parent compound Bi $_2$ Te $_3$”. en. In: *Proceedings of the National Academy of Sciences* 108.1, pp. 24–28. ISSN: 0027-8424, 1091-6490. DOI: 10.1073/pnas.1014085108. URL: https://pnas.org/doi/full/10.1073/pnas.1014085108 (visited on 05/31/2023).

Zhang, Jingyun et al. (Oct. 2017). "Prediction of high-pressure phases of Weyl semimetal NbAs and NbP". en. In: *Scientific Reports* 7.1. Number: 1 Publisher: Nature Publishing Group, p. 13251. ISSN: 2045-2322. DOI: 10.1038/s41598-017-13610-x. URL: https://www.nature.com/articles/s41598-017-13610-x (visited on 02/25/2022).

Zhang, Qiang et al. (Sept. 2021). "Unusual Exchange Couplings and Intermediate Temperature Weyl State in Co 3 Sn 2 S 2". en. In: *Physical Review Letters* 127.11, p. 117201. ISSN: 0031-9007, 1079-7114. DOI: 10.1103/PhysRevLett.127.117201. URL: https://link.aps.org/doi/10.1103/PhysRevLett.127.117201 (visited on 05/23/2023).

Zhou, Yonghui, Xuliang Chen, et al. (Apr. 2016). "Pressure-induced reemergence of superconductivity in topological insulator Sr 0.065 Bi 2 Se 3". en. In: *Physical Review B* 93.14, p. 144514. ISSN: 2469-9950, 2469-9969. DOI: 10.1103/PhysRevB.93.144514. URL: https://link.aps.org/doi/10.1103/PhysRevB.93.144514 (visited on 05/31/2023).

Zhou, Yonghui, Juefei Wu, et al. (Mar. 2016). "Pressure-induced superconductivity in a three-dimensional topological material ZrTe $_5$". en. In: *Proceedings of the National Academy of Sciences* 113.11, pp. 2904–2909. ISSN: 0027-8424, 1091-6490. DOI: 10.1073/pnas.1601262113. URL: https://pnas.org/doi/full/10.1073/pnas.1601262113 (visited on 05/31/2023).

Živković, Ivica et al. (Nov. 2022). "Unraveling the origin of the peculiar transition in the magnetically ordered phase of the Weyl semimetal Co 3 Sn 2 S 2". en. In: *Physical Review B* 106.18, p. L180403. ISSN: 2469-9950, 2469-9969. DOI: 10.1103/PhysRevB.106.L180403. URL: https://link.aps.org/doi/10.1103/PhysRevB.106.L180403 (visited on 05/23/2023).

Zocco, D. A. et al. (June 2014). "Persistent non-metallic behavior in Sr2IrO4 and Sr3Ir2O7 at high pressures". en. In: *Journal of Physics: Condensed Matter* 26.25. arXiv:1304.5864 [cond-mat], p. 255603. ISSN: 0953-8984, 1361-648X. DOI: 10.1088/0953-8984/26/25/255603. URL: http://arxiv.org/abs/1304.5864 (visited on 06/02/2023).

Zyuzin, A. A. and A. A. Burkov (Sept. 2012). "Topological response in Weyl semimetals and the chiral anomaly". In: *Phys. Rev. B* 86 (11), p. 115133. DOI: 10.1103/PhysRevB.86.115133. URL: https://link.aps.org/doi/10.1103/PhysRevB.86.115133.